ARGONNE NATIONAL LABORATORY
9700 South Cass Avenue
Argonne, Illinois 60439

PRACTICAL SUPERCONDUCTOR DEVELOPMENT FOR ELECTRICAL POWER APPLICATIONS

ANNUAL REPORT FOR FY 2000

U. Balachandran

Contributors:

Y. S. Cha	J. R. Hull	V. A. Maroni
S. E. Dorris	Y. Jee	R. L. McDaniel
J. T. Dusek	R. E. Koritala	N. Merchant
J. E. Emerson	M. Lelovic	D. J. Miller
B. L. Fisher	M. Li	J.-H. Park
K. C. Goretta	J. W. Lucas	J. J. Picciolo
K. E. Gray	B. Ma	J. P. Singh

Energy Technology Division

December 2000

Materials Science Division.
Chemical Technology Division.

Contents

Figures

v

Tables

PRACTICAL SUPERCONDUCTOR DEVELOPMENT FOR ELECTRICAL POWER APPLICATIONS

ANNUAL REPORT FOR FY 2000

Abstract

Most large-scale high-critical-temperature superconductor applications require wires or tapes that can carry high currents in applied magnetic fields. This report describes technical progress of research and development efforts aimed at producing superconducting components and devices in the Y-Ba-Cu-O and Bi-(Pb)-Sr-Ca-Cu-O systems. Topics discussed are formation of first- and second-generation composite conductors, characterization of structures and superconducting and mechanical properties, modeling of grain-boundary current transport, and fabrication and analysis of prototype components.

1 Introduction

The superconductor program at Argonne National Laboratory (ANL) includes film and bulk processing directed toward improving the properties of high-T_c superconductors (HTSs), developing processing methods for production of commercial conductors, fabricating and testing prototype conductors, and studying basic phenomena. Emphasis is placed on the technology and science of fabrication of long-length tapes and wires. Cooperative relationships with industrial and academic partners are integral to this program. The principal objective of the ANL program is to develop methods to fabricate and use structurally reliable HTSs for generation, transmission, and storage of electrical energy. Work is now focused on superconductors based on yttrium-barium-copper oxide and bismuth-lead-strontium-calcium-copper oxide.

Currently, composite and monolithic conductors in the form of wires, tapes, films, or other shapes must meet several requirements. For most applications, the conductors must be capable of carrying high currents in the presence of high magnetic fields and must be strong, flexible, and chemically and cryogenically stable. Potential applications for such conductors include transmission lines, motors, generators, transformers, magnetic-energy storage devices, and electronics. The principal impediments to the use of bulk HTSs are low critical current (I_c) and critical current density (J_c) in large applied magnetic fields, relatively poor mechanical properties, and difficulty in fabricating very long lengths of conductors with uniform properties. Processing methods that will improve the HTSs have been and continue to be developed, with most of the effort centered on $YBa_2Cu_3O_x$ (Y-123) in the form of coated conductors.

This report reviews the technical progress and status of (1) Y-123 tapes and their substrate materials, (2) $(Bi,Pb)_2Sr_2Ca_2Cu_3O_X$ (Bi-2223) and $Bi_2Sr_2CaCu_2O_X$ (Bi-2212) wires and tapes, (3) study of microstructures and fundamental grain-boundary properties, and (4) modeling and testing of key properties of prototype superconducting devices.

2 Technical Progress in 1999–2000

2.1 Y-Ba-Cu-O Coated Conductors

The coated-conductor effort is focused on five main tasks: preparation of biaxially textured substrates on metallic foils; epitaxial deposition of Y-123 onto textured substrates; detailed study of microstructure and texture; measurement of properties of interest to the application of coated conductors, with emphasis on superconducting properties such as critical temperature (T_c), I_c, and J_c; and examination and modeling of fundamental properties, such as current transport across grain boundaries.

Although we have used single-crystal substrates such as $LaAlO_3$ and $SrTiO_3$ for preliminary studies, we now focus on using Hastelloy C coated with various textured buffer layers applied by electron-beam evaporation or pulsed laser deposition (PLD). Biaxial texture in MgO has been induced by inclined substrate deposition (ISD), and in Y_2O_3-stabilized ZrO_2 (YSZ) by ion-beam-assisted deposition (IBAD). Y-123 layers have been deposited by either PLD or a solution technique based on trifluoroacetates.

In addition to using standard techniques such as scanning and transmission electron microscopy (SEM and TEM), and X-ray diffraction to characterize the microstructures of our conductors, we have used ANL's Advanced Photon Source (APS) and Raman spectroscopy to acquire detailed information about structure. Because current transport is generally limited by grain boundaries, we continue to study the nature and transport properties of individual boundaries.

2.1.1 Substrate Development for Coated Conductors

Inclined Substrate Deposition of MgO

ISD offers promise as a rapid and inexpensive technique to texture buffer layers for coated conductors. Work over the past year focused on confirming the technological merit of ISD. Textured MgO layers were applied on static and moving substrates, and their microstructures and properties were examined.

Biaxially textured thin films of MgO have been deposited by electron-beam evaporation on Ni-alloy tapes as oriented buffer layers for coated conductors

(Fig. 1). The substrates were inclined with respect to the atomic vapor and translated through collimated dual-vapor sources. Growth anisotropy in the MgO, and self-shadowing effects due to the inclined angle combine to create a biaxial texture in the deposited thin films. MgO films grown to thicknesses of 2.0 μm with this ISD technique have yielded in-plane textures of 10–12° full-width half-maximum (FWHM). Results of a parametric study on the in-plane texture in short-length static-mode samples, along with preliminary results of long-length samples deposited under translating conditions, are summarized.
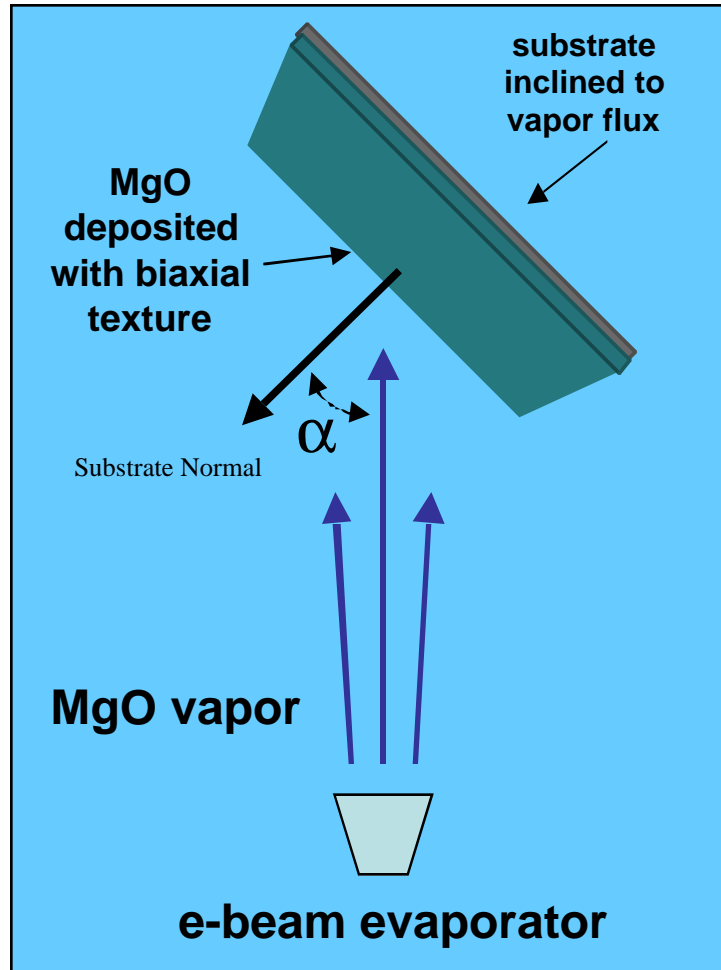
Fig. 1. Schematic diagram of ISD process.

We have investigated the dependence of texture development on processing in MgO films deposited by ISD to optimize the deposition parameters required for continuous coating. ISD of MgO has proved effective in creating short-length biaxially textured Y-123 coated conductors (see, e.g., M. Bauer et al., IEEE Trans. Appl. Supercond. 9 [1999] 1502). We coated 0.5-m-long tapes by using a collimated-flux inclined substrate deposition (CF-ISD) geometry with feed rates of 6.1 cm/min. The texture in the MgO films was evaluated with four-circle X-ray diffraction and selected-area electron diffraction (SAED). Growth morphology and structure were investigated by TEM.

Hastelloy C tapes were ultrasonically cleaned in acetone and methanol prior to loading in a reel-to-reel continuous-deposition system. The system was designed to allow simultaneous deposition on two tapes. The feed mechanism and take-up reel were designed to put the as-coated MgO tape in compression, with a strain of <5%. The tapes were inclined ≈40° with respect to the atomic vapor, which was created with a dual-electron-beam evaporation system. Evaporation was conducted in two zones; each contained a group of collimators that restricted the angular variance of the atomic flux to <10°. Feed rate through the two collimated deposition zones was adjusted so that MgO was deposited to a thickness of 1.0 μm in a single pass. The deposition rate for continuous coating was ≈200 Å/s.

Cross-sectional TEM coupled with SAED allowed the investigation of texture development in ISD MgO as a function of thickness (Fig. 2). From intensity-versus-thickness plots of dark-field photomicrographs, we determined that the zone where MgO coalesced into textured films occurs at ≈900 nm. X-ray diffraction indicated that the textures of ISD MgO films improved with thickness (Fig. 3). We note that in contrast to YSZ, the (001) axis of ISD MgO is not normal to the substrate; it is tilted by an angle β toward the direction of deposition (Fig. 4).

In-plane texture of the MgO on static samples exhibited little dependence on deposition rate, but rates ≥≈60 Å/s may lead to poorer texture (Fig. 5). Deposition on static samples also indicated that in-plane texture improved with an increase in sample inclination with respect to the vapor source; this in turn inclined the (200) face, which grows toward the vapor (Fig. 6).
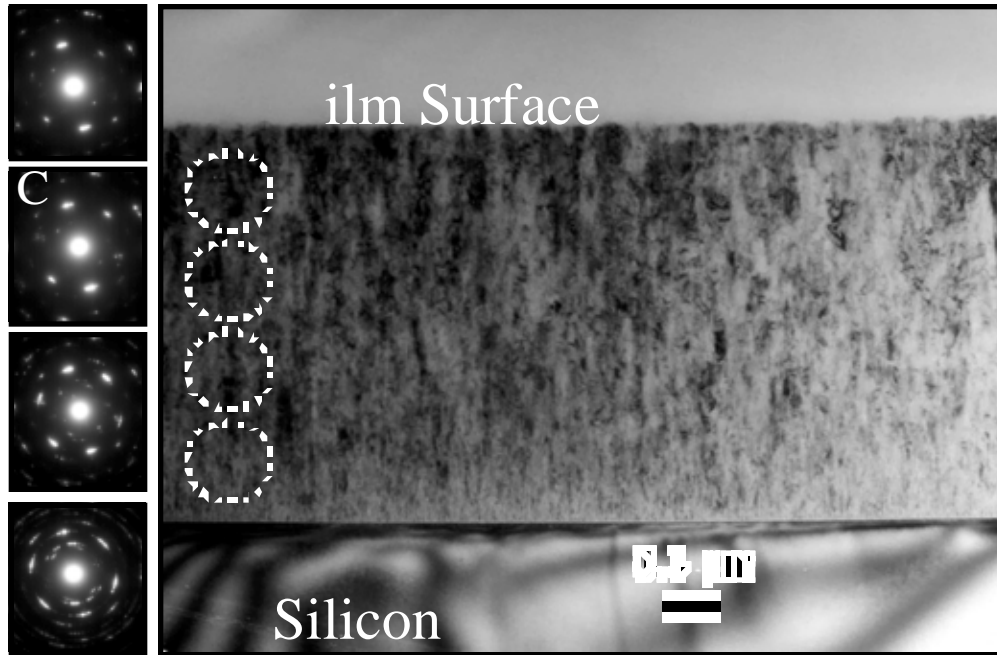
Fig. 2.   TEM photomicrograph of statically processed film on Si, with SAED patterns at various film thicknesses.

FWHM = 5.5 + 57.85*exp(-d/1.46)
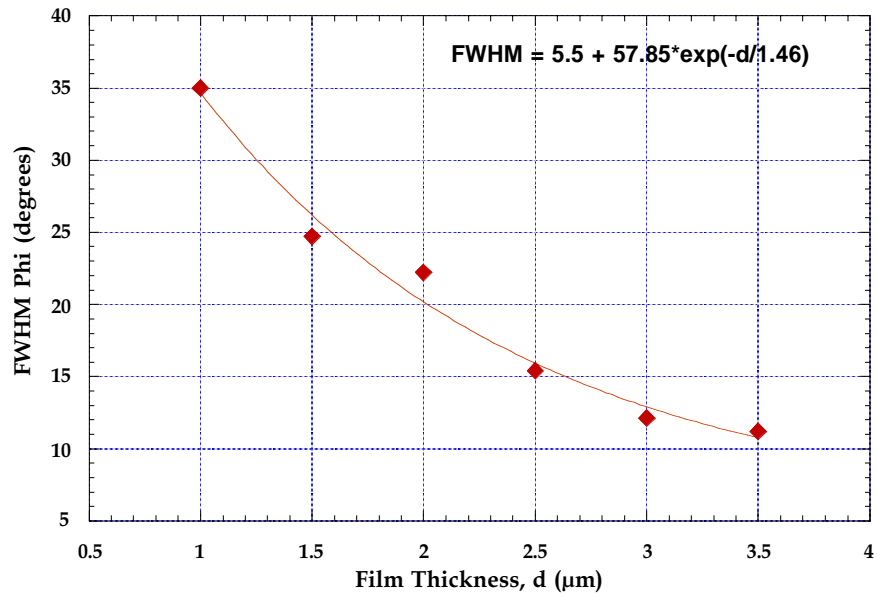
Fig. 3. FWHM of φ scans vs. thickness of MgO film.
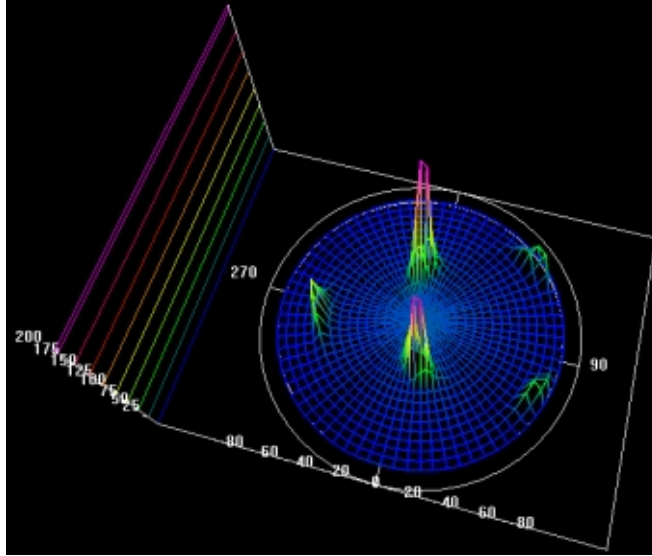
Fig. 4. Three-dimensional pole (200) figure of typical ISD MgO film.

The average in-plane FWHM of a 0.5-m-long tape deposited under continuous conditions, as measured with pole figures, was ≈24°. This value is the average FWHM measured from 10 positions along the tapes at approximately every 5 cm. The standard deviation of the FWHM was 1°, with the best value equal to 23°. These values are slightly higher than expected from the use of 10° collimators; however, the measured FWHM values are from films that are significantly thinner than the statically processed samples, and the surface texture is expected to be much sharper than the bulk value (Fig. 3). In addition, the deposition rate of 200 Å/s was probably too fast to achieve optimal texture.

Work is in progress to further address textures on moving and static substrates. To confirm the quality of the texture surface of the CF-ISD MgO films, we will also evaluate the effects of a thick homoepitaxial layer.

Although significant progress has been made in the growth of MgO buffer layers during ISD, substantial further improvements must be achieved. For example, microcracks have been observed, as shown in Fig. 7, a plan-view TEM image of an MgO film deposited at a substrate inclination angle of 55°. These cracks and significant surface roughness are due to shadowing by columnar grains and to the habit of MgO to preferentially grow the (200) equilibrium crystal. In FY2001, we will examine the extent to which we can smooth the MgO surface. Statically processed samples will be used in most of this effort.
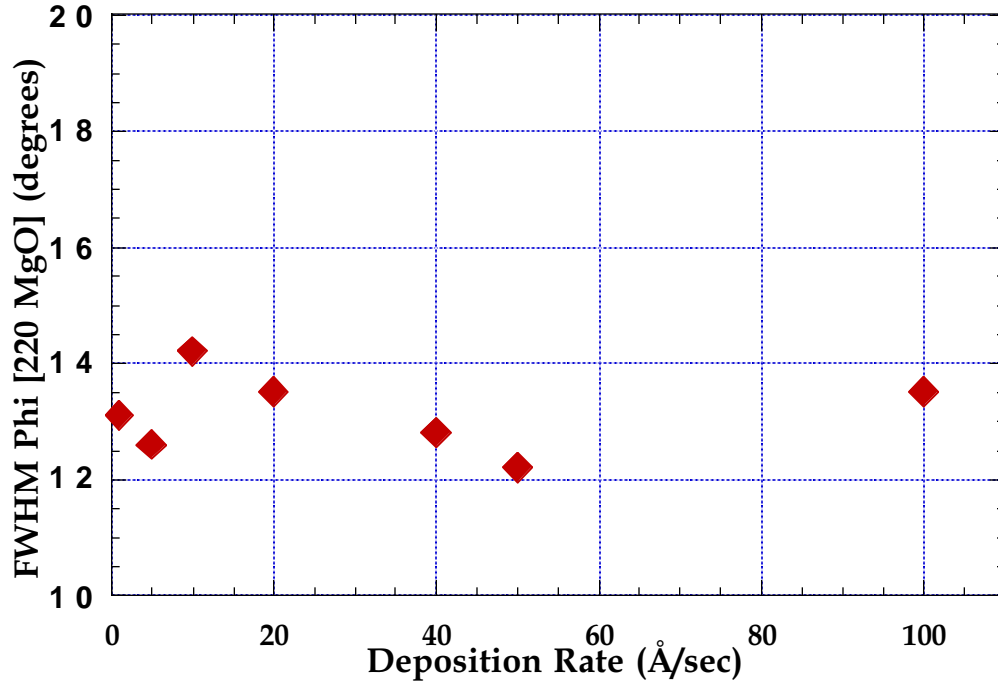
Fig. 5. *In-plane texture of ISD MgO vs. deposition rate for 2.5-µm-thick films.*
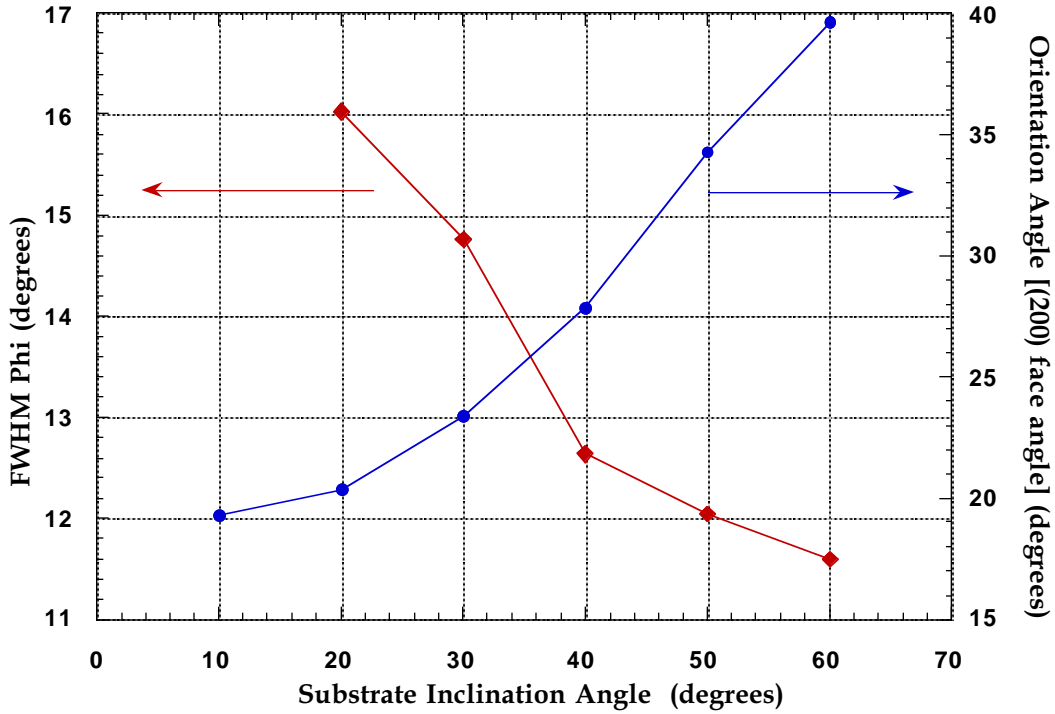
Fig. 6. *In-plane FWHM and (200)-face orientation of ISD MgO versus substrate inclination angle in statically processed samples.*
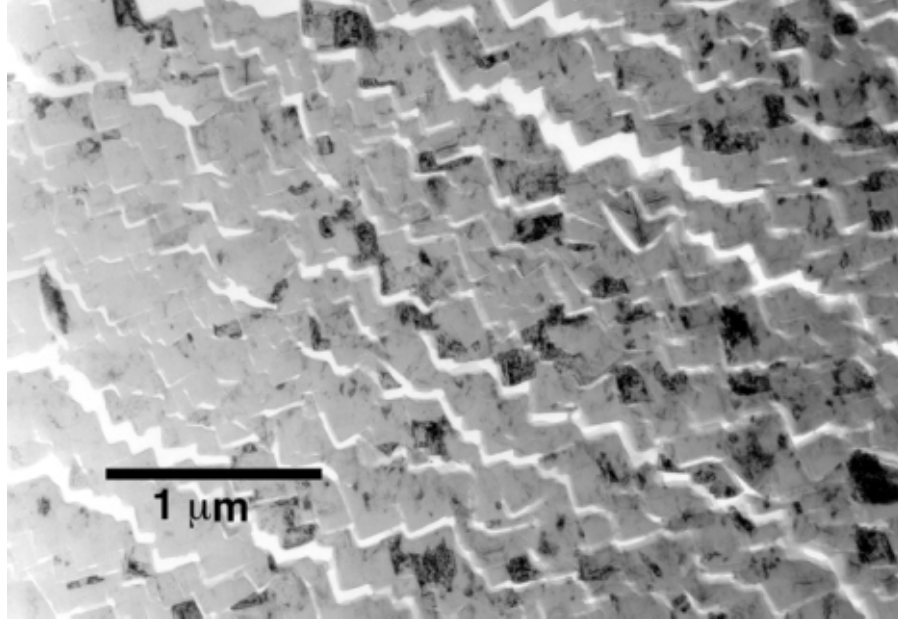
Fig. 7. Plan-view TEM photomicrograph of ISD MgO layer.

Also, several studies have shown that biaxially textured YSZ films can be deposited by a combination of ISD and PLD (see, for example, K. Matsumoto et al., Physica C 330 [2000] 150). We intend to evaluate such films for our coated-conductor substrates.

Ion-Beam-Assisted Deposition of YSZ

A second IBAD system (IBAD-2) was brought on-line in FY2000 and films were produced (Figs. 8 and 9). IBAD-2 has advanced our study of the effects of film thickness, ion bombardment angle, and r-value on texture. In the new chamber, a 3-cm Kaufman ion gun mounted on a motorized rail allows the bombardment angle to be varied independently from the substrate. A unique Faraday cup assembly measures the ion fluence and beam divergence and provides information about the effect of ion channeling on texture development. In addition, characterization by in-situ reflectivity high-energy electron diffraction provides a better understanding of the growth mechanisms and should eventually lead to YSZ IBAD thin films with greatly improved in-plane textures.

With two electron-beam evaporators, one being a multiunit evaporator, the system is equipped to handle up to five materials at a time. This configuration allows versatility in buffer layer architecture; for example, Y_2O_3, CeO_2, and MgO cap layers can all be deposited within the same chamber with
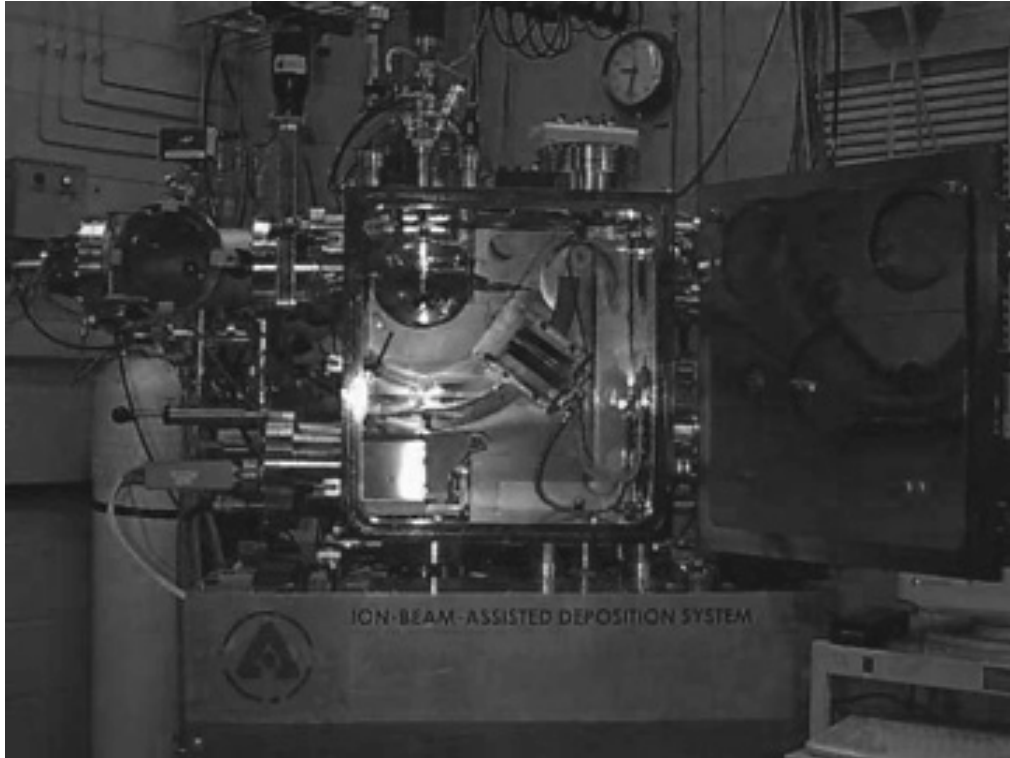
Fig. 8.   New IBAD-2 chamber for production of substrate layers for coated superconductors.
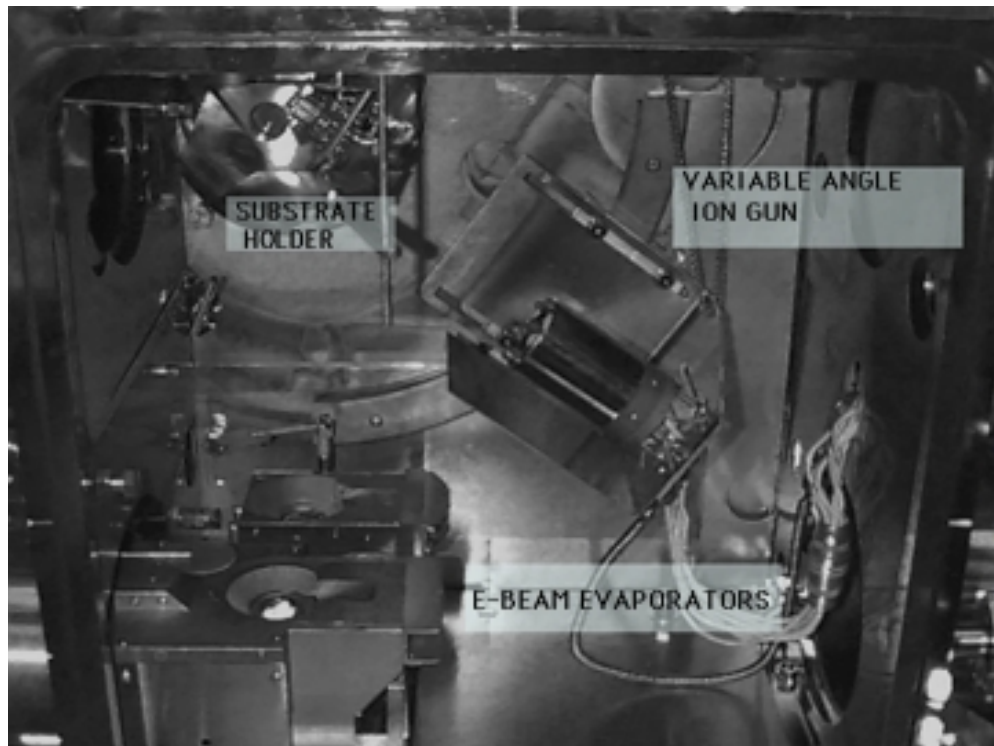
Fig. 9. Inside of new IBAD-2 chamber; key components are labeled.

minimal contamination and very little downtime for material changes. The system includes a hot stage with a maximum temperature of at least 900°C, which is higher than will be required for the substrates now being examined.

In both IBAD chambers, to improve the in-plane alignment of biaxially textured thin films of YSZ that are deposited by IBAD on flexible metal substrates, we have examined the effects of ion-to-atom arrival ratio (r-value). Texturing substrates by IBAD allows versatility in substrate selection; however, sputtering losses during deposition decrease film thickness and significantly affect processing time. We are therefore striving to better understand the processes involved in the development of ion-beam-induced (200) texture and to optimize deposition parameters to compensate for inherent shortcomings.

Previous work has firmly established that the degree of texture development in YSZ films produced by IBAD is primarily dependent on the ratio of ions to atoms, i.e., r-value, arriving at the substrate surface during processing. The r-value can be changed by varying the ion beam current density (I_b) and deposition rate. In the present work, film development was studied primarily by evaluating the degree of texture versus film thickness for various r-values, at a constant ion-bombardment angle of 55° from an 8-cm ion source with an ion-beam energy of 300 eV. The goal was to identify the optimal r-value for YSZ deposition.

As-received polycrystalline Hastelloy C was used as the substrate; 100-μm-thick Hastelloy C sheet was sheared into 1-cm^2 coupons and polished with diamond paste to a finish of 0.1 μm. The substrates were ultrasonically cleaned in acetone, and further cleaned by swabbing the surface with ethanol. Partially shielded Si substrates were placed adjacent to the Hastelloy C substrates so that film thicknesses could be determined accurately. The base pressure of the deposition chamber before ion bombardment was 10^{-7} torr, which rose to an operating pressure of 9×10^{-5} torr with initiation of the Ar and O_2 gas flow into the ion source. The O_2 flow rate was set to 10% of that of Ar.

The r-value was varied by changing I_b and measuring the corresponding ion fluence at the substrate surface by the Faraday cup. An accurate ion fluence, which varied between 3 and 7 μA, was ensured by proper positioning of a Faraday cup for each deposition. After generation of a steady ion bombardment, evaporation of the YSZ began. While focused onto the evaporation hearth, the power to the electron beam was initially held low to condition the YSZ. After conditioning, the power was steadily increased manually to the desired deposition rate displayed on the crystal quartz rate monitor. When a constant deposition rate and ion bombardment were ensured, IBAD was initiated. The deposition rate was varied from 0.4 to 2.0 Å/s, and all depositions were made to a thickness of 0.8 μm.

Biaxial texture was characterized with a Scintag four-circle X-ray diffractometer (CuKα radiation). Standard 2θ scans were used to determine any preferred crystalline orientation. The degree of out-of-plane texture was determined by the FWHM of Ω scans of the YSZ (200) reflection. In-plane texture was measured by the FWHM of φ scans of the YSZ (111) reflection. (111) pole figures were generated to map out extents of biaxial texture.

X-ray analysis was performed on the IBAD YSZ/Hastelloy C substrates. YSZ films deposited without ion assistance (r = 0) were essentially amorphous. Increasing r-values up to 1 induced a gradual increase in (111) preferred growth. The ions presumably provided sufficient surface mobility for the adatoms of YSZ to preferentially grow with a <111> direction normal to the surface. Studies on preferred growth of IBAD YSZ as a function of substrate temperature have shown formation of (111) at lower r-values and higher temperatures. Without the assisting ion beam or at low r-values, formation of (111) surfaces is most stable, whereas at larger r-values, the ion beam limits the mobility of adatoms and promotes growth of (200) surfaces.

Films produced at an r-value of 1.6 showed both (111) and (200) orientations; r-values above 1.6 produced (200) preferential growth. At high r-values, the intensity dropped because of the decreased film thickness that was a result of sputtering and concomitant X-ray penetration into the substrate. Figure 10 illustrates the effect of r-value on preferential growth of IBAD YSZ. It can be expected that the (200) orientation remains up to a critical r-value r_c, at which more material is sputtered away than deposited.

The degree of c-axis out-of-plane texture was determined by Ω scans performed on the (200) reflection. At r-values >2, all films with (200) preferred texture exhibited good c-axis alignment, with FWHM values to ≈5°. Previous studies on various substrate materials have shown that out-of-plane texture forms readily and is mostly dependent on the surface roughness of the substrate. This is expected because of growth rate anisotropy and the tendency toward columnar-growth structures in YSZ.

To quantify the degree of in-plane texture, we performed φ scans of the YSZ (111) reflection. Figure 11, a φ scan for a film with an r-value of 2.32, shows four symmetric (111) peaks. FWHM determinations of Gaussian curve fits were used to characterize the degree of biaxial texture.
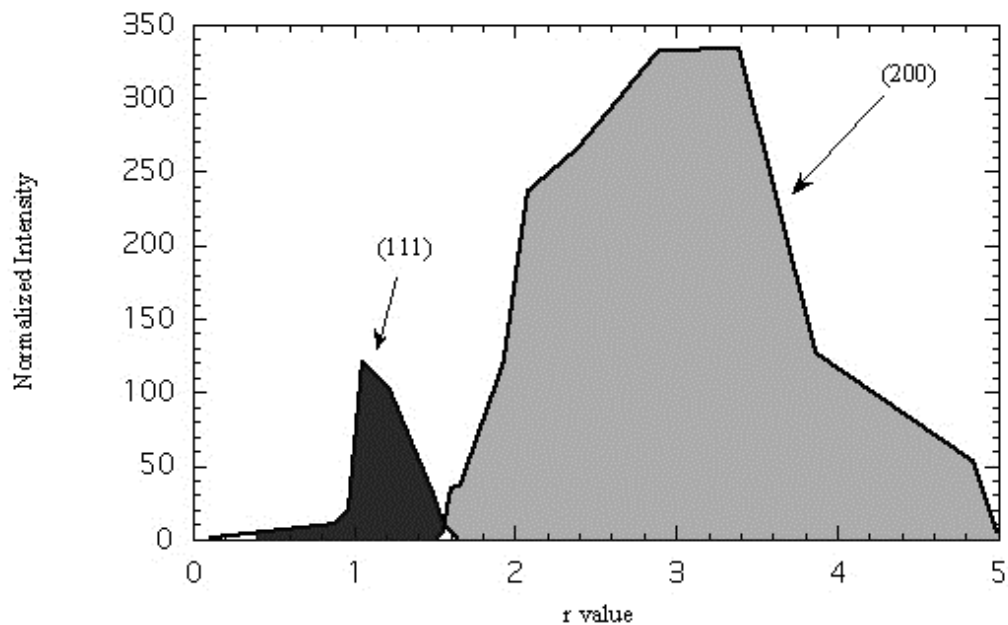
Fig. 10. *θ-2θ relative intensity as a function of r-value, illustrating zones of preferred orientation.*
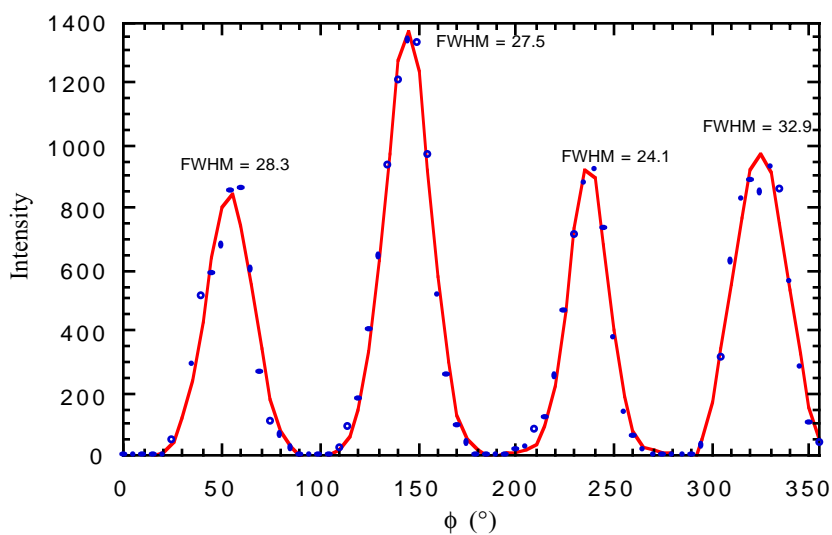
Fig. 11. *ɸ scan of IBAD YSZ film produced with r-value of 2.32, indicating in-plane biaxial texture.*

The in-plane texture of IBAD YSZ was studied for r-values of 1.4-6. Figure 12, a graph of FWHM as a function of r-value, reveals a steady improvement in texture with increasing r-value up to r ≈ 3. Thereafter, the increase of FWHM saturated with r-values of ≈6.

As the number of ions that hit the surface increases, more of them satisfy the criteria for ion channeling and contribute to an increase in anisotropic ion etching and overgrowth of crystallites having orientations other than those of the biaxially aligned YSZ (200) grains. Thus, increasing the ion flux allows the (200) faster-growing grains to grow and further align themselves with respect to the ion beam. It has been shown that the degree of in-plane texture increases asymptotically to the critical value r_c, where more material is sputtered away than deposited. Therefore, the degree of in-plane texture should also increase to a critical value.

The 8-cm ion source used in this work is capable of achieving an overall FWHM of ≈17°. However, glancing-angle X-ray studies have shown that surface textures are substantially sharper than those of the bulk, typically ≈9° less in the FWHM. This implies that an IBAD YSZ film produced with an in-plane texture of 17° would correspond to a surface FWHM of 8° and would therefore yield Y-123 films with J_c values of $> 10^6$ A/cm^2 at 77 K.

Film thicknesses on the partially shielded Si control samples are plotted as a function of r-value in Fig. 13. The decrease in thickness for an increasing r-value follows an approximate linear trend. From a linear fit, a calculated thickness, z_t, was used to determine the loss in thickness Δ, due to ion etching. Assuming an equal packing density for a film deposited without ion assistance, the number of atoms sputtered away n_a could be calculated for each deposition by the thickness loss $\Delta z = 1.64 - z_t$. The ion number density n_i was also calculated.

The sputter yield n_a/n_i for a 300-eV ion beam and bombardment angle of 55° as a function of r-value is shown in Fig. 14. The YSZ sputter yield increased rapidly with r-value, presumably because of the increased number of ions hitting the surface and dislodging YSZ surface atoms. The sputter yield rate of increase tapered off as the r-value approached the critical value r_c. We completed the study by constructing an IBAD YSZ texture/processing contour map (Fig. 15). Thickness and texture data were integrated to quantitatively map out the zones of preferred YSZ orientation. The two most easily changeable and important variables in the development of texture are the atomic and ion flux, better described as the deposition rate, and the ion current density. The data needed to generate relatively smooth contour lines (iso-FWHMs and iso-thicknesses) were calculated by fitting the experimental
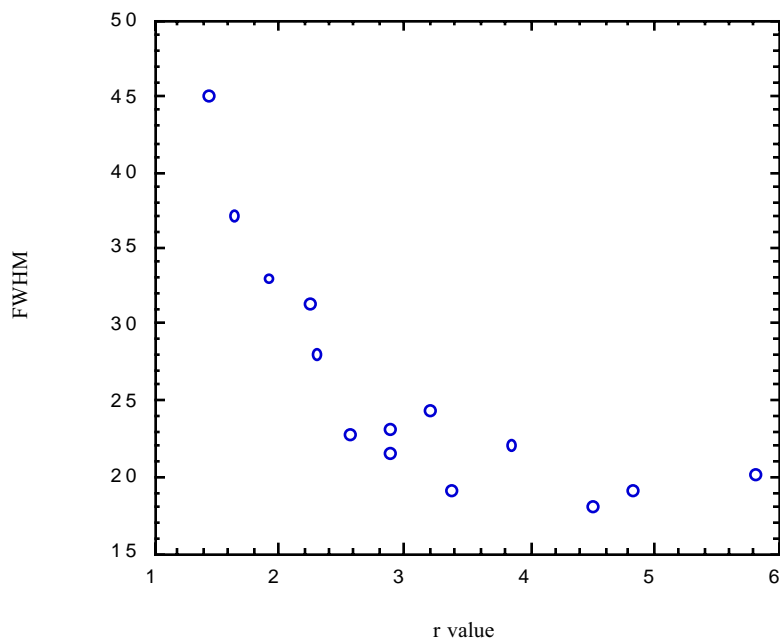
Fig. 12. Effects of r-value on in-plane texture of IBAD YSZ films.
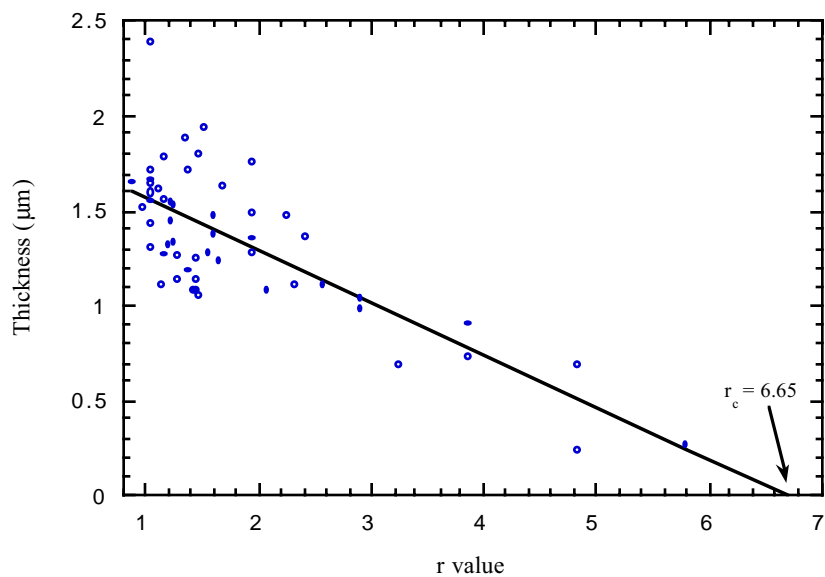
Fig. 13. Film thickness as function of r-value.
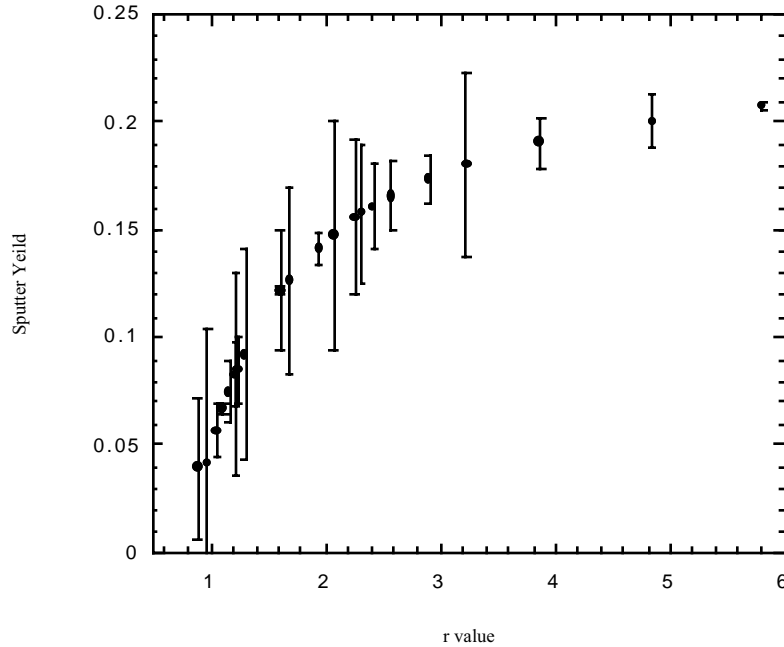
Fig. 14. Sputter yield of YSZ surface versus r-value for 55°, 300 eV Ar+ ion beam.

data to curve fits. The data within zones that were not heavily studied were generated by extrapolating appropriate individual curve fits. Most of the experimental data were gathered at deposition rates between 0.64 and 3.2 Å/s and at ion current densities between 150 and 350 $\mu A/cm^2$, at which the tendency for biaxial texture development was the strongest.

The zones that showed (111) and (200) preferred growth are shaded. The (200) preferred growth is presented as dark gray; it spans a large region and is present for r-values > ≈1.67. The (111) zone of preferred growth is marked by lighter gray and is found between the 1 and 1.67 r-value contour boundaries. There is little overlap of the (200) and (111) preferred growth that occurs at an r-value of ≈1.6. Thus, the small zone of (111) + (200) can be assumed to start at the (111) transition to the (200), proceeding to extend into and overlap a very small strip of the (111) zone. Low r-values of <1 produced YSZ films that were essentially amorphous. The boundary of transition from (111) to (200) preferred orientation approximately follows the 1.2 (1.67) thickness/r-value contour line. The (200) zone is present at $1.67 \leq r \leq r_c$, where $r_c \approx 6.65$ and marks the value at which sputtering overwhelms deposition.

15
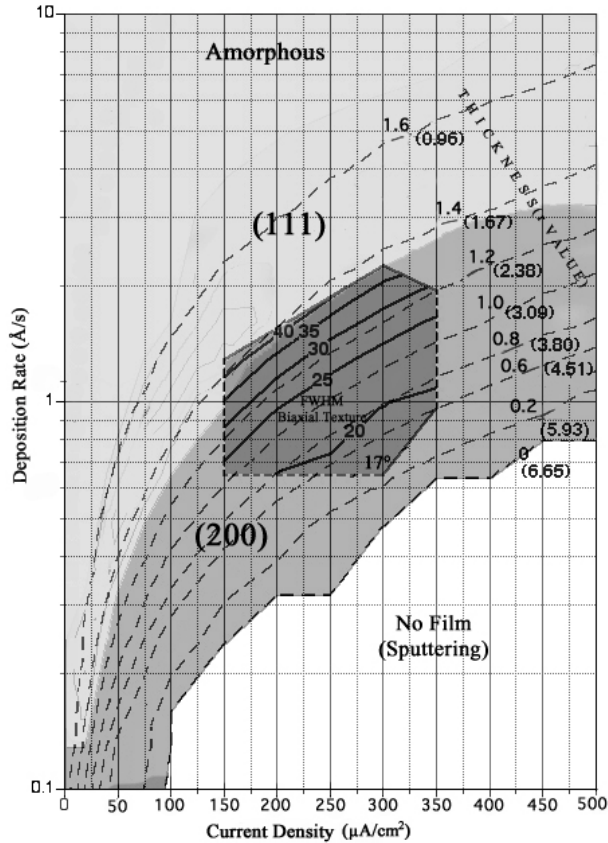
Fig. 15.   Orientation of YSZ as a function of IBAD processing conditions.

The contour of zero thickness at the r_c marks the boundary at which the atom arrival rate and etching rate reach unity, and preferred (200) film growth begins. However, this boundary is not as well-defined as the line suggests. The processing zone between the zero and 0.2 thickness contour boundaries was highly susceptible to ion bombardment. Such high r-values introduced increased amounts of ion damage and stress between the film and substrate and was evident by visual inspection that revealed poor cohesion and delamination of the films deposited within this zone.

The region marked with heavy lines within the (200) zone represents biaxial texture development. Contained in this area are iso-FWHMs (lines of equal biaxial texture). FWHM data were obtained from films produced with ion current densities of 150–350 $\mu A/cm^2$. No FWHM data were obtained for very low deposition rates, which require excessively long processing times to reach the 1.6 μm thickness criterion. Thus, the dashed borders represent the cutoff of data analysis. However, the biaxial texture zone can be expected to extend past the dashed regions following the isolines, eventually being pinched off at an r-value of ≈3, which corresponds to both low and high deposition-rate and

current-density coordinates. This zone can be expected to extend through the (200) zone and terminate at the r_c contour boundary.

To improve the J_c values of Y-123 thin films on flexible metallic substrates, films have been deposited on textured buffer layers. Electron microscopy has been used to investigate the microstructure, grain size, thickness, and crystal orientation of these buffer layers before Y-123 deposition, with the goal of optimizing texture. Y-123 films deposited on the optimized layers were also examined by electron microscopy.

SEM was performed in a Hitachi S4700 field-emission-gun microscope. Samples were prepared by either fracturing the specimen and examining it as-is or after mechanical polishing. TEM was carried out in a Philips CM30. Plan-view TEM specimens were prepared by mechanical grinding, dimpling, and ion-milling from the undeposited side of the sample. Cross-sectional TEM specimens were prepared by gluing two pieces of deposited material face-to-face, followed by mechanical grinding, dimpling, and ion-milling.

Biaxially textured YSZ buffer layers were deposited on randomly oriented Hastelloy C and 304 stainless steel substrates by IBAD. Deposition was at room temperature with varying ion-to-atom arrival ratios (r-values).

A cross-sectional TEM image of a YSZ film with an r-value of 2.8, grown on Hastelloy C, is shown in Fig. 16. It can be seen that the microstructure of the YSZ film consists of columnar grains that increase in width as the film becomes thicker. SAED patterns were obtained at four points in the film, shown in the figure as points A, B, C, and D. The pattern at the bottom of the film (A) indicates a randomly oriented polycrystalline film that gradually changes as the film becomes thicker, whereas the pattern at the top (D) demonstrates preferred texture. These results indicate that grains that are aligned favorably with the ion source dominate the structure as the film grows.

Good results have been obtained when Y-123 has been deposited on YSZ buffer layers. Figure 17 is an SEM image of YSZ on which a CeO_2 cap layer was deposited, followed by Y-123. The image was acquired with backscattered electrons, to observe differences in elemental composition. Figure 18 is a cross-sectional TEM image of the same sample; it shows that crystalline Y-123 was deposited.
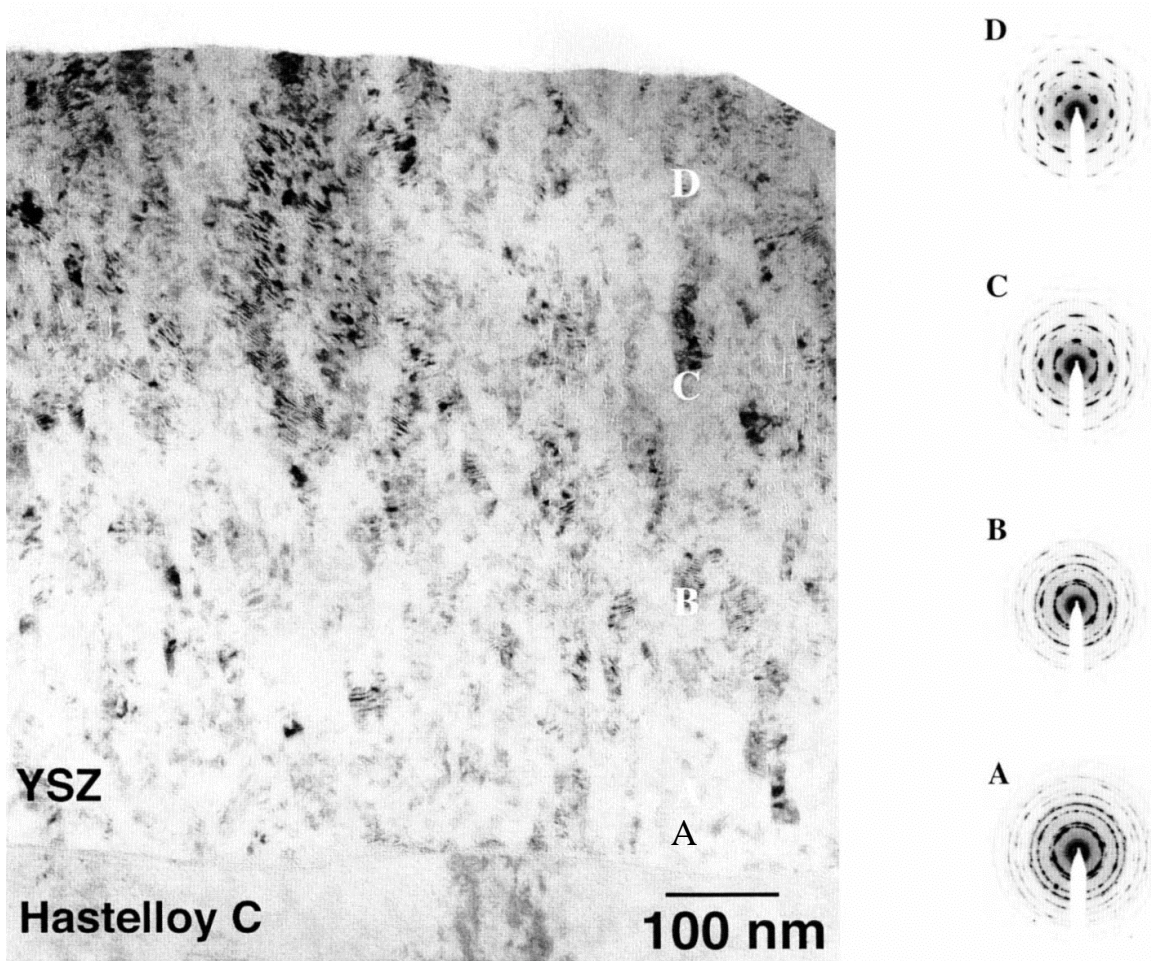
Fig. 16.   Cross-sectional TEM photomicrograph of IBAD YSZ layer on Hastelloy C substrate and SAED patterns from various regions.

2.1.2 Pulsed Laser Deposition of Y-123

A PLD system consisting of a 30.5-mm-diameter deposition chamber, 5.1-cm-diameter substrate holder (950°C maximum temperature capability), and Lambda Physik KrF excimer laser (248 vm) was comissioned in FY2000. Figure 19 shows the PLD system in operation. Y-123 films ($\approx$1 μm thick) were deposited on single-crystal substrates and Hastelloy C buffered by layers of ISD MgO, IBAD YSZ, and various cap layers, such as CeO_2.

For most of the Y-123 film PLD, the excimer laser pulse width was 25 ns; the pulse energy, 160 mJ; the pulse repeat rate, 8 Hz; and the oxygen pressure, 250 mtorr. These conditions produced a growth rate of $\approx$0.25 nm/s. For deposition of the CeO_2 layer, 1 Hz and 300 mtorr of oxygen pressure were
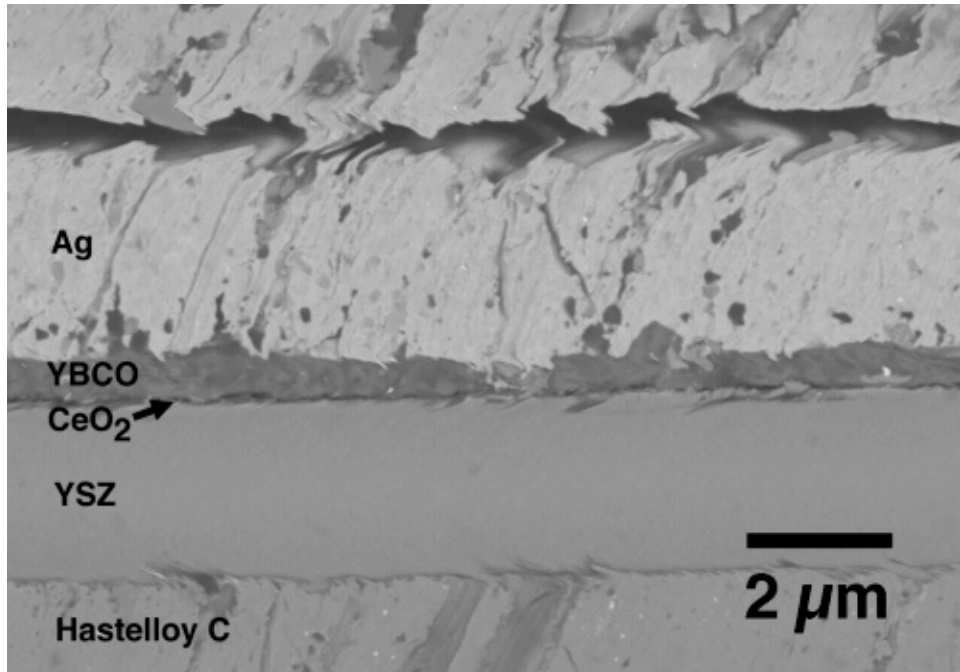
Fig. 17. SEM photomicrograph of Y-123 coated conductor, with YSZ deposited by IBAD.
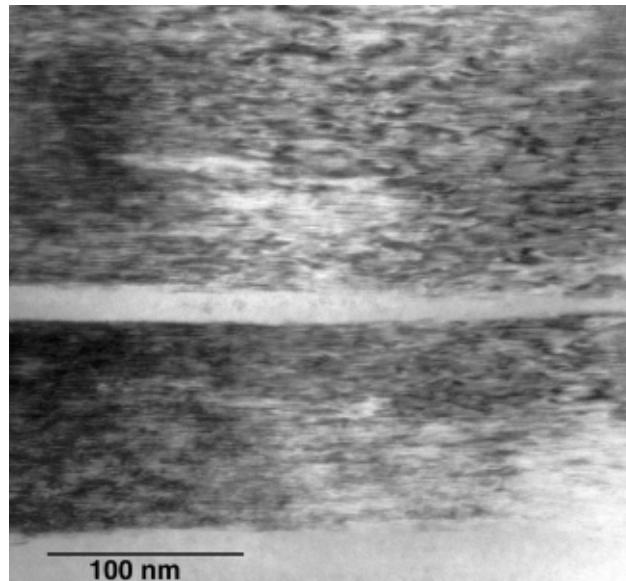
Fig. 18.   Cross-sectional TEM photomicrograph of Y-123 layer on CeO$_2$/YSZ/Hastelloy C substrate.
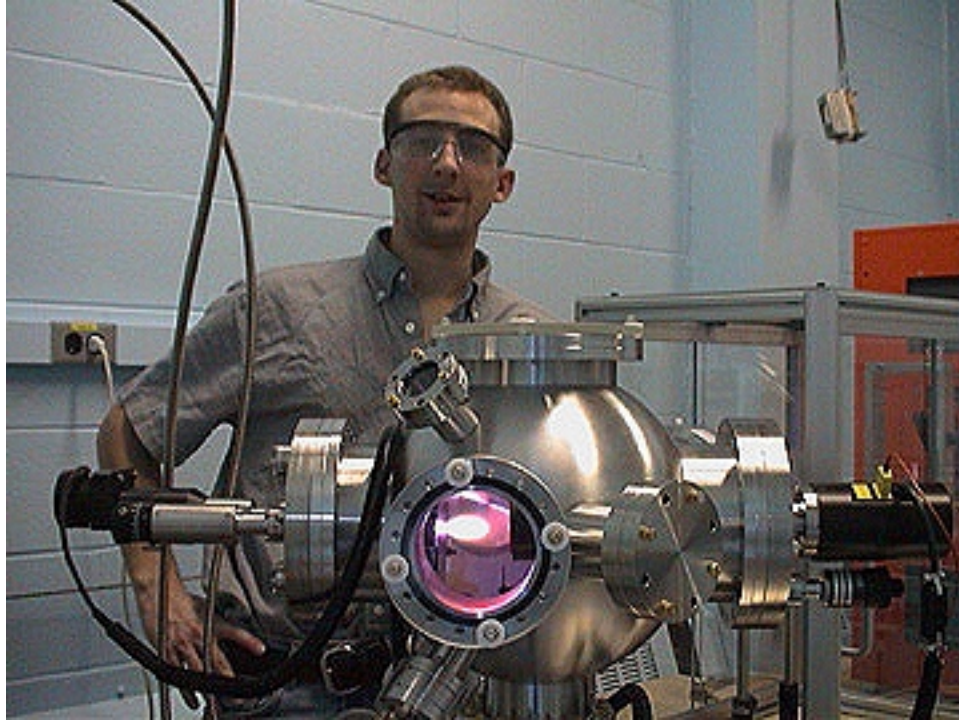
Fig. 19. PLD system in operation.

used. Substrates were mounted with Ag paste to a heated sample stage. Targets were rotated during deposition, and distance between the target and the substrates was 7.5 cm.

Three types of substrates were used for the deposition of Y-123 thin films:

(001)-oriented $LaAlO_3$ (LAO) single crystals for initial optimization of the growth conditions; Hastelloy C substrates coated with biaxially textured YSZ buffer layers that were deposited by IBAD, and Hastelloy C substrates with biaxially textured MgO buffer layers grown by ISD.

Film structures were examined primarily by SEM and X-ray diffraction pole figures and ϕ scans. T_c and J_c values for all films were measured inductively. For some of the films, transport J_c was also measured, with or without an applied magnetic field. For the transport measurements, a Ag film ≈ 2 μm thick was coated on the Y-123, and the composite films were annealed for 2 h in O_2 at 450–500°C.

Y-123 Films Grown on (001) LAO Substrates

Y-123 films were deposited on (001) LAO substrates at substrate temperatures (T_s) of 745, 755, 765, 770, 780, 790, 800, and 810°C to optimize deposition temperature, oxygen pressure, and annealing conditions (Table 1). The thickness of the films was ≈0.3 μm for a 22-min deposition. Several 1-μm films were also deposited to achieve higher I_c and J_e values.

X-ray diffraction confirmed the c-axis-oriented growth of the films. In the temperature range that we studied, a higher deposition temperature led to a higher T_c in the resultant Y-123 film. The best T_c and J_c values were obtained at $T_s = 790$°C: $T_c = 90$ K, transition width (ΔT) = 0.2 K, inductive $J_c > 3.3$ MA/cm^2, and transport $J_c = 2.4$ MA/cm^2. For example, Fig. 20 shows the transport I_c results of a Y-123/LAO film (Sample 0530A, 1.0 μm thick, width = 5 mm) deposited at 790°C, with inductive $J_c = 0.8$ MA/cm^2.

Y-123 films with a thickness of 1 μm exhibited J_c values of 0.7-0.8 MA/cm^2, much lower than the 2.4 MA/cm^2 obtained on 0.3-μm-thick Y-123 film. Similar thickness dependencies have been reported by many others.

Table 1. Superconductivity data for Y-123/LAO films

Sample Number	T_s (°C)	Thickness (μm)	T_c (K)	ΔT_c (K)	Inductive J_c (MA/cm^2)	Transport J_c (MA/cm^2)
0731A3	745	0.3	85.0	>2.0	1.0	-
0728A3	755	0.3	86.0	0.8	2.6	-
0714A1	765	0.3	86.2	0.9	3.0	0.3
0717A2	765	1.0	86.0	0.8	>1.0*	0.7
0421A1	770	0.3	86.4	0.8	1.8	-
0509A	780	0.3	87.1	0.6	-	-
0530A	790	1	86.0	0.2	-	0.8
0517A2	790	1	89.9	0.4	-	0.7
0720A1	790	0.3	88.0	0.5	>3.3*	to be done
0508A1	800	0.3	87.0	0.6	2.77	2.4
0727A2	810	0.3	90.5	1.5	2.3	to be done

*J_c value exceeded range of inductive system.
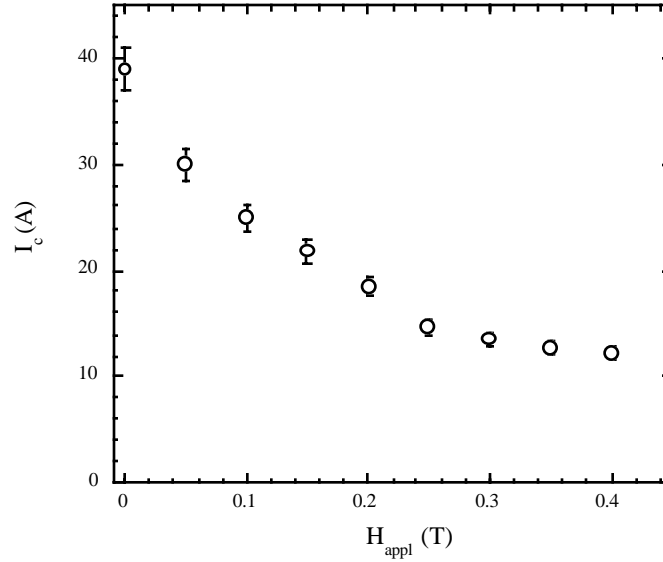
Fig. 20.   Y-123/LAO films (0530A, 1.0 μm thick, width = 5 mm) deposited at 790°C. Inductive J_c = 0.8 MA/cm^2; also, J_c under applied magneic field.

Y-123 Films Grown on YSZ(IBAD)/Hastelloy C

Y-123 films were grown on YSZ(IBAD)/Hastelloy C substrates at various temperatures (Table 2). The c-axis orientation and biaxial textures of Y-123 films were confirmed by pole figure analysis on these films (Fig. 21). The FWHM values of the φ-scan peaks of the films are 15-18° and 18-22° for Y-123 and YSZ layer, respectively. Typical T_c values were 88 K, the transition width was ≈2 K, and J_c values were ≈0.2 MA/cm^2. Better texture will be required to obtain higher J_c values.

Table 2. Properties of Y-123/YSZ/HC films

Sample Number	T_s (°C)	Thickness (μm)	T_c (K)	ΔT_c (K)	Inductive J_c (MA/cm^2)*	Transport J_c (10^5A/cm^2)
0526A	735	0.3	87.0	3.3	-	1.2
0525C	745	0.3	88.5	2.5	-	2.5
0524A	755	0.3	88.2	3.8	-	-
0523A	765	0.3	86.8	~5.5	-	1.2

*No suitable conversion constant is available for Y-123/metal film to deduce the inductive J_c value.

22
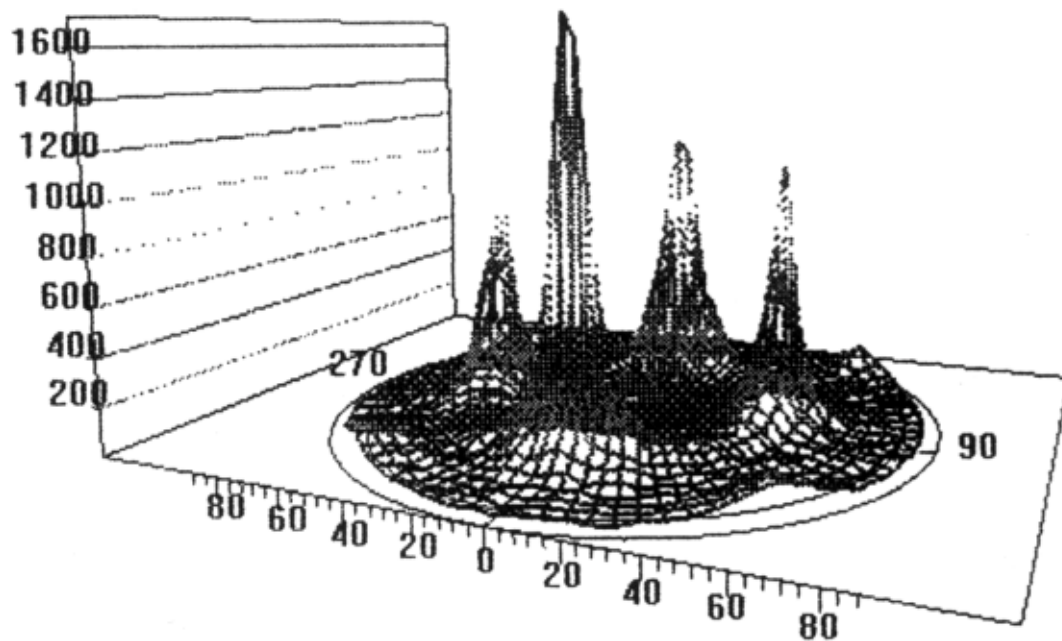
(a)
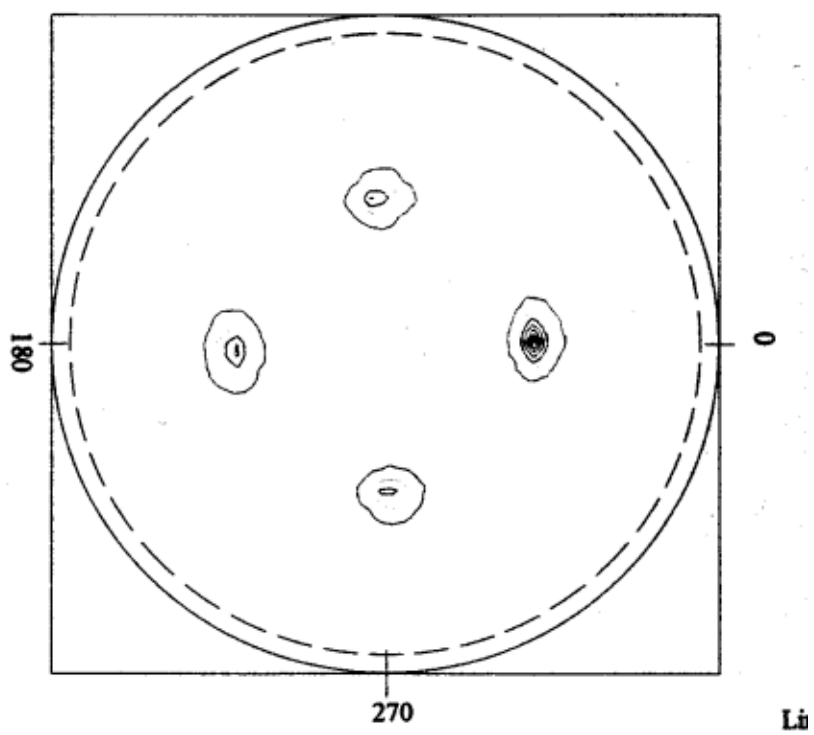
(b)
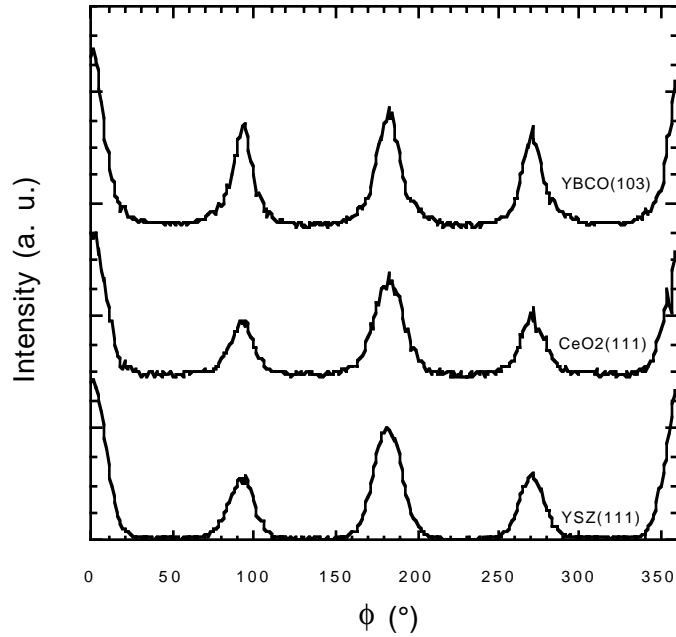
(c)

Fig. 21.   Pole figures (a and b) and φ scans (c) of Y-123/CeO₂/YSZ/HC films (0607A2), FWHM ≈15-18° for Y-123(103) and 18-22° for YSZ(111).

To improve the lattice match between the Y-123 film and the YSZ buffer layer, a CeO$_2$ buffer layer was deposited on YSZ/HC by PLD (Table 3). By depositing the CeO$_2$ buffer layer, the Y-123 (100) orientation can be eliminated (Fig. 22) and T$_c$ can be increased to ≈90 K.

Y-123 Films Grown on MgO(ISD)/HC Substrates

Y-123 films were deposited on MgO(ISD)/HC substrates. Buffer layers of CeO$_2$, SrTiO$_3$ (STO), and/or MgO were deposited to improve the surface smoothness and the lattice match between Y-123 and the ISD MgO layer. The films that have been produced are listed and described in Table 4. Analyses are in progress.

X-ray pole figure measurement of the Y-123/STO/MgO(PLD)/ MgO(ISD)/HC reveals clear biaxial texture for both the Y-123 and the MgO (ISD) layers (Fig. 23). The tilt angle derived from the pattern of the MgO layer and of the Y-123 film is 30°.

Table 3. Properties of Y-123/CeO$_2$/YSZ/HC films

Sample Number	T$_S$ (°C)	Thickness (µm)	T$_c$ (K)	ΔT$_c$ (K)	Inductive J$_c$ (MA/cm^2)*	Transport J$_c$ (10^{5}A/cm^2)
0609A2	750	0.3	90.0	5.0	-	1.2
0607A2	755	0.3	88.0	4.8	-	-
0612A2	755	0.3	90.0	5.0	-	1.0
0622A1	755	0.3	90.5	3.2	-	-
0621A	765	0.3	87.0	2.0	-	1.5
0627A	775	0.3	88.0	3.3	-	-

*No suitable conversion constant is available for Y-123/metal film to deduce the inductive J$_c$ value.
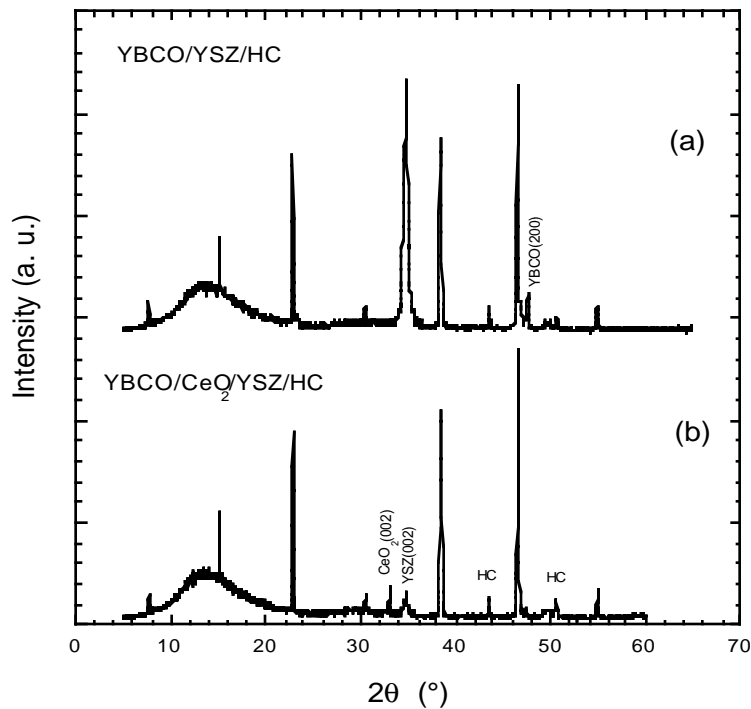
Fig. 22. 2θ diffraction pattern of Y-123/YSZ/HC and Y-123/CeO$_2$/YSZ/HC samples; Y-123 (l00) peaks have been eliminated by growth of CeO$_2$ buffer layer.

25

Table 4. Y-123 films grown on MgO(ISD)/HC substrates

Films	Description
Y-123/MgO(ISD)/HC	ISD MgO biaxially textured layer only
Y-123/CeO$_2$/MgO(ISD)/HC	Additional CeO$_2$ buffer layer introduced
Y-123/STO/MgO(ISD)/HC	Additional STO buffer layer introduced
Y-123/STO/MgO/MgO(ISD)/HC	Additional MgO and STO buffer layer introduced by PLD

To date, T_c values have been <77 K; therefore no J_c values have been measured. Clearly, either the MgO surface must be improved through cleaning and annealing and/or buffers will be needed between the MgO and the Y-123.

With respect to future work, the IBAD will focus on decreasing the FWHM. Successful ISD will require improvement in the matching of Y-123 to MgO. Annealing conditions must also be optimized for the Ag coatings on Y-123 thin films.

2.1.3 Y-123 Films from a Solution Process

Various processing methods have been investigated to achieve high J_c values for coated conductors on metallic substrates. Metal-organic decomposition (MOD) or sol-gel processes, which are performed in nonvacuum environments, offer great promise because they are cost-effective and easily scalable. Solution techniques are now being studied by many researchers, and good results have been obtained. A MOD process based on trifluoroacetate (TFA) has produced some of the highest J_c values of all the solution techniques. However, its application to metallic substrates has not been consistently successful, mostly because we lack a full understanding of the processing conditions and their relationships to resultant structures and properties. We are now working on systematically optimizing the parameters of the TFA process. LAO single crystals are being used as the substrate. With the idea of the application to metallic substrates, we are concentrating especially on lowering heat treatment temperatures.

Solutions have been prepared in an ambient atmosphere. Metal acetates of Y, Ba, and Cu were weighed to a 1:2:3 ratio, dissolved in trifluoroacetic acid, and refluxed for 4 h. The resultant solution was dried in air to evaporate the

(a)

(b)
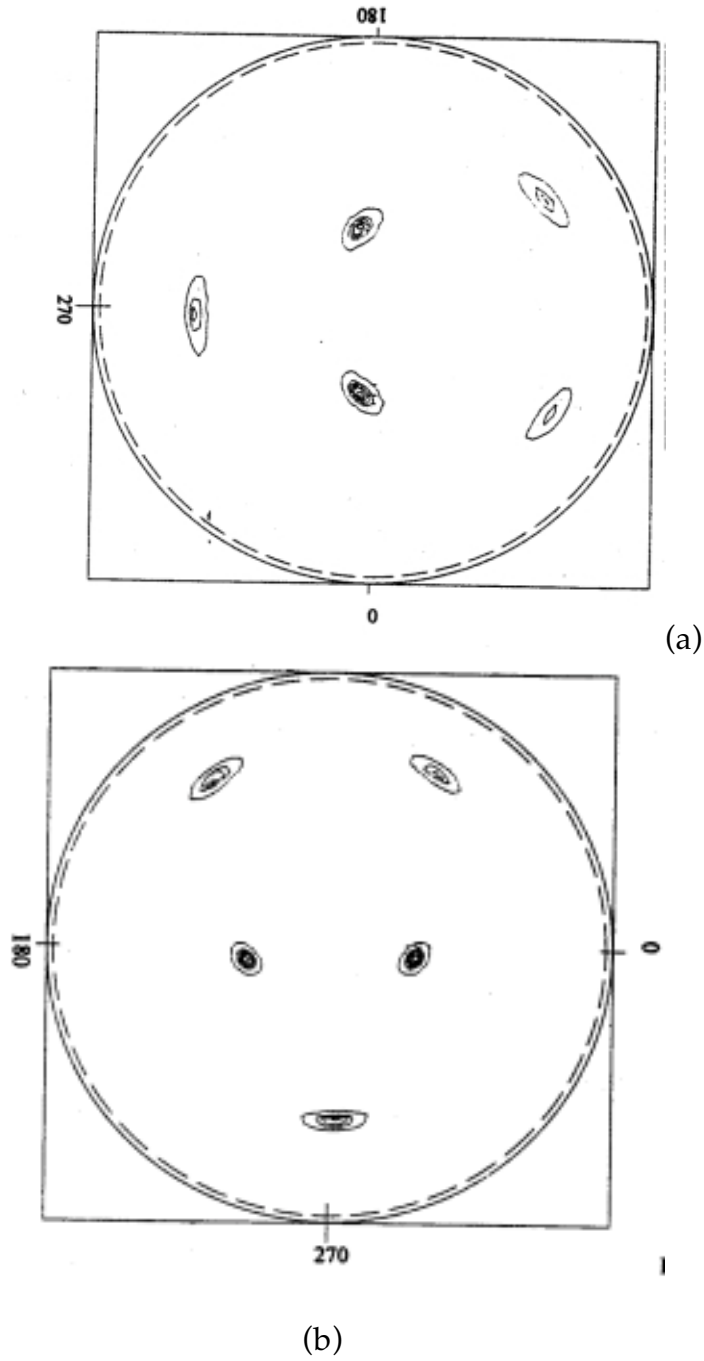
Fig. 23. Pole   figure   patterns   of   (a)   MgO(220)   plane   and   (b)   Y-123(103)   plane   of   Y-123/STO/MgO(PLD)/MgO(ISD)/HC sample.

solvent and obtain a solid blue residue. This residue was then easily dissolved in methanol. We brought the total cation concentration to 1.5M and used this methanol-based solution in our experiments.

The solution was coated on LAO single crystals by dip- or spin-coating. The precursor film was converted to an epitaxial Y-123 film through two heat treatments. During the first treatment at low temperature, a uniform solid film containing substantial fluorine formed. An epitaxial Y-123 film was then developed and the fluorine was eliminated by a second heat treatment, in Ar at higher temperatures. Four maximum temperatures, ranging from 720 to 780°C, were studied. After the heat treatments, the composition of each final Y-123 film was determined by atomic emission spectroscopy. T_c was measured inductively. Microstructure and texture were evaluated by SEM, conventional X-ray diffraction, rocking curves, and ϕ scans.

Microstructures of representative samples are shown in Fig. 24, which reveals many pores and small particles. The presence of pores and small particles is typical of films fabricated by a post-annealing process. The films prepared at 720°C (Fig. 24a) and 740°C (Fig. 24b) consisted of several layers of c-plane and acicular, a-axis-oriented grains. The main texture of all of the films was perpendicular to the c-axis. As can be seen in Fig. 24c, the 760°C sample exhibited few a-axis grains, indicating that the texture is improved at this temperature. In the film prepared at 780°C (Fig. 24d), numerous large particles, rather than acicular grains, were observed, and the Y-123 layers below the particles appeared to be smoother than in other samples. The large particles were Cu-rich, which suggests that a CuO-rich liquid phase begins to form at ≈780°C, enhancing growth of c-axis-oriented grains.

Sharp T_c transitions were observed in films prepared at 740 and 760°C. Thus, for processing in Ar, temperatures between 740 and 760°C are considered optimal for the formation of the Y-123 phase.

Figure 25 shows (004) and (005) peaks of Y-123 films prepared at 720, 740, 760, and 780°C; the location of the strong (111) peak is marked by an arrow, but the peak itself is absent. The films were highly textured, in spite of the frequently observed a-axis grains. However, impurity peaks, which are considered to arise from second phases, were also observed in the diffraction patterns.

In addition, the FWHMs of ϕ scans and rocking curves were measured to evaluate in-plane and out-of-plane textures. Figure 26 shows (113) ϕ scans of films prepared at 740 and 760°C. The FWHMs of the (113) peaks for both films were <1°, indicating strong c-axis alignment of the grains. The FWHMs of
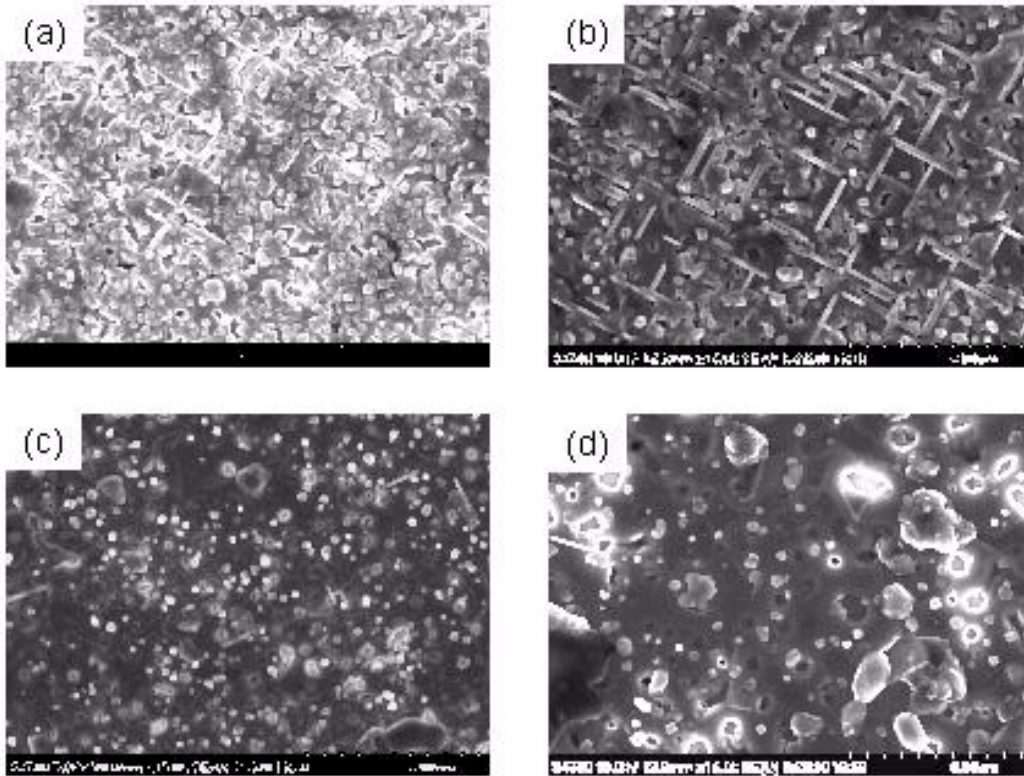
Fig. 24. SEM photomicrographs of samples prepared at (a) 720, (b) 740, (c) 760, and (d) 780°C.

rocking curves of the (002) peak were <0.5° (Fig. 27). These are excellent values when compared with those found in the literature. In addition, the maximum heat treatment temperature in our study was relatively low when compared with previously reported temperatures, which augurs for successful adaptation of this TFA process to coated conductors.

2.1.4 Grain Boundaries in Y-123

There is evidence that the J_c of grain boundaries (GBs) in HTSs does not drop as quickly with magnetic field H as might have been expected from a simple Josephson junction model. We have demonstrated that in very low fields, pinning of Josephson vortices by the meandering of thin-film, [001]-tilt, bicrystal GBs in Y-123 enhances J_c. However, as the spacing between Josephson vortices decreases in higher fields, this long-wavelength pinning potential due to meandering becomes less effective. Gurevich and Cooley
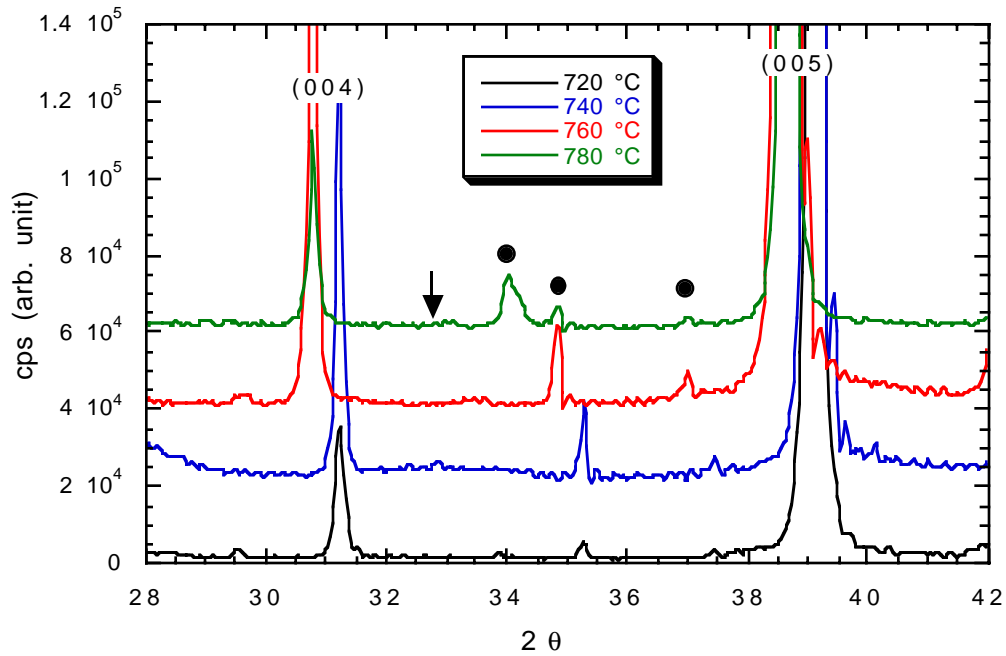
Fig. 25. X-ray diffraction spectra that show strong texturing. Arrow indicates location of (111) peak, filled circles indicate extraneous phases.

(A. Gurevich and L. D. Cooley, Phys. Rev. B 50 [1994] 13563) have proposed a new mechanism for an enhanced GB J_c arising from pinned Abrikosov vortices in the banks of a GB. These pinned Abrikosov vortices present a static, quasiperiodic pinning potential to pin GB vortices. The calculations of these vortices, which predict, e.g., a peak in $J_c(H)$, are restricted to low fields, but the central concept can be extrapolated to higher fields. The conceptual extrapolation leads one to expect that the spacing of Abrikosov vortices will be optimal for all fields that are well above the flux entry field H_{c1}. A peak in $J_c(H)$ is not uncommon in melt-textured and single crystal Y-123 materials that are made without intentional GBs. However, we are unaware of such direct experimental evidence for GB transport.

Magnetization data on the same sample are consistent with features of the J_c hysteresis when interpreted in this framework, including the irreversibility field, above which the internal flux profiles are nearly the same for FC and ZFC (Fig. 28). A necessary expectation above the irreversibility field is that the GB transport should be indistinguishable, and our data
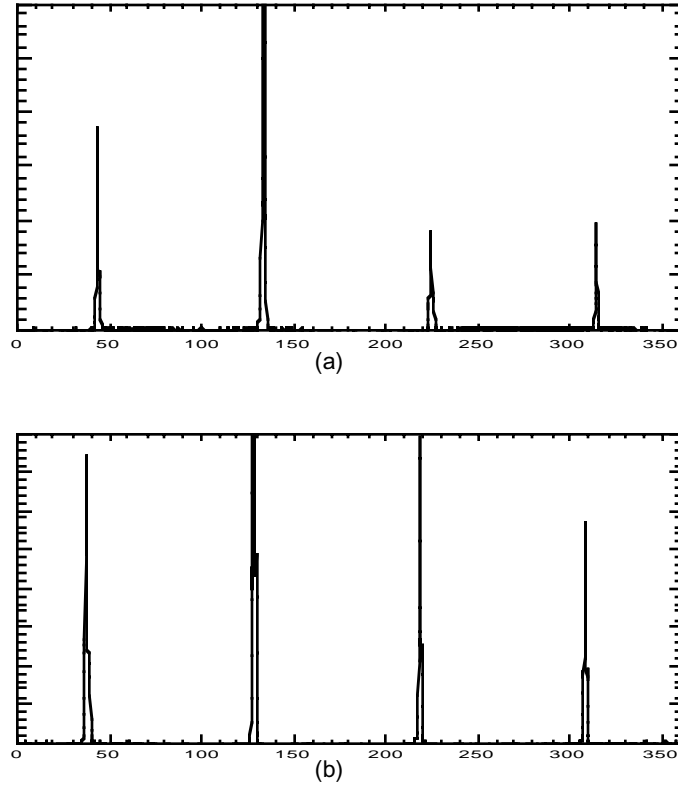
Fig. 26. ϕ scans of (113) Y-123 peak of TFA-derived films produced at (a) 740 and (b) 760°C; FWHM values are <1°.

confirm this. Finally, in the ZFC case, after a sufficiently high current is applied so that vortices can be both injected in the banks and exhibit flux creep, the J_c of the GBs is significantly and permanently increased. This result is consistent with the additional flux penetration caused by the supercritical current in the banks, although the full J_c value for FC is generally not achieved.

The focusing of flux along the GB, caused by field expulsion from the banks, is an alternative explanation that shares many of the above-noted characteristics. Although flux focusing can explain the low-field (≈100 Oe) hysteresis in granular materials, the hysteresis in our data extends to much higher fields. If our data are interpreted as being due to flux focusing, they imply a focused field of ≈0.1 T at the GB for applied fields of only ≈30 Oe. In coated conductors that are limited by GB transport, this result implies that a significant increase in I_c can be attained by introducing Abrikosov vortices into the grains near the GBs.

31
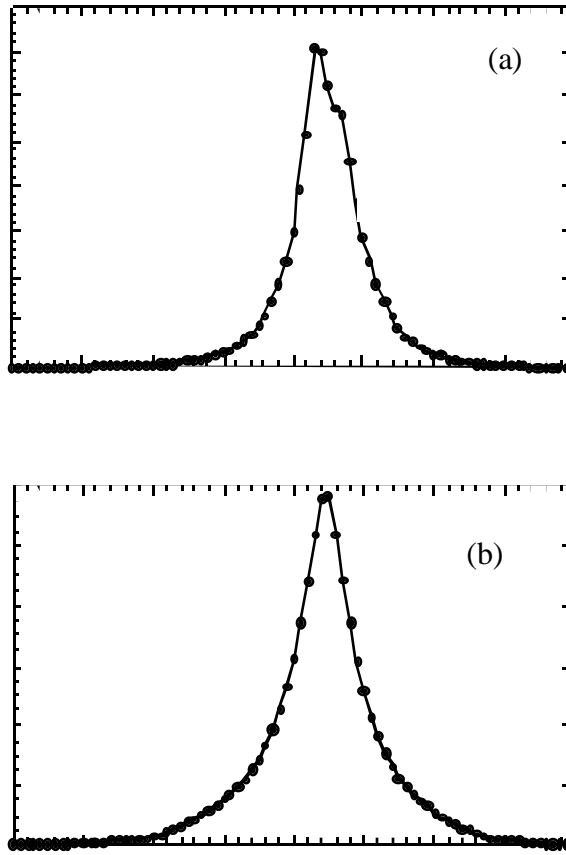
*Fig. 27. Rocking curves of (002) peak of films produced at (a) 740
and (b) 760°C; FWHM values are <0.5°C.*

We first report data on GBs among bulk materials that show a peak in $J_c(H)$ and an unusual hysteresis, findings that significantly support the central concept of the Gurevich-Cooley model. At high fields, this support comes from analyzing the history dependence of $J_c(H)$ and the field profiles found in these bulk materials. In collaboration with R. Feenstra and D. K. Christen of the Solid State Division at Oak Ridge National Laboratory, we obtained additional critical current data on bicrystal GBs. The data exhibited a peak in the GB critical current, $I_{cb}(H)$ and an unusual inverse hysteresis. The results provide additional support to the mechanism proposed by Gurevich and Cooley for an enhanced GB critical current. Further support for the Gurevich-Cooley model arises from the history dependence of $I_{cb}(H)$ and the field profiles found in these bulk materials. As stated previously, we have measured $I_{cb}(H)$ of the GB either after FC of the sample in an applied field H
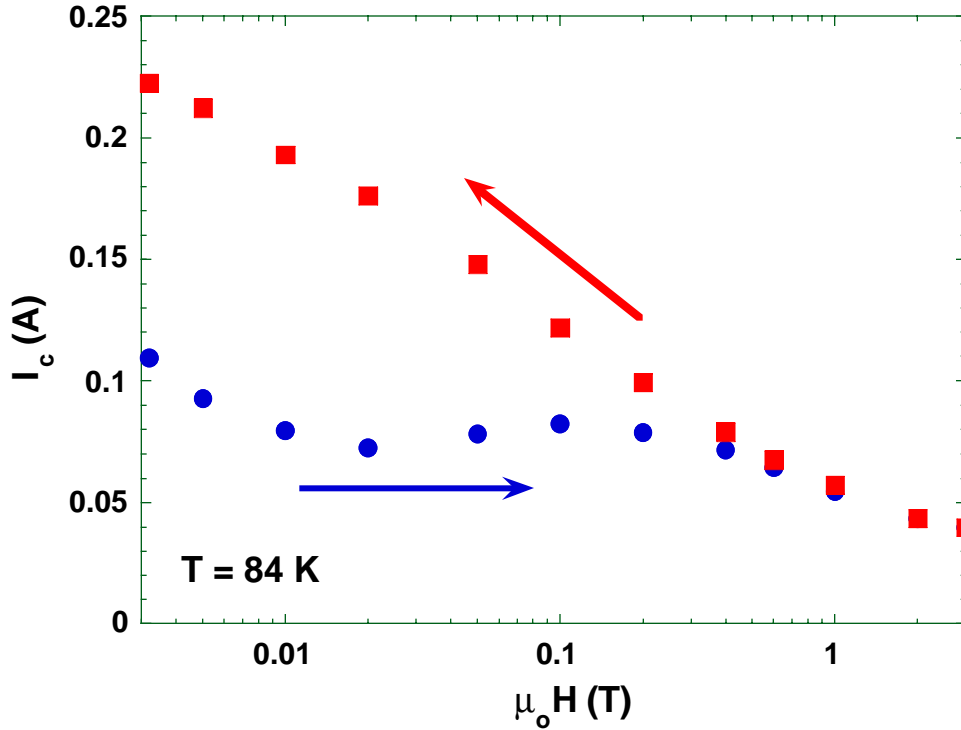
Fig. 28. Data for critical current through bulk 90º [100]-tilt GB: circles = zero-field-cooled (ZFC); squares = field-cooled. GB irreversibility point corresponds to that of grains as measured by magnetization. Unusual inverse hysteresis and peak effect for ZFC data are consistent with model of Gurevich and Cooley.

to a temperature T from above the transition temperature T_C; or after increasing H after ZFC to T (Fig. 29). In low fields, the GBs exhibit a higher I_{cb} for FC, which is just the opposite of the usual hysteresis for the grains of bulk materials (in which the greater internal fields associated with FC decrease the pinning and thus I_{cg}). However, this is exactly the expectation of the Gurevich-Cooley model for GBs, because FC provides a higher Abrikosov vortex density in the banks that can more strongly pin GB vortices.

2.1.5 Additional Microstructural Studies of Coated Conductors

Characterization at the Advanced Photon Source

During FY 2000, we initiated studies aimed at developing and applying synchrotron-based X-ray diffraction, scattering, and spectroscopy methods to coated conductor substrates, buffer layers, precursors, and fully processed
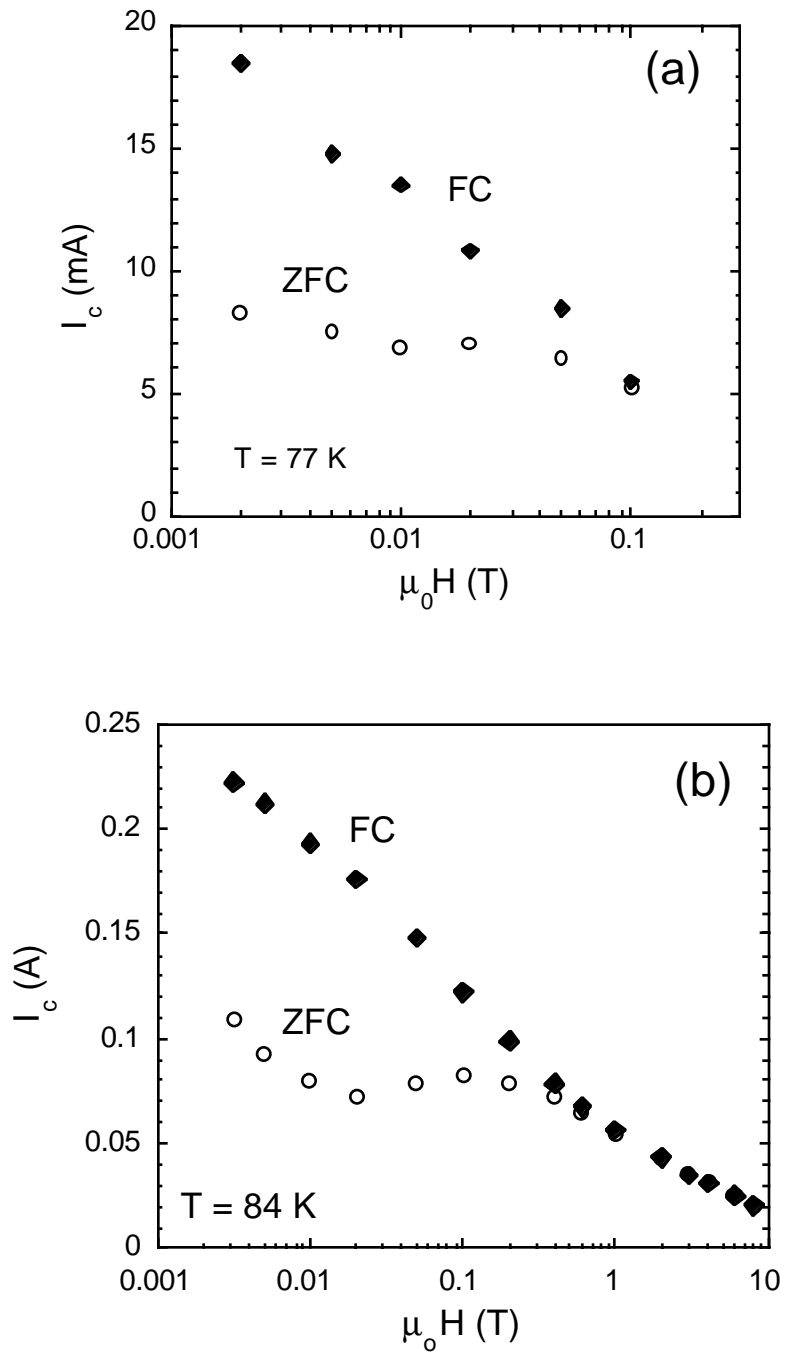
Fig. 29. I$_{cb}$ data for FC and ZFC for GBs in Y-123; data obtained from (a) 11° [001] tilt GB in coated conductor and (b) 90° [100]-tilt GB in bulk sample.

samples. This work is being done at the ANL Advanced Photon Source (APS); it makes use of capabilities available at the Materials Research Collaborative Access Team insertion device beamline located at Sector 10 (10-ID) of the APS. The X-ray beam at 10-ID is high intensity ($>10^{13}$ photons/sec), highly collimated ($\approx 0.002°$ beam divergence), and tunable over a wide energy range (5-90 keV). The beamline is currently equipped with a well-instrumented X-ray spectroscopy bench and an 8-circle Huber goniometer that provides better than $0.02°$ resolution of diffraction lines in the $\theta/2\theta$ mode. Examples of some of the capabilities we are attempting to exploit for the detailed characterization of coated conductor embodiments during various stages of fabrication/processing are given below.

The diffraction pattern in Fig. 30 was obtained from a Y-123/CeO_2/YSZ/Inconel coated conductor sample on a coated substrate embodiment produced by the IBAD method, with the Y-123 applied by PLD. The pattern, recorded in 15 min with an unattenuated 11-keV beam ($\lambda = 1.1271$ Å), covers the 2θ range of the first ten $[0,0,l]$ diffraction lines of Y-123 (many of which have saturated the detector), as well as specific diffraction lines for the underlying CeO_2 and YSZ buffer layers and the Inconel substrate. Detecting the strongest of the $[0,0,l]$ reflections of well-textured Y-123 is normally not difficult with a modern laboratory X-ray source, but detecting the underlying buffer and substrate diffraction lines becomes more difficult as the Y-123 layer becomes thicker. The appearance in Fig. 30 of non-$[h,0,0]$ diffraction lines for the substrate and buffer layers (albeit only weakly in some cases) has implications for the texture of the templating architecture that underlies the Y-123 layer. Raman microspectroscopic examination of this sample revealed no evidence of second phases and none were detected in the diffraction pattern of Fig. 30.

The patterns in Fig. 31 were obtained from Y-123 films supported on LAO single-crystal substrates, with the Y-123 layers formed by heat treatment of dip-coated TFA precursors. From a correlation with Fig. 30, it is clear that most of the diffraction lines for patterns YJ21 and YJ38 in Fig. 31 are due to $[0,0,l]$ lines of c-axis textured Y-123. However, the pattern for film YJ21 shows evidence of the presence of additional phases, as indicated in the scale-expanded segments of the pattern shown in Fig. 32. For the X-ray wavelength used in this measurement (1.1271 Å), most of the types of second phases one might expect to encounter for a TFA-based Y-123 film have the strongest diffraction lines in the 2-θ range from 15 to 35°. (This would include phases such as Y_2O_3, BaF_2, $BaCuO_2$, Y_2BaCuO_5, CuO, and non-$[0,0,l]$ lines of Y-123.) The expanded pattern in Fig. 32 shows evidence of the three strongest lines of

* YBCO / [0,0,1] through [0,0,10] ■ YSZ / [2,0,0], [2,2,0], [3,1,1], [4,0,0]
+ CeO₂ / [1,1,1], [2,0,0], [4,0,0] ∇ Inconel / [1,1,1], [2,0,0], [2,2,0]
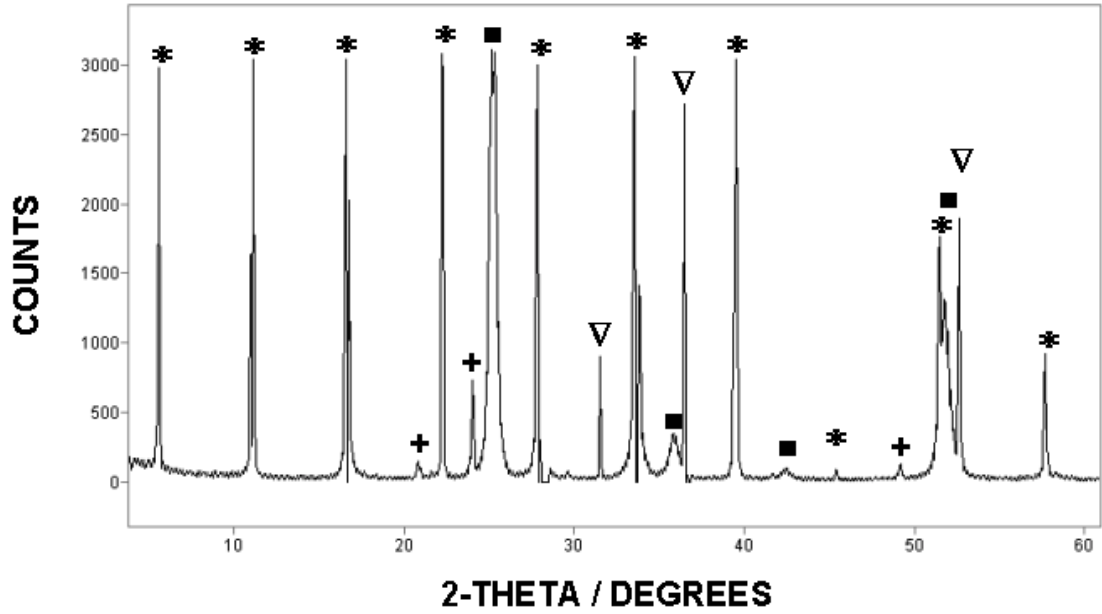
Fig. 30.   Synchrotron   θ-2θ   X-ray   diffraction   pattern   of
Y-123/CeO₂/YSZ/Inconel-coated conductor sample produced from
IBAD-processed substrate and PLD-deposited Y-123.
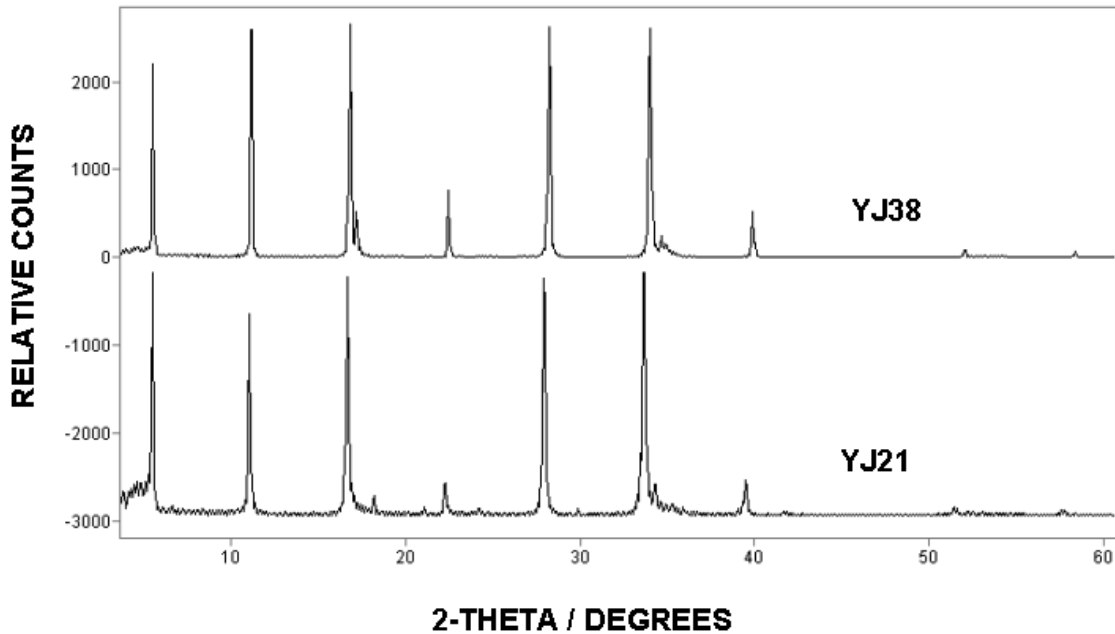
Fig. 31.   Synchrotron X-ray diffraction patterns of two Y-123 films deposited on single-
crystal LAO by the TFA dip-coat method. The five most intense lines (all
[0,0,l]s of Y-123) are saturating the detector.

36
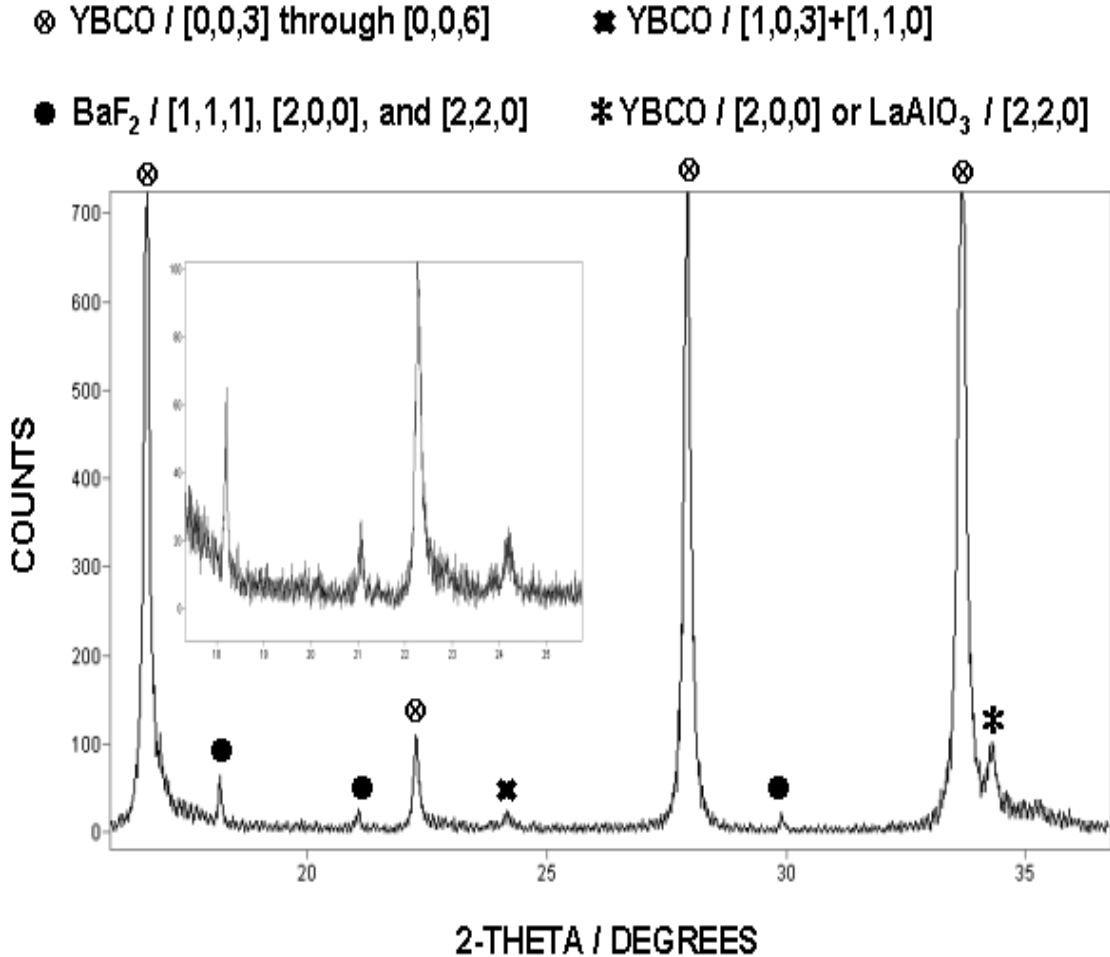
Fig. 32. Expanded view of diffraction pattern for sample YJ21 in Fig. 31, showing evidence of BaF₂, and non-[0,0,l] lines of Y-123.

cubic BaF$_2$ (marked with black dots), the [1,0,3]/[1,1,0] line of Y-123 (**X**), and a line indicated with an ∗ that is believed to be the [2,0,0] reflection of Y-123, although it does occur near the expected 2θ value for [2,2,0] of LAO.

Figure 33 shows the rocking curve for the [2,0,0] diffraction line of a single-crystal YSZ substrate obtained directly from a TFA-type Y-123/CeO$_2$/YSZ coated conductor specimen. The insert displays the corresponding θ-2θ diffraction pattern in the 24-26° 2θ range. In this range, one normally finds the [2,0,0] diffraction lines of YSZ and CeO$_2$ at 25.30° (d = 2.574 Å) and 24.04° (d = 2.706 Å), respectively, for λ = 1.1271 Å. It appears in the insert that the [2,0,0] of the CeO$_2$ layer(s) may be manifested at two somewhat higher 2θ values, indicating a more compressed structure. Specifically, we observe a weak diffraction line at 24.48° and a more intense
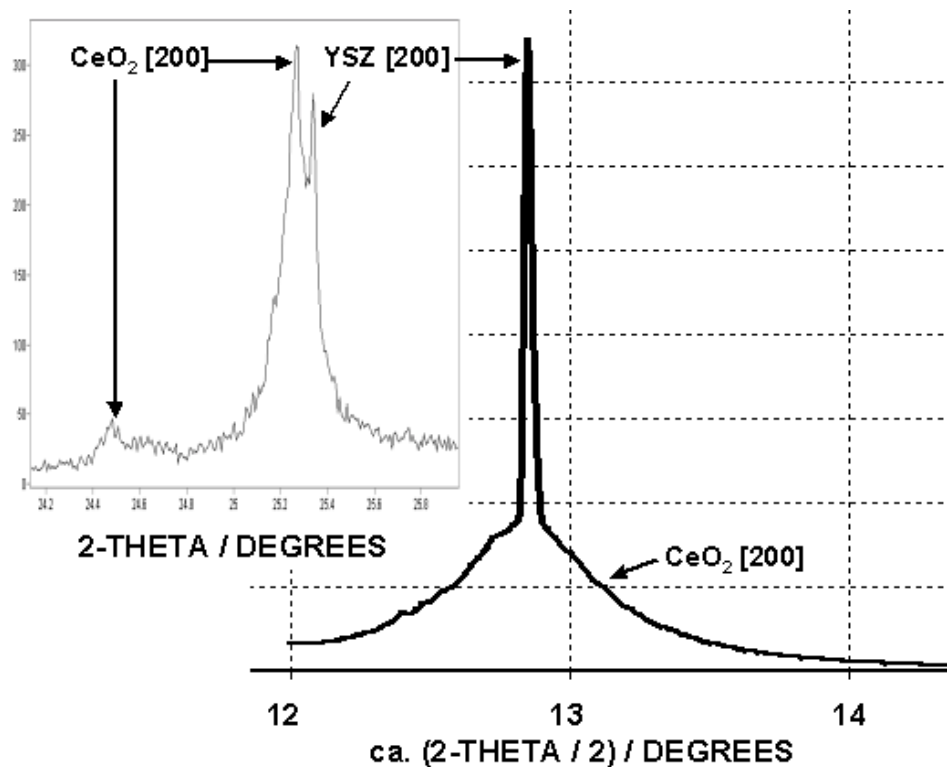
Fig. 33. Rocking curve for the [2,0,0] diffraction line of the YSZ (single-crystal) substrate in a Y-123/CeO$_2$/YSZ-coated-conductor embodiment, showing evidence of what appears to be a compressed CeO$_2$ buffer layer. Inset displays the local θ-2θ diffraction pattern.

one at 25.27°, which together equate to d-spacings of ≈2.64 and ≈2.58 Å, respectively, assuming that these two diffraction lines emanate from the CeO$_2$ buffer layer structure. This interpretation of the diffraction pattern suggests that the CeO$_2$ film may be stratified into two or more layers with different [2,0,0] d-spacings. The sharp/narrow feature in the rocking curve is interpreted to be from the [2,0,0] reflection of YSZ indicated in the inset, where it appears at 25.34°, which gives a d-spacing of 2.570 Å for the YSZ single-crystal substrate (i.e., close to the accepted value of 2.574 Å). The broad underlying feature in the rocking curve is believed to be due to the [2,0,0] line of the ≈30-nm-thick compressed CeO$_2$ buffer layer. It is noteworthy that the diffraction pattern and rocking curve were obtained through a ≈0.5-μm-thick Y-123 over layer. We are continuing to investigate the utility of synchrotron-based X-ray diffraction methods for the quantitative in-situ study of stress/strain and misorientation effects in coated-conductor buffer layers.

Characterization of Coated Conductors by Raman Microscopy

We continue to use Raman microscopy techniques to characterize coated conductors, substrates, precursors, and fully processed samples. The full-symmetry forms of orthorhombic (x = 0) and tetragonal (x = 1) Y-123 exhibit distinct Raman spectra that contain (for each form) five readily detectable phonons. However, it is well known that Y-123 can also exist in several other types of stable and metastable structures and that these structures can coexist (see, for example, M. N. Iliev, Am. Chem. Soc. Symp. Ser. 730 [1999] 107). The Raman spectra of the various forms (and mixtures of forms) of Y-123 are sensitive to the types of structural perturbations that one must be concerned about during the preparation/fabrication of Y-123-based coated conductor materials. These can include (1) poor c-axis texturing, (2) cation disorder, (3) disconnected/fragmented metal-oxygen (M-O) bonds (e.g., due to blotchy/discontiguous deposition), and (4) incomplete oxygenation. The frequency ranges of the five characteristic Raman phonons of orthorhombic and tetragonal Y-123 are summarized in Table 5, together with characteristic frequencies of other frequently observed coexisting phases.

Note especially in Table 5 the two modes for disordered types of Y-123 structures (Y-123-D) typically observed at ≈ 225 and ≈ 585 cm^{-1}. The 225 cm^{-1} mode is reported to be associated with domains of broken M-O chain structures, such as in samples that exhibit clumpy/islandlike deposits. It is known that the 585 cm^{-1} mode is clearly correlated with cation disorder in the Y-123 lattice (see, for example, G. Gibson et al., Physica C 333 [2000] 139). Also, it is important to note that each of the five characteristic phonons of $YBa_2Cu_3O_6$ and $YBa_2Cu_3O_7$ is sensitive to the angle of incidence of the Raman excitation laser with respect to the Y-123 crystallographic axes and the excitation/detection polarization orientations. In Raman microscopy examinations, the direction of the incoming laser radiation and the direction of the detected Raman scattering are typically the same, and that direction is usually perpendicular to the substrate surface; hence, it is also perpendicular to the a-b planes of the Y-123 film (for well-textured samples). Under these excitation/detection conditions (referred to hereinafter as the *xx/yy* orientation), the 340/335 and 140/150 cm^{-1} modes of $YBa_2Cu_3O_6$ and $YBa_2Cu_3O_7$ are considerably more intense than the other three modes. In particular, for perfectly textured Y-123, the 475/505 cm^{-1} mode should be weakest of all. The appearance of this telltale Y-123 mode in *xx/yy* orientation is generally indicative of the presence of poorly textured domains, wherein Y-123 grains are puckered or tilted upward with respect to the substrate surface. In addition, because the frequency of this mode for $YBa_2Cu_3O_{7-x}$ varies monotonically from x = 1 to x = 0, it can be used as an approximate indicator of the oxygen stoichiometry of the Y-123 phase.

Table 5.   *Characteristic Raman frequencies of Y-123 and common coexisting phases*

Phase	Characteristic Phonon Mode Frequencies (cm^{-1})[b]							
$YBa_2Cu_3O_6$	115	140		340	450	475		
$YBa_2Cu_3O_7$	115	150		335	435	505		
Y-123-D[a]		225				585		
$BaCuO_2$						585(m)[b]		635(s)[b]
CuO			290(s)[b]					630(m)[b]
Y_2BaCuO_5				390(m)[b]			605(s)[b]	

[a]Y-123-D indicates normally inactive Y-123 phonons that become active through loss of inversion symmetry or disorder.
[b](m) and (s) indicate moderate relative intensity and strong relative intensity, respectively.

Recent Raman microscopy examinations of Y-123 coated conductor specimens on single-crystal and textured metal substrates have produced spectra that are highly useful in gauging the quality of the Y-123 deposit. These specimens have come from IBAD, ISD, and TFA deposition processes. The spectrum in Fig. 34 was obtained from a TFA-based film deposited on an LAO single crystal and processed at 780°C. In this spectrum, the laser has been defocused over a ≈30-μm-diameter domain. An interpretation of the spectral features is given in Fig. 34. Note that there is evidence of $BaCuO_2$, possible cation disorder (although this is difficult to determine with certainty in the presence of $BaCuO_2$ because of overlapping phonons), a less than optimally textured $YBa_2Cu_3O_{7-x}$ phase with x → 1.0 (as indicated by the intensity of the 475/505 cm^{-1} phonon and its appearance at a value of ≈500 cm^{-1}), and some degree of M-O chain disruption.

TFA-type Y-123 precursors processed at progressively lower temperatures (<780°C) showed less and less $BaCuO_2$, but evidence of cation disorder (585 cm^{-1}) persisted. This is shown clearly in Fig. 35. It is also evident that the
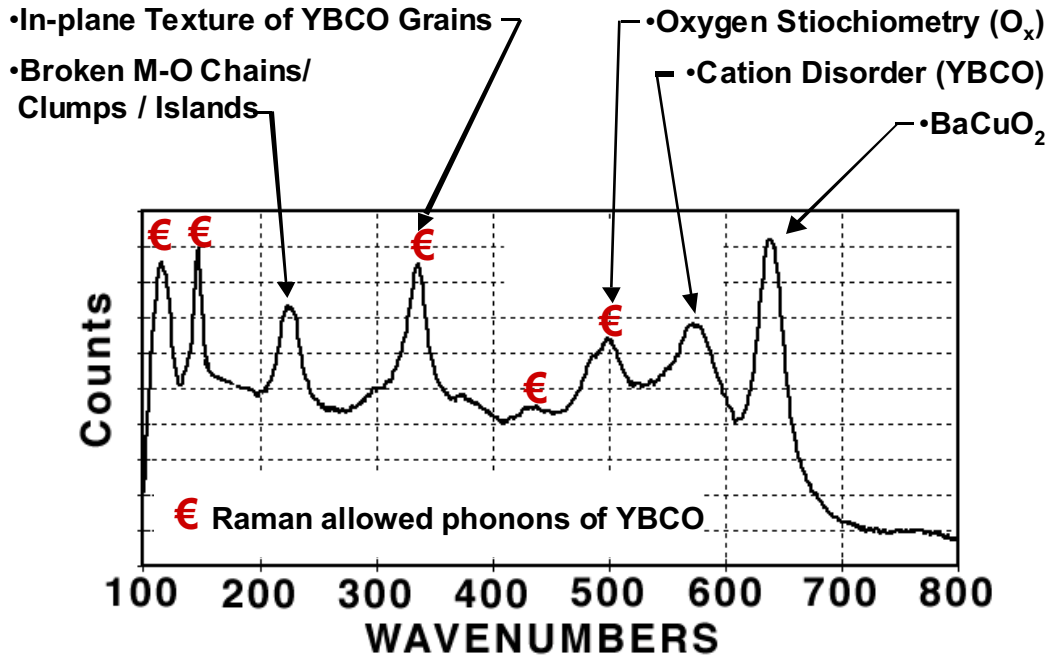
Fig. 34.   *Raman spectrum of Y-123 film on LAO single-crystal substrate, showing many features typically observed for Y-123-coated-conductor specimens.*

samples processed at the two lower temperatures (740 and 720°C) suffered less than the others from the occurrence of broken M-O chain structure domains, but contained increasingly greater amounts of CuO (≈ 290 cm^{-1} mode).

Figure 36 shows Raman microscopy results for an IBAD sample and two ISD samples on textured Inconel substrates. The text blocks to the right of each spectrum in Fig. 36 summarize the interpretation of the results. Comparison of the results in Figs. 35 and 36 reveals that the best samples in terms of Y-123 texture, phase purity, M-O disruption, and cation disorder are those produced by the IBAD process. These are also the coated-conductor samples that have exhibited the highest J_c values in our laboratory. Figure 37 contains Raman microscopy results for two TFA-type samples (on single-crystal YSZ) produced by a collaborating organization. In each case, we present spectra for three locations on the same sample to show the spot-to-spot variability we have regularly encountered with IBAD-, ISD-, and TFA-processed coated-conductor specimens. Referring to the two samples as S1 and S2, respectively, spectra S1-A, S1-B, and S1-C, when viewed in progression, indicate increasing amounts of M-O disruption (225 cm^{-1}), BaCuO$_2$ (≈ 630 cm^{-1}), and loss of Y-123 texture (the disappearance of the 335 cm^{-1} mode). The progression through spectra S2-A, S2-B, and S2-C reveals a similar result. In fact, there is almost no evidence of c-axis textured

41

Raman microscopy spectra of TFA-type YBCO samples on LaAlO$_3$ for four heat treatment (HT) temperatures: Note

- broken M-O chain structures set in above 740°C (1),

- evidence of CuO at the lower HT temperatures (2),

- reduction in in-plane texture for HT temperatures above 760°C (3) vs (4),

- evidence for orthorhombic YBCO (4),

- BaCuO$_2$ begins to appear for HT temperatures above 740°C (5),

- cation disorder persists for all HT temperatures (6),
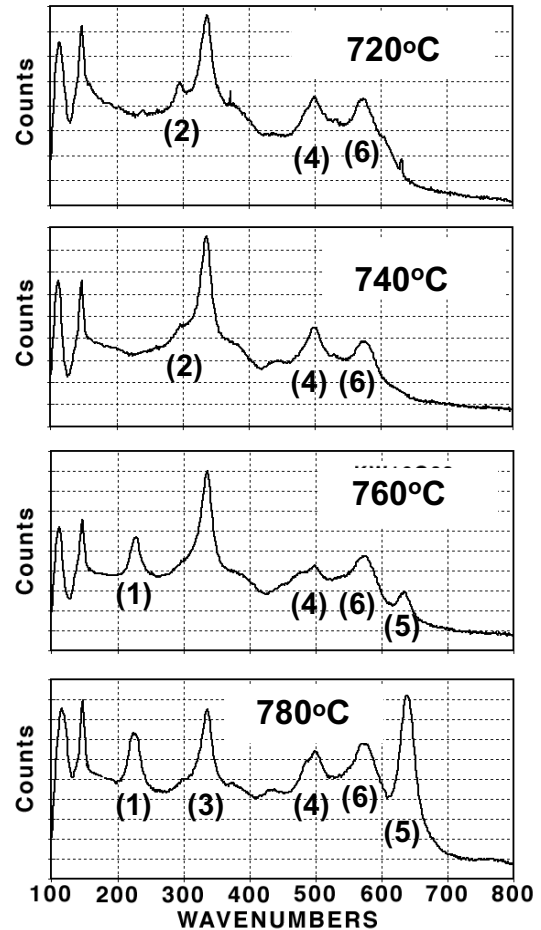
Fig. 35.   Raman microscopy data for series of TFA-based Y-123 films on LAO single-crystal substrates. Text at left of spectra summarizes interpretation.

Y-123 grains in spectrum S2-C. Quite possibly, the BaCuO$_2$ impurity that produced the strong scattering at ≈630 cm^{-1} could be deflecting the Y-123 grains around it out of the plane of the substrate. Raman images of BaCuO$_2$ crystallites embedded in Y-123 films on single-crystal and textured metal substrates show that these crystallites are mostly in the micrometer-size range and occur in patches, but some exhibit in-plane dimensions of several micrometers, which is large enough to disrupt the Y-123 film texture during grain growth.

• YBCO/CeO$_2$/YSZ/Inconel (IBAD) →

  -evidence of a continuous film (1)
  -good in-plane texture (2)/(3)
  -orthorhombic YBCO (3)
  -minimal cation disorder (4)

• YBCO/CeO$_2$/MgO/Inconel (ISD) →

  -broken M-O chain structures (1)
  -poor in-plane texture (2)/(3)
  -orthorhombic YBCO (3)
  -moderate cation disorder (4)

• YBCO/YSZ/MgO/Inconel (ISD) →

  -evidence of continuous film(1)
  -fair in-plane texture (2)/(3)
  -orthorhombic YBCO (3)
  -moderate cation disorder (4)

Fig. 36.   Raman spectra of selected IBAD and ISD coated-conductor samples. Text at left of spectra summarizes interpretation.

2.2 Bi-Pb-Sr-Ca-Cu-O Conductors

2.2.1 Development of Stronger Sheaths for Tapes and Wires

Optimization of Ag-Mg alloys

As we reported in the FY 1999 Annual Report, dispersion-hardened Ag alloys have been examined as sheaths for HTSs. Increased strength over that of pure Ag is needed for strain tolerance and reliable performance in high magnetic fields. These Ag alloys are generally hardened by oxidizing solute species such as Mg or Ni. Oxidation of such alloys is a complex process that consists of several simultaneous events: oxygen diffuses in from the environment; the solutes diffuse toward the oxygen source; the solutes oxidize to form first oxygen-rich clusters and, later, discrete oxide
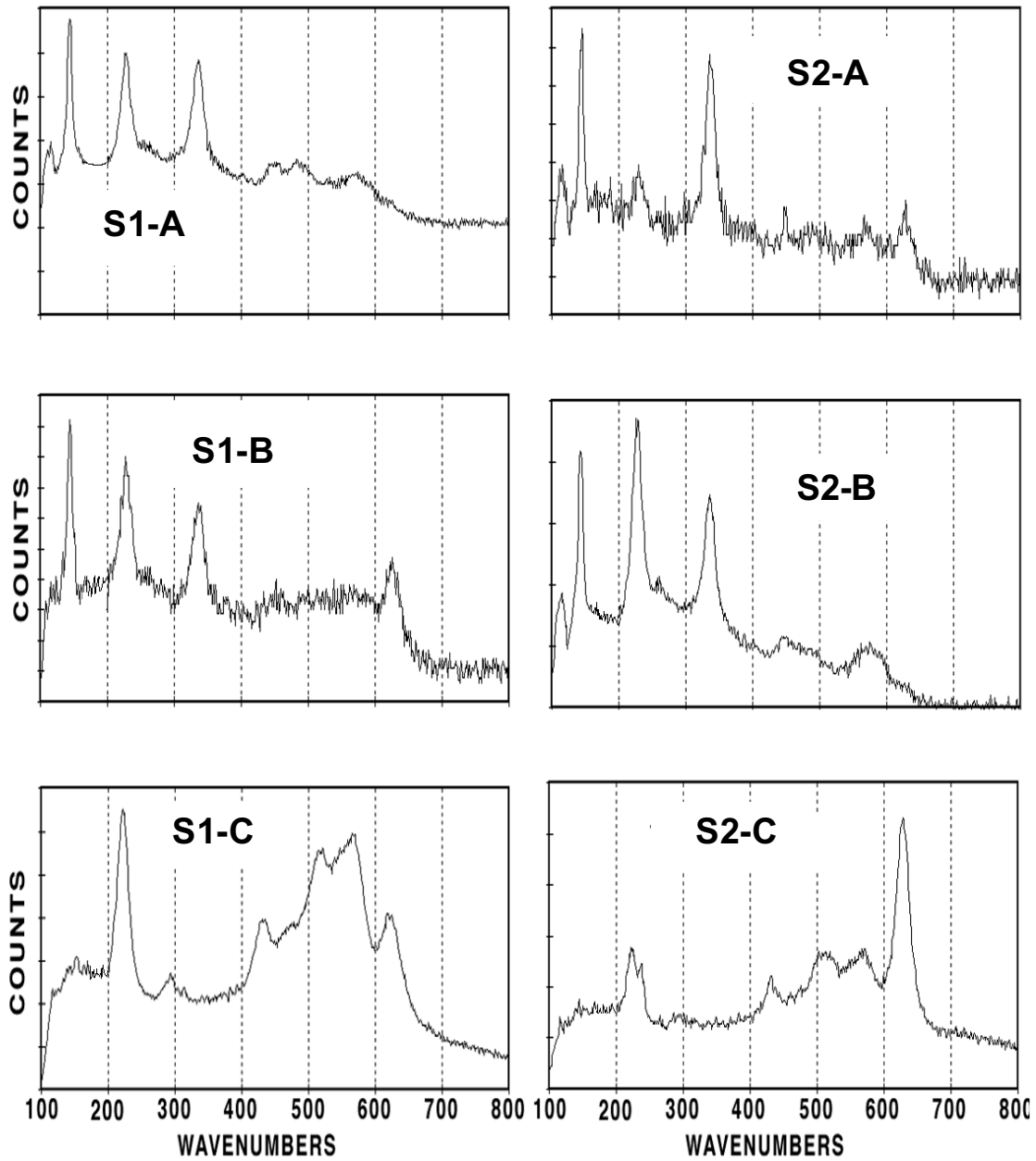
Fig. 37.   Raman spectra of TFA-based Y-123 samples (S1 and S2) at differing locations on same sample, showing spot-to-spot variability.

precipitates; and the grains of the alloy grow, but the growth is impeded once sufficiently large and numerous solute/oxygen particles form. Each of these events affects the resultant mechanical properties of the alloy. Our most recent goal has been to identify optimal heat treatments for hardening Ag/1.2 at.% Mg (AgMg) alloys that may be used as sheaths for Bi-2223 and Bi-2212 superconductors. The extent and distribution of strength within oxidized test specimens has been assessed by microhardness measurements.

In the current studies, square coupons (≤0.5 g and 0.4 mm thick) of 99.9% Ag and AgMg were prepared from cold-rolled sheets and heat treated in flowing 8% O_2 at 450–825°C. Treatment times ranged between 2 and 100 h, depending on the time required for saturation of dissolved oxygen. All samples were given a secondary treatment at 825°C in flowing 8% O_2 for 50 h to simulate actual heat treatments of composite superconductor tapes. Cross-sectional Knoop hardness profiles were obtained from heat-treated coupons and microstructures of polished surfaces were examined SEM.

Figure 38 shows microhardness profiles of cross sections of AgMg alloys treated initially at 450–825°C in flowing 8% O_2. For all samples, changes in hardness were found to be a function of depth. Hardness near the surface was high and decreased toward the center. A treatment temperature of 700°C yielded the profile with the highest overall hardness. The highest hardnesses were approximately three times higher than that of annealed 99.9% Ag (H_k(Ag) = 48 kg/mm^2).

 After a secondary heat treatment at 825°C in flowing 8% O_2 for 50 h, some samples showed marginal increases in hardness, with a few exhibiting a marked increase (Fig. 39). Large increases in hardness occurred in both the 450 and 600°C samples, with the 600°C first heating yielding the highest hardness profile.

Observations of microstructure may explain these mechanical properties. SEM photomicrographs of etched cross sections after the first heat treatment revealed remarkable differences in grain structure among the various heat-treatment temperatures. In AgMg at 450°C, grain size was small and relatively uniform across the sample. At 500°C, a region with significantly larger grains emerged in the centers of the samples. The large-grained region increased in size for the 600, 700, and 825°C samples.

This contrast at the two temperatures is believed to be the result of differences in the rate of grain growth and oxygen transport at the various temperatures. At 450°C, the rate of oxygen transport was slow, but so was the rate of grain growth. Here, oxygen diffused to the center of the sample and formed grain-growth-inhibiting Mg-O clusters before significant grain growth could occur. As temperature increased, so did the rates of both processes. At 500°C and above, significant grain growth occurred in the interior before oxygen could penetrate and form Mg-O clusters.
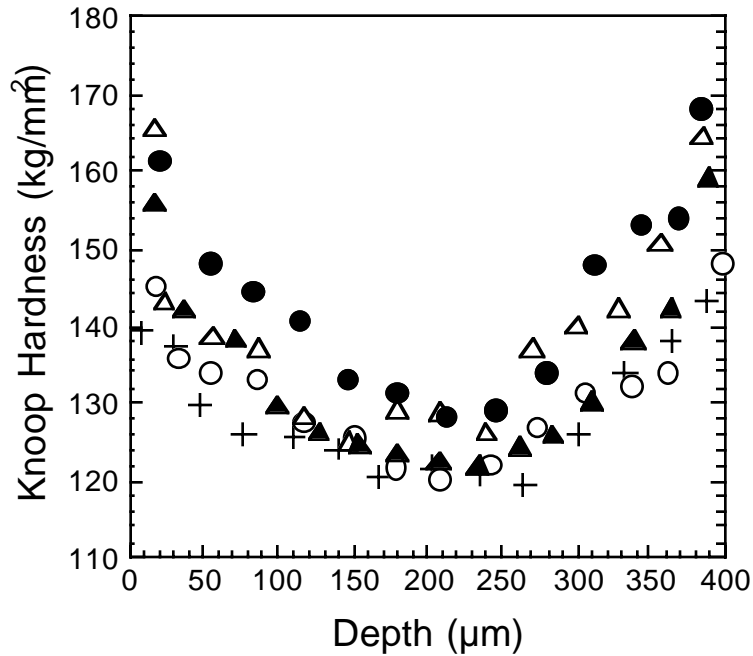
Fig. 38.   Microhardness profiles of AgMg alloys after first heat treatment: 450 (+), 500 (◯), 600 (△), 700 (●), and 825°C (▲).

All samples were given a secondary treatment at 825°C in flowing 8% O_2 for 50 h to simulate the actual treatment of a composite Bi-2223 superconductor tape. The grain structures of both alloys after such treatment did not change (Fig. 40), suggesting that solute-oxygen clusters were present and indeed pinned GBs.

A question may be raised as to whether Mg-O clusters or grain size governs the mechanical properties of internally oxidized AgMg alloys. Clustering certainly plays a role in determining grain size, but the extent to which clusters impede dislocation motion has not been established. Superimposing the grain-size distributions on microhardness profiles allows us to examine the relationship. Figure 41 is a hardness profile for the 700°C sample of the AgMg alloy, including hardness data from both heat treatments, superimposed on grain-size distribution. After the first treatment, the transition from the small- to the large-grained region appears to show an accompanying decrease in hardness with increasing grain size, in accordance with the Hall-Petch relationship

$$\sigma \propto D^{1/2}, \tag{1}$$

where σ is the strength (or hardness) and D is the average grain size.
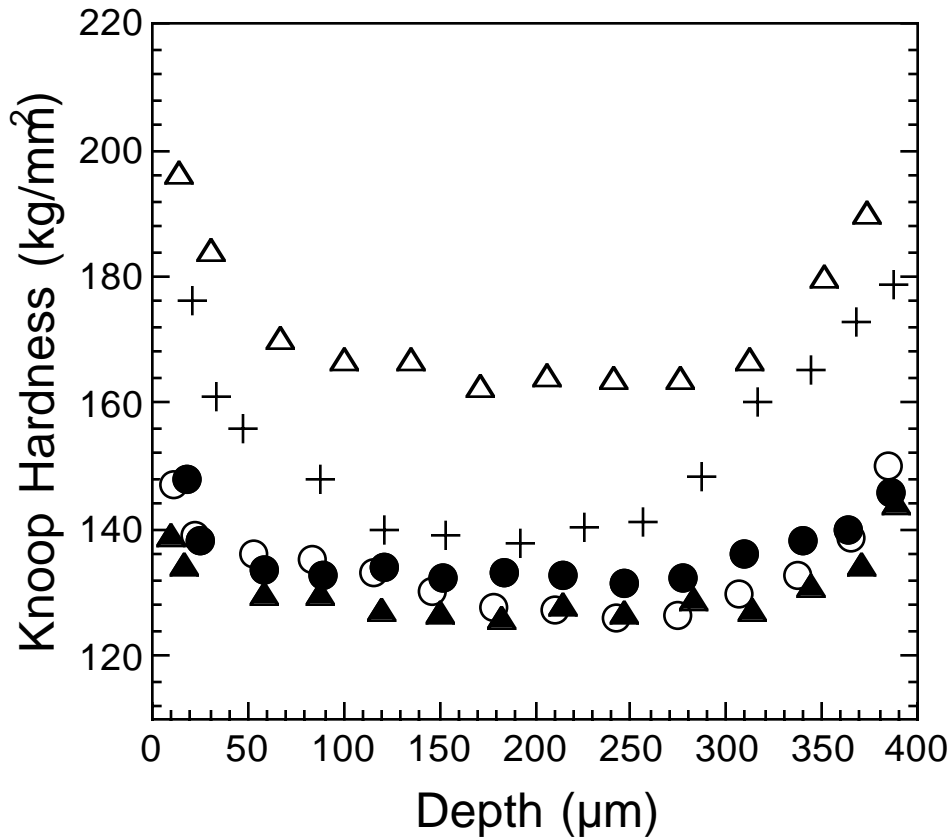
Fig. 39.   Microhardness profiles of AgMg alloys after secondary 825°C heat treatment: 450 (+), 500 (◐), 600 (Δ), 700 (●), and 825°C (▲).

However, the decreases in hardness are not as abrupt as the changes in grain size, which suggests that the distribution of solute-oxygen clusters also plays a role in hardening of the alloy. After the second heat treatment, the hardness profile flattens out, yielding an approximately constant hardness in the large-grained region and slightly increased hardness in the small-grained region at the surface. In this case, hardness remains nearly uniform across the boundary between grain sizes, suggesting that clustering becomes more influential than grain size in determining hardness.

Internal oxidation of Ag alloys that contain Mg was found to be complicated and highly dependent on processing temperature. The presence of Mg-O clusters significantly affected hardness and microstructure, and hardened the alloy by impeding dislocation motion. The hardness of the oxidized AgMg was significantly   higher   than   that   of   Ag.   The   alloys   generally
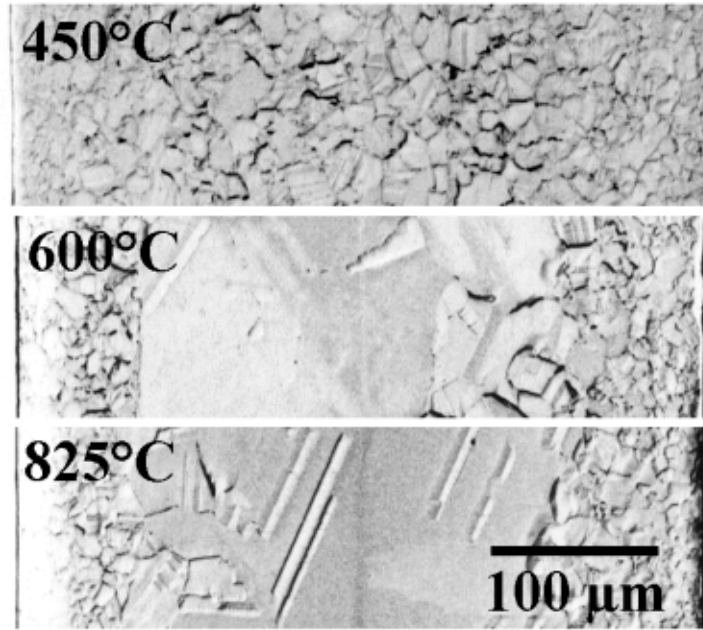
Fig. 40.   SEM photomicrographs of etched alloys after initial heat treatment at temperatures shown, followed by secondary treatment at 825°C.

exhibited profiles with high hardness values near the surface and lower hardness values toward the center. Hardness was higher in the small-grained regions and decreased in the larger grained regions, in accordance with the Hall-Petch relationship. However, the transition in hardness was not as abrupt as the change in grain size, suggesting the effect of another factor on hardness.

Irrespective of the precise explanation for hardening effects in oxidized AgMg, it was necessary to complete two additional pieces of work. The processing schedule for, especially, Bi-2223 required optimization, and microstructures required detailed study. We therefore developed a processing schedule that imparts a uniform yield strength of 200 MPa to Ag/1.2 at.% Mg, while maintaining high J_c in the Bi-2223.

The key to the hardening process is formation of oxygen-rich Mg-O clusters within the Ag. The superstoichiometry of O with respect to Mg in these clusters decreases as they become larger. A schematic diagram of the smallest Mg-O cluster is shown in Fig. 42. Actual clusters within a specimen that was heated in 8% O_2 for 50 h are shown in Fig. 43.

The Mg-O clusters are stable with prolonged heating at temperatures to 825°C. Although larger clusters have a tendency to form preferentially along
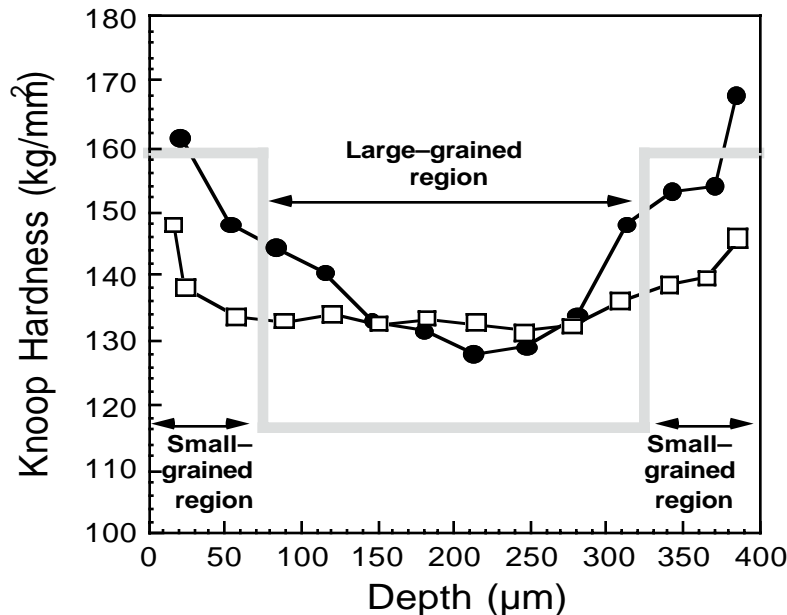
Fig. 41.   Relationship of grain size regions to hardness profile for AgMg alloy treated in 8% O$_2$ at 700°C for first treatment (●) and 825°C for second treatment (□).

grain boundaries (Fig. 44), most of the smaller clusters remain within the grains; thus, the increases in yield strength over that of pure Ag are substantial.

Round Bi-2212 Wires with Hardened Sheaths

In support of cable and transformer projects, we are developing Bi-2212 wires with round cross sections.   Recent work has focused on the use of hardened sheaths that contain Al. The need for sheaths that are stronger than pure Ag is agreed upon. Similar to use of Mg/MgO for hardening Ag, the Al/Al$_2$O$_3$ system exhibits good compatibility with the superconductor core.

Heat treatment parameters were initially optimized for a 300-filament Ag/Al-alloy-sheathed wire (outer diameter 0.8 mm). The key parameter that required control was the peak temperature for partial melting. Various heat treatment schedules were examined.   Critical currents of the samples were generally measured at 77 K.   Figure 45 shows the dependence of peak
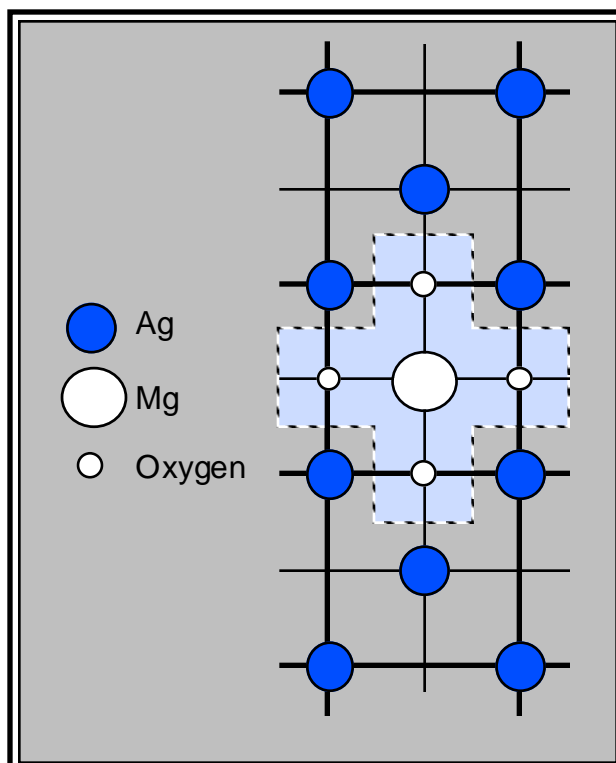
Fig. 42. *Two-dimensional representation of Mg-O cluster in Ag lattice; O/Mg = 4.*
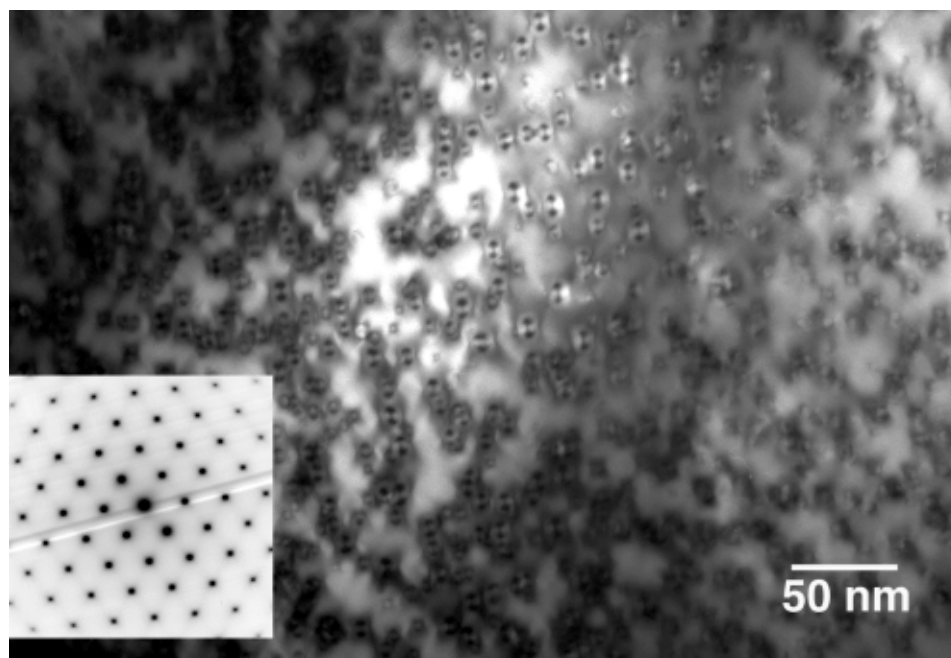
Fig. 43. *TEM photomicrograph of Mg-O clusters in alloy heated at 850°C for 50 h.*
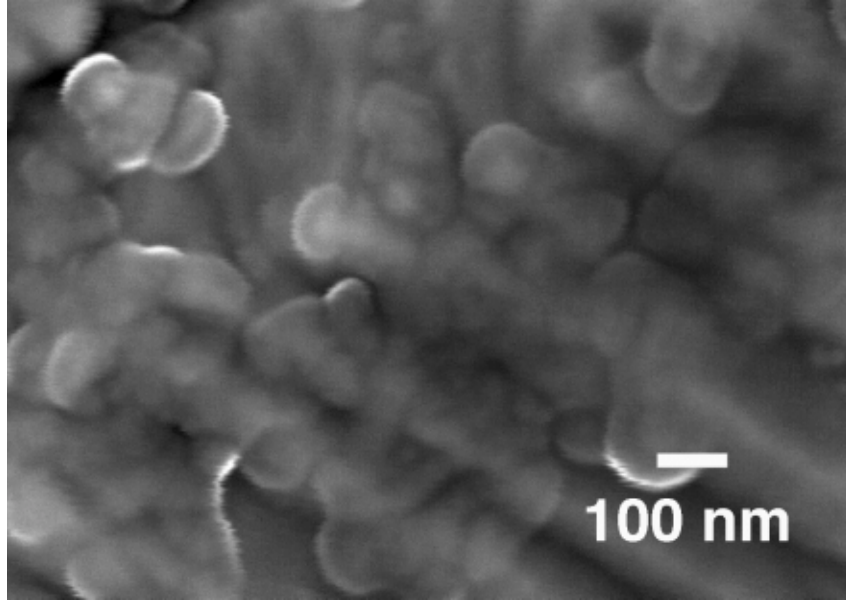
Fig. 44.   SEM photomicrograph of large Mg-O clusters near grain boundary in alloy heated at 850°C for 50 h.

temperature on the I_c of the conductors, which were postannealed at 450°C in Ar. It has been shown that this annealing increases the I_c of the samples at 77 K, but reduces the I_c of the samples at 4.2 K. In this study, the highest I_c was obtained with heating at 891°C. This finding indicates that significant melting is necessary to achieve high J_c. The best result to date was $I_c = 2.5$ A at 77 K. Based on the I_c value at 77 K, the J_c at 4 K was estimated to be $>3 \times 10^5$ A/cm^2.

Single-filament Ag-sheathed Bi-2212 wire (outer diameter 0.8 mm) has also been fabricated and heat treated. The highest I_c at 77 K was 0.96 A. Both conventional and isothermal heat treatments have been tested.

To work efficiently, we have adopted a strategy for optimizing the wire processing. Although it is time consuming and relatively expensive to measure the I_c of every sample at 4.2 K, it is quite easy to do so at 77 K. Measurements at 77 K are best made on samples with high T_c values. Annealing in Ar is useful for raising T_c, and thus for facilitating good I_c measurements at 77 K; however, this annealing reduces I_c at 4.2 K. Therefore, we use Ar annealing for samples to be measured at 77 K, but do not plan to anneal samples to be used or measured at lower temperatures. We have found that for our sheathed Bi-2212 wires, the relationship between partial-melting temperature and I_c at 77 K is very similar to what has been published about this relationship at 4.2 K. Therefore, our decision to use primarily 77 K measurements seems to be reasonable.
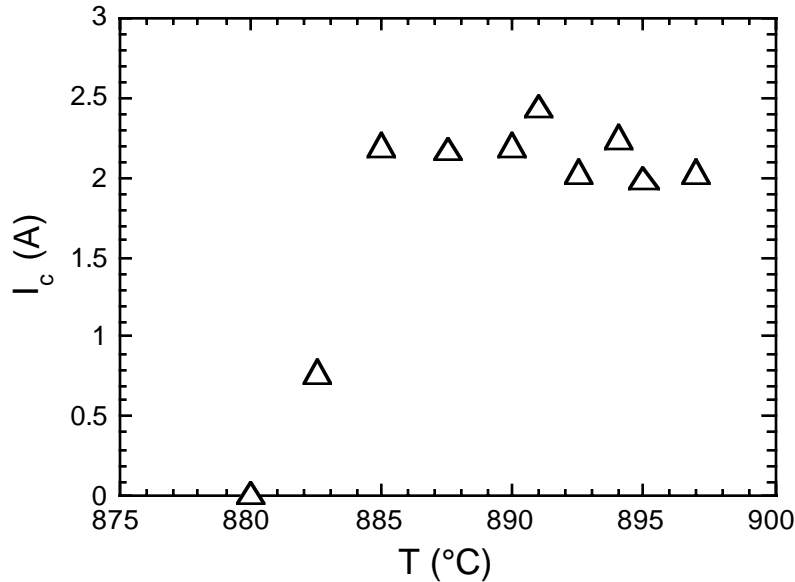
Fig. 45. *I_c at 77 K versus maximum partial-melting temperature for a 300-filament Ag/Al-alloy-sheathed wire conductor.*

A further study was conducted of the cooling rate after the melting stage, with the peak temperature fixed at 891°C. The cooling rates were varied from 3°C/h to 15°C/h. A cooling rate of ≈ 7°C/h yielded the highest I_c at 77 K.

I_c measurements of some wires were conducted at 4.2 K in applied magnetic fields (Fig. 46). For these Bi-2212 wires, there was no postannealing in Ar. The sample in Fig. 46 exhibited an I_c of 0.51 A at 77 K and 200 A at 4.2 K in self field. At 4.2 K and 6 T, the sample maintained 36% of its zero-field I_c. Transport J_c at 4.2 K was 1.7 x 10^5 A/cm^2. The highest J_c we can expect from our best wires is estimated to be ≈220 kA/cm^2.

To reduce AC losses of the Bi-2212 wires, insulating layers are being applied to reduce the coupling loss. $SrZrO_3$, $BaZrO_3$, and ZrO_2 have been used as the insulating materials. In one method, the insulating materials were packed into the Ag-alloy tube, along with Bi-2212 filaments. In another method, the insulating materials were dip-coated before mechanical working. The latter method ensured that the individual filaments were isolated from each other. The conductor was preheat-treated to burn out the organics before drawing.
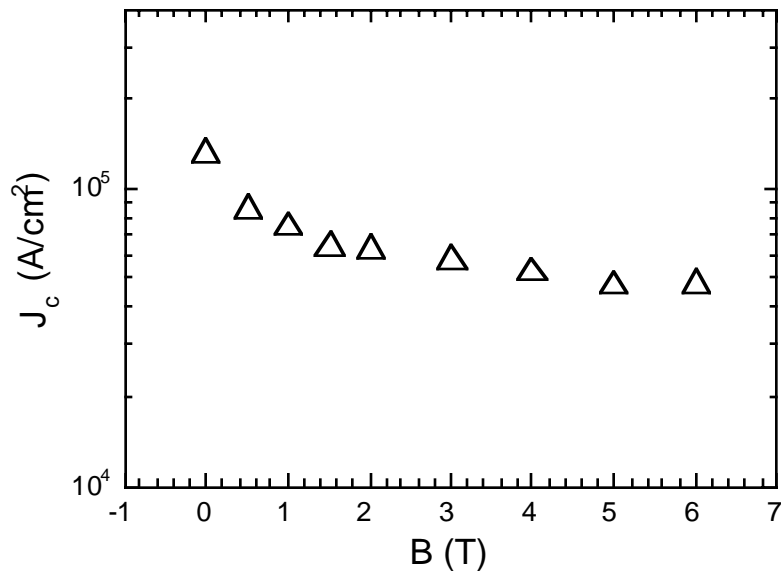
Fig. 46. J_c *at 4.2 K versus applied magnetic field for round multifilament Bi-2212 wire.*

The insulating layers obtained were found to be uniform and dense according to SEM observations, and have been shown to be chemically stable at high temperatures. Several coatings that have been developed appear to be suitable for practical applications.

2.2.2 Optimal Microstructural Development in Bi-2223 Superconductors

Transport current in Bi-2223 and Bi-2212 continues to be limited at 77 K by factors such as misaligned superconducting grains, presence of deleterious phases, and poor flux pinning. In this section, the efforts to identify and eliminate second phases, provide optimal development of textured superconducting grains, and improve performance in an applied magnetic field (H_{app}) are summarized.

Raman Spectroscopy of Bi-2223 Microstructures

Raman microspectroscopy and imaging techniques are being used to investigate key mechanistic features that influence the formation of layered Bi-based superconducting phases during the thermal treatment employed to produce Ag-sheathed Bi-2223 composite conductors. Recent information gained from these studies includes identification of the constituent phases in certain

53

nonsuperconducting second-phase (NSP) agglomerations that tend to resist dissipation as high-T_c phase formation proceeds to completion.

The experimental methods and instrumentation used in these investigations were reported previously (see, e.g., K. T. Wu et al., J. Mater. Res. 12 [1997] 1195). Briefly, heat-treated Ag-sheathed Bi-2223 specimens were cast in epoxy and the casting was polished until the ceramic core of the specimen was exposed. Raman microscopy was used to examine the exposed polished cores, which were usually mounted in transverse view.

Figure 47 is an example of the type of measurement that we typically make when using Raman microscopy techniques. The defocused Raman spectrum in Fig. 47 was obtained by spreading the excitation laser over the circled region indicated in the white-light image (WLI) of the specimen (in this case, a transversely mounted, fully processed, 19-filament Ag/Bi-2223 composite) and recording a dispersive (grating mode) Raman spectrum. The Ag-sheath regions in the WLI shown in Fig. 47 have been darkened by image processing to provide contrast with the ceramic filaments. Portions of three ceramic filaments can be seen in the WLI.

From previous phase characterization studies, we know that the Raman features at 626, 570, and 520 cm^{-1} in defocused spectra are due to Bi-2223, $(Ca,Sr)_{14}Cu_{24}O_{41}$ (14/24 AEC), and $(Ca,Sr)_2CuO_3$ (2/1 AEC), respectively. Using the imaging Raman microscope in the filter mode, we determined the location within the circled area in the WLI from which the Raman scattering occurred at each of the three frequencies. These regions are shown by the three Raman images to the right of the WLI in Fig. 47. (Each of the three Raman images has been corrected to remove background [BG] effects.) In these three images, the white regions represent the locations of the phases scattering at the frequency indicated below each image.

The image of the 626 cm^{-1} feature I(626)/BG revealed that the layered Bi-2223 phase was located in bands along the Ag sheath. Images for the 570 and 520 cm^{-1} features revealed that the 14/24 and other nonsuperconducting phases tended to agglomerate and overlap in the midcore region of the filament. The appearance of overlapping phase domains was associated with the penetration depth of the excitation laser. NSP agglomeration appeared to be a key factor limiting the supercurrent capacity of the Ag/Bi-2223 composite conductor. Current Ag/Bi-2223 heat treatment studies (in collaboration with American Superconductor Corp. (ASC)) are focused on developing thermodynamics-based strategies for dissipating these agglomerates in multifilament wires.
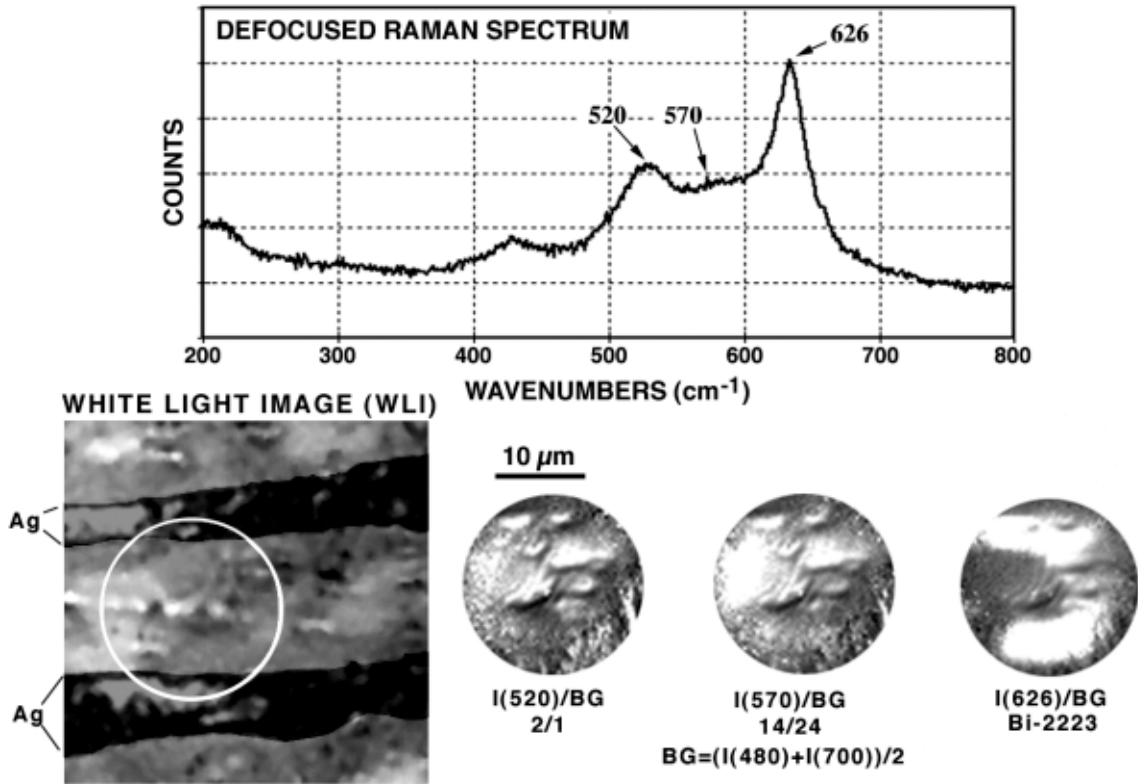
Fig. 47. Raman microscopy results for 19-filament Ag/Bi-2223 composite wire. White domains in Raman images I(520)/BG, I(570)/BG, and I(620)/BG indicate locations of the 2/1, 14/24, and Bi-2223, respectively, in WLI.

Merged filaments constitute a second type of performance-limiting microstructural defect in multifilament Ag/Bi-2223 composite wires. Typically, when two filaments merge (Fig. 48), the resultant domain is characterized by poorly developed Bi-2223 grain colonies and large agglomerations of nonsuperconducting phases. The defocused Raman spectrum in Fig. 48, obtained from the shaded region in WLI, shows evidence of 2/1 (its principal Raman band being indicated as image a in the defocused spectrum) and Bi-2223 (its principal Raman band being indicated as image b in the defocused spectrum). The white domains in the Raman images of images a and b, shown in Fig. 47, indicate the dominant locations of 2/1 and Bi-2223, respectively.

To obtain a clearer picture of the relative presence or absence of overlapping phases in Raman images of agglomerated regions, we have developed an image-processing procedure based on gray-scale inversion and subtraction. Inverting the gray scales for images a and b and then subtracting a^{-1} from b^{-1} produces an image in which white regions should highlight the general location of Bi-2223 and black regions should highlight the general location of 2/1. The result of this procedure is shown in Fig. 6. The whitest

regions in the (a^{-1}–b^{-1}) image were where Bi-2223 was the more prominent phase; the darkest regions occurred where 2/1 was more prominent. SEM plus energy-dispersive spectroscopy (EDS) analyses of the regions shown in Fig. 48 yielded metallic element compositions that were in good agreement with the implications of the Raman imaging results. The type of phase congestion observed in the merge region under study in Fig. 48 was typical of almost all of the merge zones we have examined in the course of this investigation.

(a)   (b)   (c)
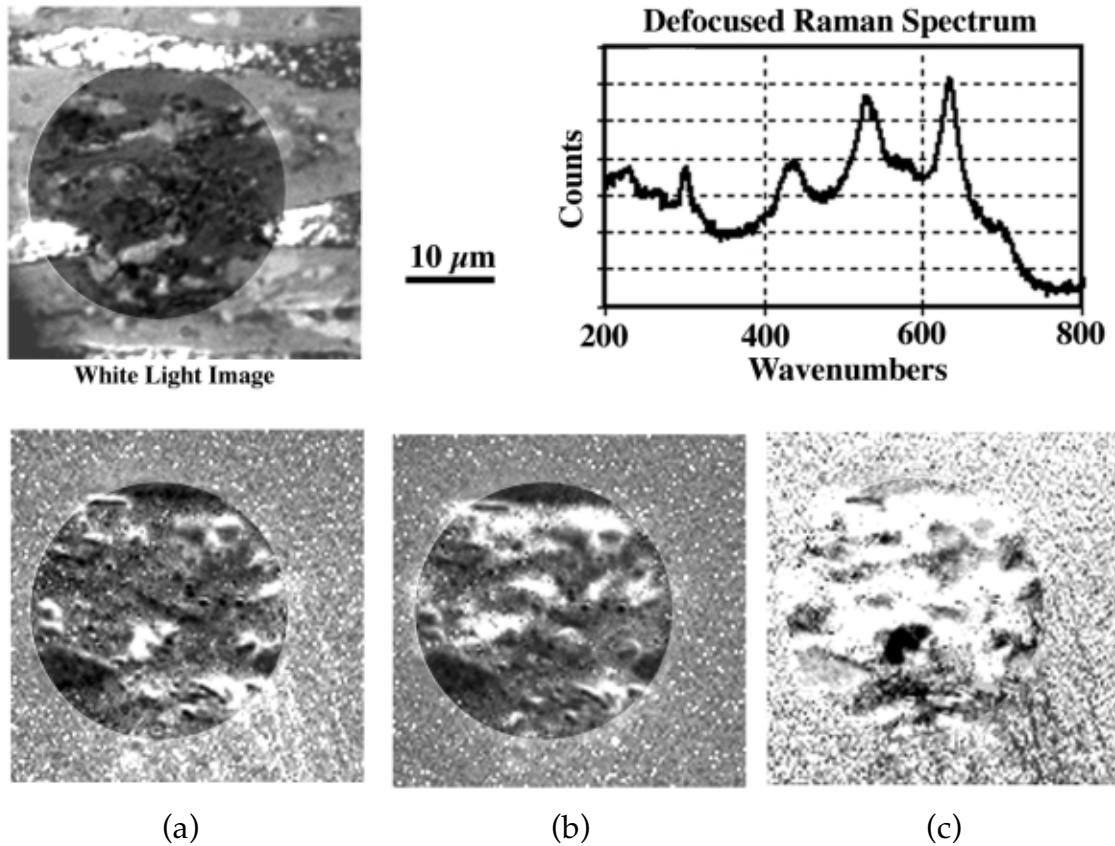
Fig. 48.   *Raman microscopy analysis of large merge zone between two filaments in 19-filament Ag/Bi-2223 composite wire. Images a and b in defocused Raman spectrum (circled region) are due to 2/1 and Bi-2223, respectively. White areas in Raman images for (a) image a and (b) image b show dominant locations of 2/1 and Bi-2223 phases, respectively; (c) inverted/subtracted image (a^{-1}–b^{-1}) provides a map of general location of 2/1 (darkest regions) and Bi-2223 (lightest regions).*

Minimization of Deleterious Nonsuperconducting Phases

The discussion in the previous section of this report makes clear the need to greatly reduce or eliminate large congested NSPs in multifilament Ag/Bi-2223

composite conductors. Over the past year, we have investigated a heat treatment protocol that either eliminates the NSPs or reduces them to the smallest possible size (preferably submicrometer). Based on the work of Holesinger et al. (presented at 1999 Annual Peer review) on the rubblizing effect that large NSPs have on Bi-2223 grain colonies during intermediate deformation, it seems particularly advantageous for this diminishment of the nonsuperconducting phases to take place during the first heat treatment (HT1), i.e., before intermediate deformation.

In the course of extensive studies of how temperature and oxygen partial pressure (pO_2) influence microstructural development during the heat treatment of Ag/Bi-2223 composites, we observed that for a given pO_2 in the range in which the Bi-2223 phase has appreciable stability (nominally 0.04-0.21 atm), there is an onset temperature for the growth of robust Bi-2223 grain colonies (a desirable effect) and another onset temperature for the persistent formation of large NSPs (an undesirable effect). This effect is illustrated in Fig. 49, wherein we refer to these two temperatures as the grain-growth takeoff temperature (GGTT) and the second-phase takeoff temperature (SPTT), respectively. Ideally, we want the GGTT to be well below the SPTT, but this is not generally the case. At the lowest pO_2 (0.04 atm), the SPTT is lower than the GGTT, and at 0.075 atm O_2, SPTT $\cong$ GGTT. However, at the higher pO_2s, the SPTT is slightly higher than the GGTT. From a processing point of view, we want to be on the SPTT curve, provided it lies at a temperature lower than the GGTT curve.

The other important observation that we have made in the course of this work is that the composition of the nonsuperconducting phases varies significantly with pO_2 and temperature, from a CuO-dominated mix at low pO_2, to a $(Ca,Sr)_2CuO_3$-dominated mix at intermediate pO_2, to a $(Ca,Sr)_{14}Cu_{24}O_{41}$-dominated mix at the highest pO_2. This observation implies that it is possible to manipulate the constituent species of the NSP mix within the range of pO_2s in which the Bi-2223 phase has appreciable stability. One could do this by sliding along the GGTT curve between 0.075 and 0.21 atm O_2 and/or along the SPTT curve between 0.04 and 0.075 atm O_2. Accordingly, we have carried out HT1s on multifilament-type Ag/Bi-2223 composite specimens using several combinations of pO_2 and temperature on the GGTT/SPTT lower bound in Fig. 49. A typical sliding heat treatment of this type (hereinafter call thermal slide heat treatment [TSHT] generally consists of the following sequence of steps:
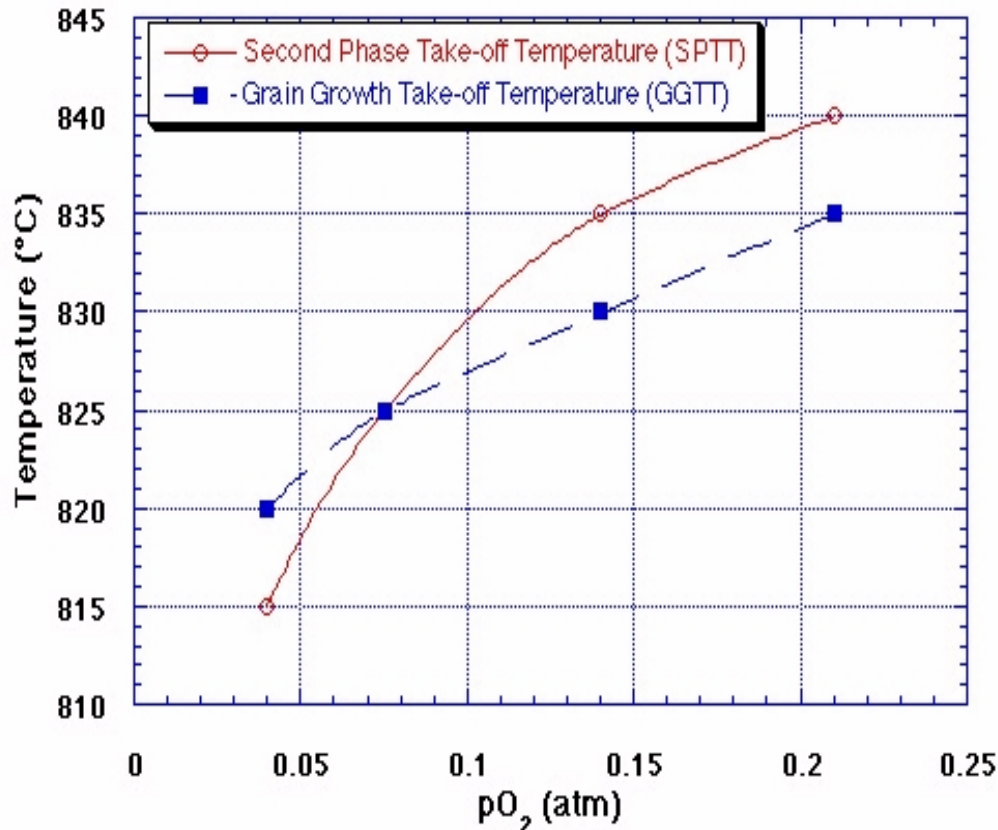
Fig. 49.   Second-phase and grain-growth takeoff temperatures for Ag/Bi-2223 composites as a function of pO₂.

1. Ramping the temperature up to 825°C at 10°C/min in 0.075 atm O_2, and holding at 825°C for several hundred to 1000 min,

2. Raising the temperature and pO_2 to 835°C and 0.21 atm O_2, respectively, and holding at those conditions for several hundred to 1000 min,

3. Shifting the temperature and pO_2 to another point on the GGTT/SPTT lower bound (e.g., 815°C and 0.04 atm O_2) and holding for several hundred to 1000 min,

4. Repeating combinations of the above heat treatments, then terminating the TSHT process by furnace-cooling the sample.

The TSHT methodology includes the condition that the variations must be made without ever crossing the lower (in terms of temperature) bound of the GGTT curve or the SPTT curve. This is done (depending on the direction one is moving along the GGTT/SPTT lower bound) by either lowering temperature first and then lowering pO_2, or raising pO_2 first then raising temperature. Termination of the treatment with a furnace cool (versus a rapid quench) is more

appropriate for application to Ag/Bi-2223 wire manufacturing, because a rapid quench induces crack-causing stresses in the wire sample.

Development work on the TSHT process is being done in collaboration with ASC as part of the effort of the ASC-led Wire Development Group. The types of microstructures achieved in some of the better TSHT processing sequences we studied are shown in Figs. 50 and 51, which contain SEM images of transverse sections of 19-filament Ag/Bi-2223 composites after the TSHT procedure. Only a few second phases larger than 1 μm are noticeable in most of the 19 filaments in Fig. 50. The phase purity and sparse nonsuperconducting phase content exhibited in Fig. 50 are considerably better than the norm for Ag/Bi-2223 composites. Figure 51 shows a high-magnification SEM image of another "better case" TSTH specimen. The sequence currently in use to produce "better case" HT1 specimens consists of 300 min at 825°C/0.075 atm O_2, then 1000 min at 835°C/0.21 atm O_2, then 1500 min at 825°C/0.075 atm O_2. X-ray diffraction examination of this HT1-type specimen indicated that the Bi-2223 to Bi-2212 ratio was ≈6.

Figure 52 presents the results of a computer-assisted SEM image analysis carried out for the sample that produced the image in Fig. 51. Figure 52a shows a grayscale histogram for a representative region of ceramic phase in the composite after manually erasing the silver by using a standard image-processing package. We know from previous studies that the 1–86 grayscale range corresponds to Bi-2223/Bi-2212, the 87–114 range corresponds to narrow transition regions between Bi-2223/Bi-2212 and the two AEC nonsuper-conducting phases (2/1 and 14/24), the 115–156 range corresponds mainly to 14/24 AEC, and the 157+ range corresponds mainly to 2/1 AEC. Figure 52b shows the area fraction of each of the four ranges, and indicates that the total Bi-2223/Bi-2212 fraction is ≈90%.

In addition to achieving a lower area fraction of nonsuperconducting phases relative to conventional HT1 results, we also achieved microstructures with considerably fewer large NSPs. In collaboration with ASC, we have shown that some of our more effective TSHT treatments, when substituted for ASC's standard HT1, lead to conductors with performance levels at least as good as ASC's best production wires manufactured to date. It is our hope that a fully optimized TSHT treatment coupled with a mating finishing treatment (yet to be developed for TSHTs) will yield an Ag/Bi-2223 conductor with performance properties that are 50-100% better than ASC's current production wires.
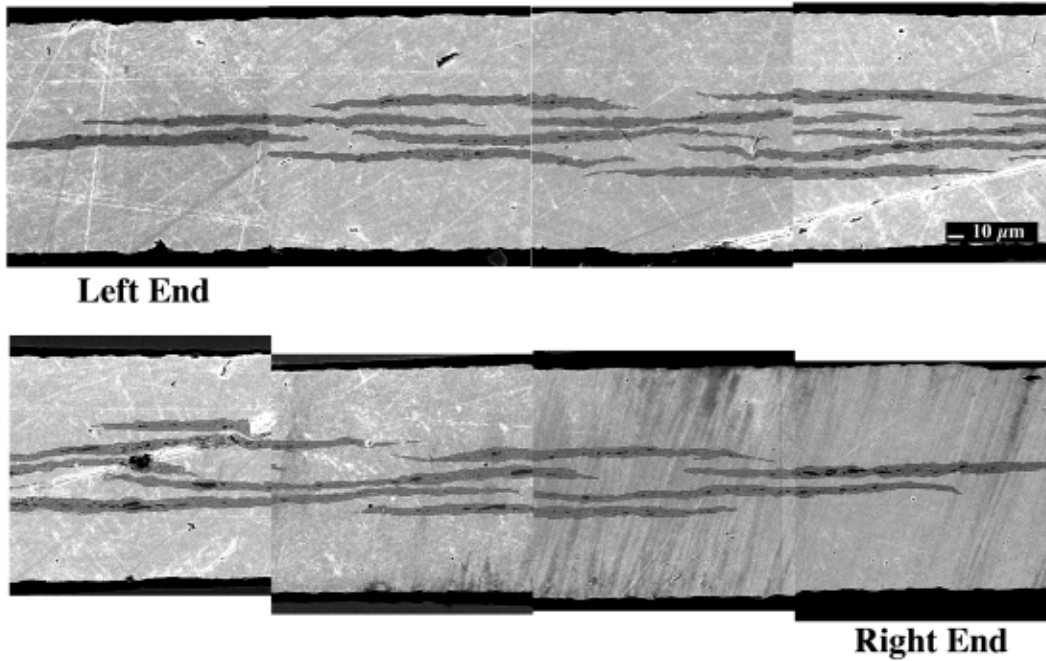
Fig. 50. *Transverse section of Bi-2223 composite specimen subjected to optimized TSHT.*
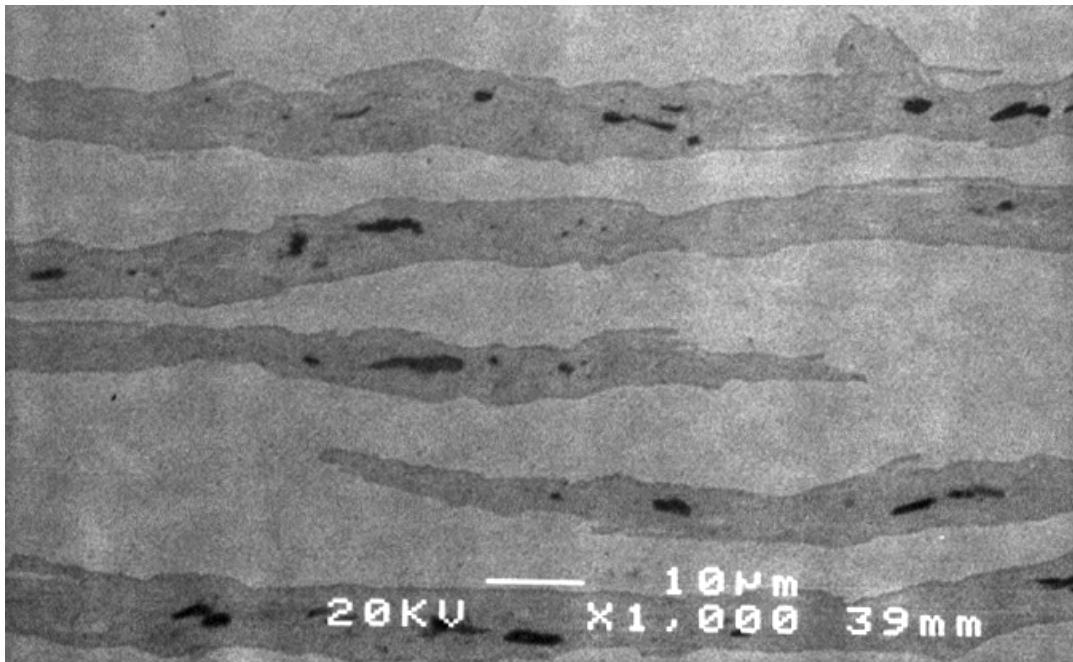

Fig. 51. *High-magnification SEM image of representative segment of "better case" TSHT sample.*
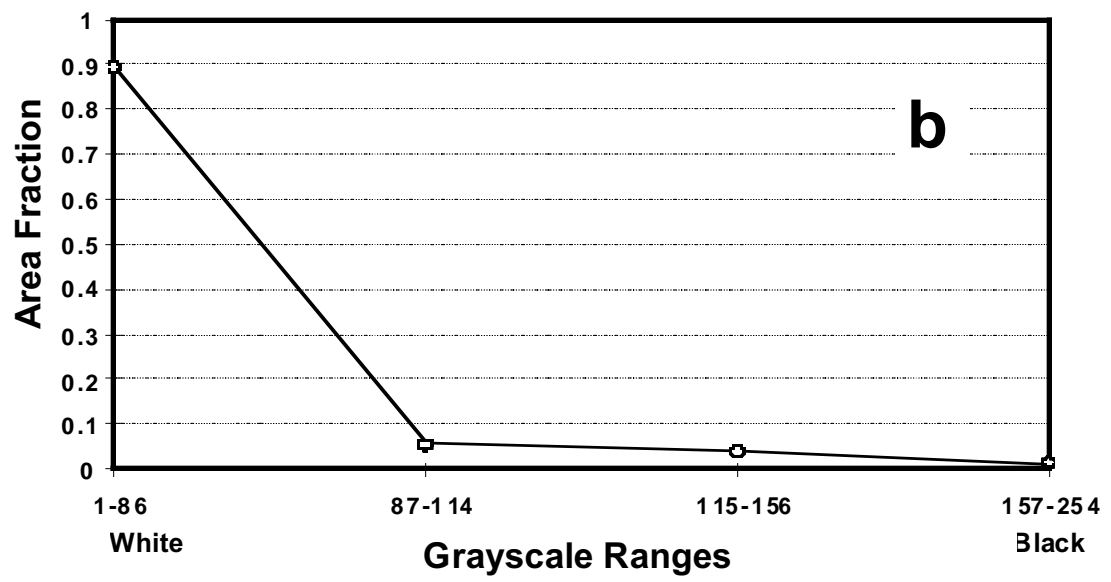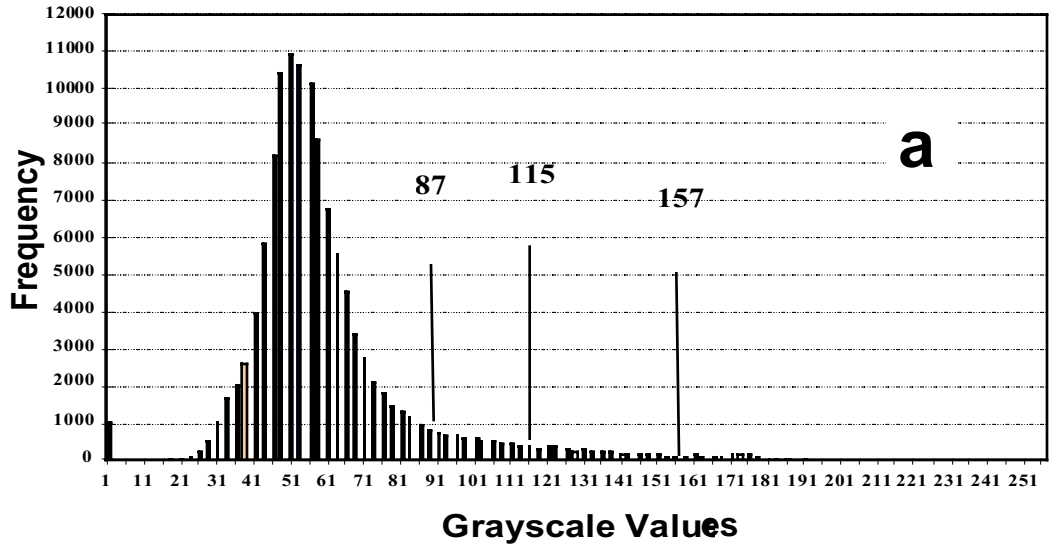
Fig. 52. (a) Grayscale values from SEM image in Fig. 51 and (b) area fractions for four gray scale regions indicated in (a); four ranges (from left to right) correspond, respectively, to regions dominated by Bi-2223, Bi-2223/NSP transition zones, 14/24 AEC, and 2/1 AEC.

Our next efforts to complete optimization of the TSHT process are aimed at determining (1) the optimal amount of time to spend at each temperature/pO_2 set point, (2) the most effective sequence of said set points, (3) the required number of visits to each set point, and (4) the optimal allowable Bi-2223 phase percentage at the end of a TSHT-type HT1. The last of these issues influences the final heat treatment that is carried out to heal the microstructural damage caused by the intermediate deformation after HT1.

Bi-2223 Tapes with Improved In-Field Performance

First-generation Bi-2223 superconducting tapes have been used to build large prototype devices such as magnets, transformers, power cables, fault current limiters, and SMES units. State-of-the-art first-generation tapes are multifilamentary, made with Ag or Ag-alloy sheaths. They are typically ≈3.5 mm wide and ≈250 μm thick, >100 m long, and capable of withstanding 100 MPa tensile stress without degradation of J_c values. They exhibit a critical current I_c of ≈50 A at 77 K in self-field.

A long-standing goal is to improve pinning in Bi-2223 tapes. We have attempted to improve pinning by creating defects at the interface between Bi-2223 and MgO. This technique has yielded promising results that will be discussed.

The precursor powder was produced by the chemical precipitation method and contained Pb-added Bi-2212, Ca_2PbO_4, alkaline earth cuprates, and CuO. Precursor powder particles were consolidated into billets by a dry-bag pressing method. The prepressed billets were inserted into Ag tubes, swaged, drawn through a series of dies, and then rolled to a final thickness of either ≈450 or ≈250 μm. Tape samples were cut and heat treated at 828°C in an 8% O_2 atmosphere. The total annealing time was ≈60 h. Each heat treatment step was 30 h at the set point. A slow-cooling schedule incorporated three cooling steps: 2°C/h for 8 h, 10°C/h for 10 h, and 60°C/h to room temperature. Cold pressing at a load of 50-70 tons was applied after the first heat treatment.

To make tapes with improved pinning, Ag was removed from one side of the as-rolled tape by chemical etching. The exposed side of the Bi-2223 was placed on an MgO single crystal and heat-treated, along with a reference tape under the same conditions. Following the first heat treatment, Bi-2223 adhered to the MgO single crystal. The composite Bi-2223/MgO tape was cold-pressed under the same load as the reference tape, and put through another heat treatment.

Bi-2223/MgO sample tapes were also fabricated on MgO films that were produced by electron-beam (e-beam) physical vapor deposition. The MgO was deposited to a thickness of ≈ 2.5 μm onto a Bi-2223 surface at a temperature of 750°C. Samples were then heat-treated under the same conditions as the Bi-2223 reference tape and the Bi-2223/MgO single crystal.

Microstructures were characterized by SEM, TEM, and chemical analysis by EDS. Transport and inductive J_c values were obtained at 4.2 and 77 K.

TEM revealed that the contact between the Ag and Bi-2223 grains was excellent. X-ray diffraction indicated that the c-axis of Bi-2223 was perpendicular to the interface.

Transport critical current was measured on short samples of Bi-2223/Ag tapes at 77 K. The I_c measurements at 77 K in self-field after each heat-treatment step were 30–35 A after the first heat treatment, and 90–100 A after the second heat treatment. Figure 53 shows the I_c-H_{app} characteristics of the superconducting tape that carried 120 A in zero applied magnetic field at 77 K ($J_c \approx 3 \times 10^4$ A/cm^2). Magnetic fields up to 0.4 T were applied perpendicular and parallel to the tape width. Magnetic field dependence at 77 K showed pronounced anisotropy for fields parallel and perpendicular to the tape width. A perpendicular field of 0.4 T lowers the I_c value from 120 to 5 A. A parallel field showed weak dependence: magnetic field of 0.4 T reduces the I_c value from 120 to 35 A.

To characterize high-I_c tapes for high field applications at 4.2 K, a short sample (4 cm) that carried 120 A at 77 K was tested at 4.2 K in a field applied perpendicular to the width of the tape. An I_c value of 560 A was obtained in the self-field at 4.2 K ($J_c \approx 1.4 \times 10^5$ A/cm^2). After an initial drop to 310 A at 1 T, the I_c reaches a plateau and then declines to 245 A at 6 T. The observed I_c drop in the low-field region at 4.2 K indicates that connectivity and grain alignment of Bi-2223 grains could be further improved by a factor of ≈ 2.

A monofilament Bi-2223 reference sample was made by the technique described above, heat-treated twice and pressed, and then measured for transport I_c at 77 K. Voltage versus transport current characteristics for a thin Bi-2223 reference tape at 77 K with a magnetic field applied perpendicular to the width of the tape showed a sharp decrease. I_c decreased from ≈ 50 A at zero field ($J_c \approx 2 \times 10^4$ A/cm^2) to ≈ 2 A at 0.4 T. This result clearly illustrates the weak performance of the Bi-2223 tapes at 77 K in applied magnetic field perpendicular to the width of the tape.

To improve pinning in Bi-2223 tapes, defects were introduced at the interface of the sample. Ag was removed from one side of the tape, and the exposed surface of the Bi-2223 was placed on an MgO single crystal. After the first heat treatment, good contact was developed along the interface between the Bi-2223 and the MgO single crystal. Transport critical current values for Bi-2223/MgO composite tapes were twice those for the Bi-2223 reference tape at 77 K in zero field. The tapes were cold-pressed and heat-treated again. High-magnification TEM was used to reveal, at higher resolution, the nature of defects in Bi-2223 grains at the interface with MgO (Fig. 54). Defects that were perpendicular to the direction of the current in Bi-2223 grains were observed.

After etching the Ag, cold-pressing the Bi-2223 with the MgO, and during heat treatment, there is a chance of damaging the sample and causing the superconductivity to decrease. The thin Bi-2223/MgO sample showed a T_c of 109 K. It is apparent that the etching, pressing, and heat treatment have not decreased the T_c of the Bi-2223/MgO sample.

Figure 55 shows the normalized values for transport current in applied magnetic field for the thin Bi-2223 reference sample versus the Bi-2223/MgO sample. In a magnetic field of 0.4 T applied perpendicular to the width of the tape, transport critical current was about three times higher in the
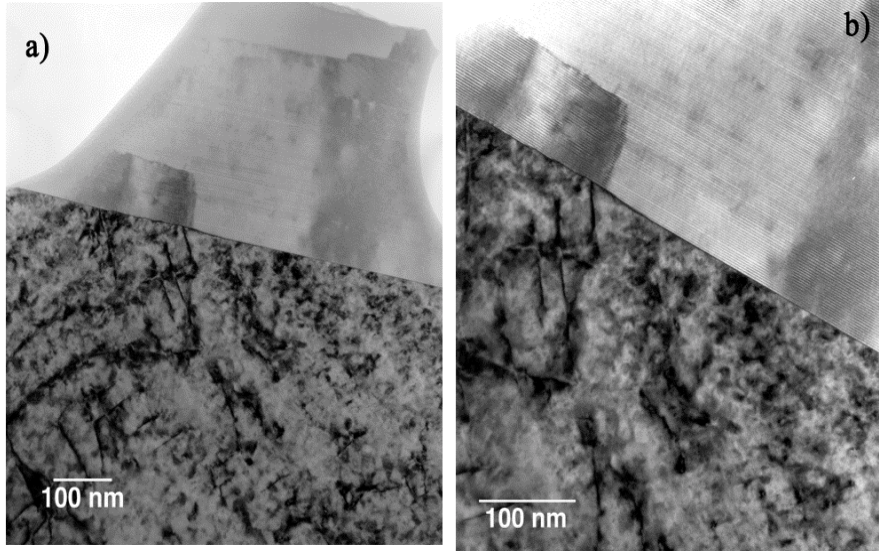
Fig. 54. *High-magnification TEM photomicrographs showing interface between Bi-2223 and MgO single crystal after cold-pressing and second heat treatment: (a) ≈120,000x; (b) ≈200,000x.*
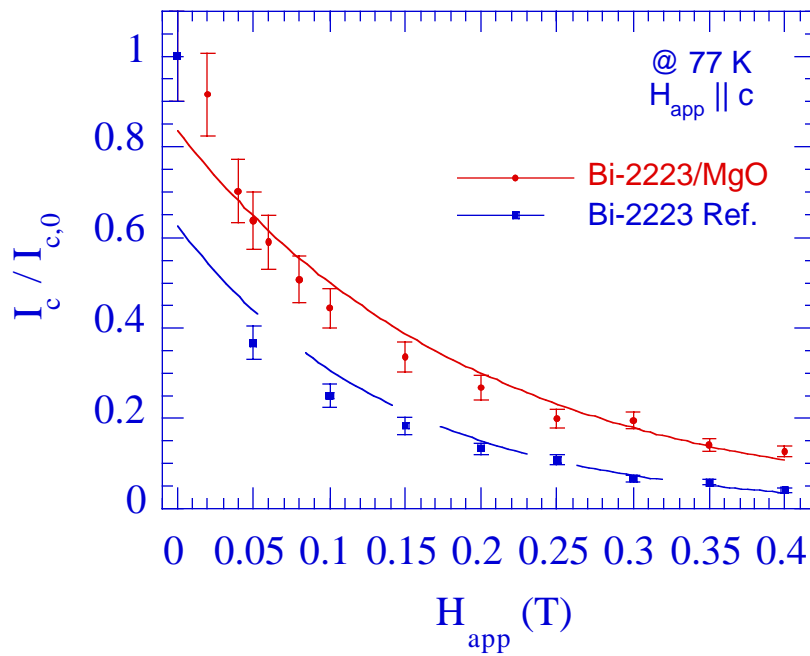
Fig. 55. *Normalized transport current as function of applied magnetic field for thin Bi-2223 reference tape and Bi-2223/MgO tape at 77 K.*

Bi-2223/MgO single crystal than in the Bi-2223 reference tape. The I_c value in a field of 0.4 T decreased to $\approx$12% of the I_c value in the zero field for the Bi-2223/MgO sample, whereas the Bi-2223 reference sample decreased to $\approx$4%.

Samples of e-beam MgO were processed under the same conditions as the Bi-2223 reference tape and the Bi-2223/MgO single-crystal tape. (E-beam evaporation has potential industrial use; single crystals of MgO do not.) T_c was $\approx$102 K and inductive $I_{c,drive}$ was $\approx$150 mA for the Bi-2223/e-beam MgO sample (J_c $\approx 2 \times 10^4$ A/cm^2). However, the transport current measurements did not show improved pinning in these samples. The method will be examined further.

2.3 Applications and Devices

Successful design of devices requires that we understand the relationships between structure and properties and among properties. Magnetic properties are of particular interest to applications such as flywheels. We report here on the status of our flywheel program and on our investigation of the forces between magnet fields and HTSs. We also report on a magnetic current sensor that has emerged from our studies of transport in HTSs.

2.3.1 Development of Flywheel Energy System

The main purpose of this effort is to support the Boeing Phantom Works in their (SPI) project to develop a 10-kWh flywheel energy system based on HTS bearings. The first unit to be developed will contain a 3-kW motor/generator (M/G). The second unit to be developed will contain a 100-kW M/G. This effort started in FY1999. Specific objectives for FY2000 were to (1) provide general consultation on overall design of the system and components, based on ANL's previous experience with these types of devices; (2) assist in the analysis and design of the HTS bearing; (3) explore alternative M/G topologies for the 100-kW system; and (4) participate, as the occasion permits, to accelerate the successful completion of the SPI project.

Significant progress was made in all four FY2000 objectives. (1) ANL participated in a consulting capacity on all aspects of the system and component design. (2) A push/pull near-zero-stiffness lift bearing was chosen to provide most of the levitation force, with the HTS bearing used mostly to provide stability. A new type of welded HTS fabrication was investigated for use in the HTS bearings. (3) A cup-motor design with rotating back iron was chosen as a likely candidate for the 100-kW M/G; the electromechanical stiffness of this motor was analyzed, and a small working 3-kW prototype was fabricated and tested. (4) Several instances occurred in which ANL was able to identify information or provide small hardware components to enhance the SPI project.

Key results from the FY 2000 program follow.

• A near-zero-stiffness lift bearing was specified for the 10-kWh flywheel. This bearing provides nearly all of the levitation force, freeing the HTS bearing somewhat to supply mostly stability. Such a design minimizes the required amount of HTS bearing material. A key feature of this bearing allows accommodation of tolerances that are typical of manufacturing, with adjustments after fabrication, as needed.

• Examination of a new superconducting welding technique for bulk HTSs showed that this type of fabrication has potential for use in future HTS bearings. The ability to weld large monoliths of bulk YBCO, in which the critical current density between grains is nearly the same as that within grains, will provide bearings with larger levitational pressures and lower rotational drag at high speeds. The welding technique was developed under separate funding. Our participation was to help measure levitational forces and trapped fields, confirming the quality of the superconducting joint.

• A cup-motor design was chosen for investigation as a possible topology for the 100-kW M/G. One difficulty with low-stiffness HTS bearings is that many motor topologies are destabilizing. It is a challenge to identify M/Gs with high specific power and low negative electromechanical stiffness. The rotating part of the cup motor consists of a permanent magnet cylinder that is uniformly magnetized in the direction of a single diameter. It is surrounded by an air gap, which in turn is surrounded by a rotating back iron. The stator coil sits in the air gap. Advantages of this concept are that there are no destabilizing forces associated with the rotating permanent magnet and that there is no rotational drag when the stator coils are not carrying current. Preliminary analysis indicates that such a M/G could be capable of 100 kW of power without destabilizing the HTS bearing. A small prototype 3-kW M/G was fabricated, a special controller was developed, and the M/G was preliminarily tested. Tests of the M/G were promising.

• A previously delivered ANL electromagnetic clutch was used to test the Boeing HTS bearing, thus helping to accelerate the project schedule.

ANL will continue its general consultation on the SPI project. It should be noted that this consultation effort is, in essence, a comprehensive technology transfer of all of ANL's general knowledge in the area of HTS bearings and flywheel energy storage accumulated over the last ten years. This knowledge is expected to augment the existing knowledge of the Boeing SPI team. The cup-motor M/G concept will be further analyzed for scale-up to 100-kW; the 3-kW M/G will be tested in FY 2001. The results of the 3-kW M/G tests will contribute to the design decision on the M/G topology for the 100-kW unit. Specific future

tasks include helping to understand rotational losses, optimizing the temperature at which the HTSs operate (64–77 K), exploring concepts for damping a structural resonance that may occur below the expected operating range, and continuing to explore the use of welded HTS structures in the bearing design. ANL will also offer its spin-pit test facility for use in a rotor destruction test of the 10-kWh flywheel system, which is planned for the last phase of the SPI project.

2.3.2 Transients in Superconductor Tube Subjected to Magnetic Fields

Bulk HTSs in the form of hollow cylinders or rings have two potential practical applications. The first is magnetic shielding and the second is in fault-current limiters (FCLs) for the power industry. A typical FCL consists mainly of an iron core inside a superconductor tube and a copper coil wound on the outside of the superconductor tube. When an FCL is used under normal operating conditions, the shielding capability of the superconductor tube keeps the impedance low. Under fault conditions, the large current in the copper coil exceeds the shielding capability of the superconductor tube and there is a jump in impedance because the iron core is no longer shielded from the coil by the superconductor tube.

In principle, the superconductor tube can provide shielding whether the source of the applied magnetic field is outside or inside the tube. We describe the induced-current and transient characteristics of a melt-processed Bi-2212 superconductor tube at 77 K. Tests were conducted with copper coils placed either outside (externally applied field) or inside (internally applied field) the tube to study the differences in transient characteristics of these two configurations. The pulsed current supply and the test setup are identical to those that we reported previously (Fig. 56). In the first test section, a copper coil is wound externally on the cylindrical superconductor tube. The coil has 80 turns, is ≈145 mm long, and has an inside diameter almost identical to the outside diameter of the superconductor tube. The Bi-2212 tube was 190 mm long, with a wall thickness of 8.0 mm and an outside diameter of 70 mm. A Hall probe was placed at the center of the tube to measure the axial magnetic flux density B. To measure the leakage field, a second Hall probe was placed on the outside of the copper coil, at the same elevation as the Hall probe inside the tube. A Rogowski coil was used to measure the induced current in the superconductor tube. Response times of both the Hall probe

68
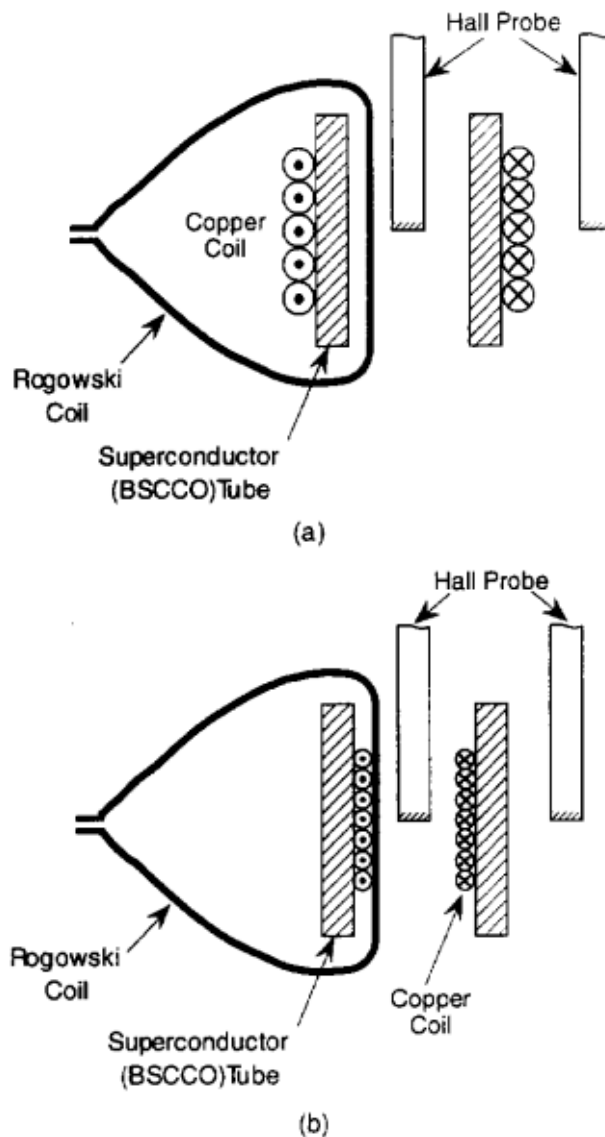
Fig. 56. *Schematic diagrams of test section used to determine induced-current and transient characteristics of melt-processed Bi-2212 superconductor tube: (a) coil outside superconductor tube, and (b) coil inside superconductor tube.*

and the Rogowski coil were much shorter than the transient time of the present experiments. The second test section is similar to the first, except that the copper coil is placed inside the superconductor tube.

Figure 57 shows the measured current and field at relatively low excitation current. In this figure, N is the number of turns of the driving coil; I (shunt) is the excitation current in the copper coil, measured by the shunt
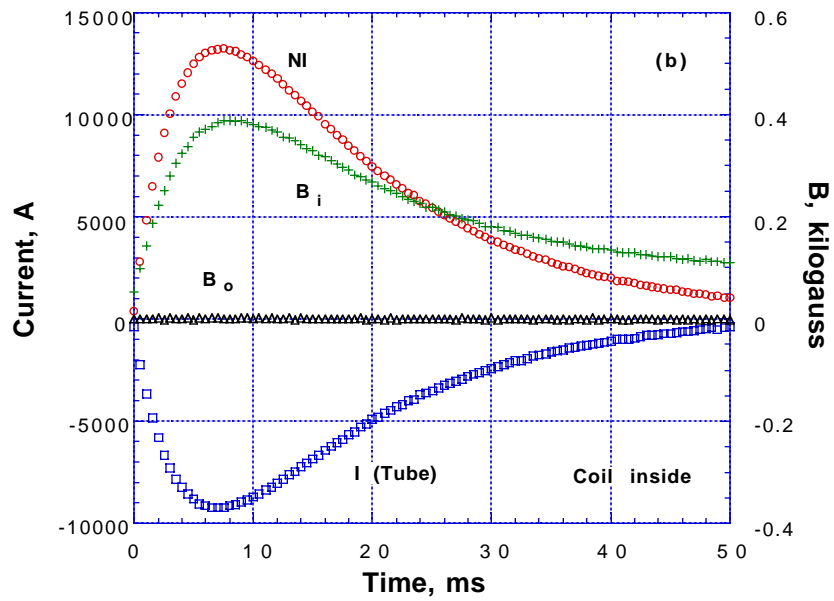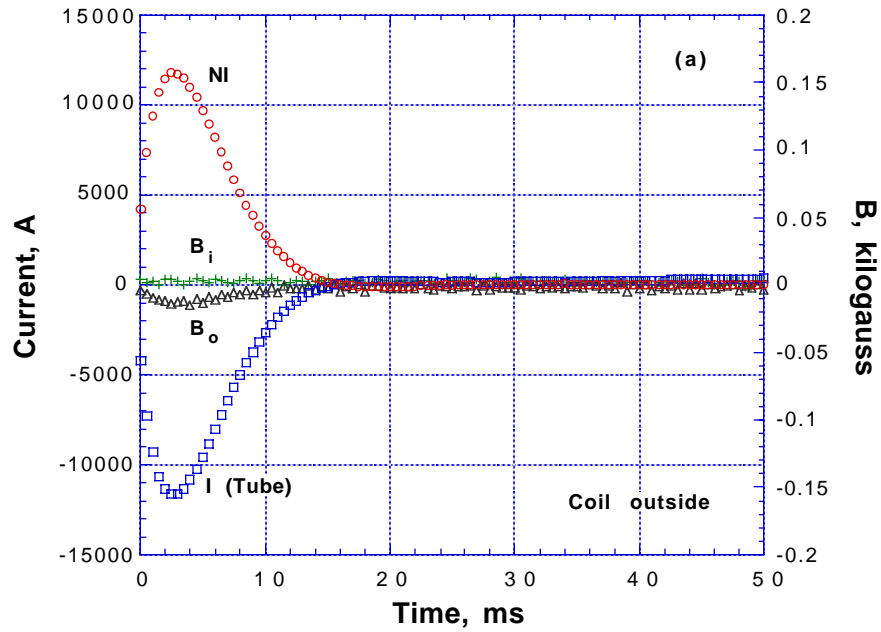
Fig. 57.   Measured current and field at relatively low excitation current for (a) coil outside superconductor tube, and (b) coil inside superconductor tube.

resistor; I (tube) is the induced current in the superconductor tube, derived from the signal of the Rogowski coil; B_i is the magnetic flux density, measured by the Hall probe inside the Bi-2212 tube; and B_O is the magnetic flux density, measured by the Hall probe on the outside of the superconductor tube.

Figure 57a shows that the field inside the tube (B_i) remains close to zero, which indicates that the externally applied field has not penetrated the tube. This finding is supported by the fact that the induced current I (tube) almost cancels the excitation current NI (shunt). A small field on the outside of the tube ($B_O \cong 10$ gauss) is the leakage field. This leakage field originates from one end of the external coil, circulates through a path outside the coil, and returns to the coil at the other end. Figure 57b shows that the applied field generated by the internal coil has also not penetrated the tube because the field outside the tube (B_O) remains close to zero throughout the test. The field inside the tube is much larger, with a maximum $\cong 400$ gauss. The field inside the tube (B_i) represents the leakage field, which originates from the center of the coil and circulates around the internal coil, through the gap between the superconductor tube and the internal coil. This leakage field is relatively high because all of the fields are concentrated inside the coil, which has a limited volume. This is different from the case with the coil outside the tube, where the leakage field is circulating through an unbounded space.

The current profiles in Fig. 57b are not as symmetric as those in Fig. 57a. Figure 57a shows that the profile of the induced current in the superconductor tube is almost a mirror image of the excitation current, indicating very good shielding and very little leakage field. This current symmetry with respect to the zero current axis is somewhat distorted in Fig. 57b. For example, the peak excitation current is $\approx 13,000$ A, whereas the peak current in the superconductor tube is only $\approx 9,000$ A. This difference in current is needed to support the relatively large leakage field, which is due to the 1-mm gap between the superconductor tube and the internal coil. Even though the leakage field is relatively large when the coil is inside, it is still capable of shielding the space outside the tube from the internally generated magnetic field at relatively low excitation current.

Figures 58a and 58b show the measured current and field at some intermediate excitation current. The magnetic field inside the tube (B_i) (Fig. 58a) shows that 2 ms into the test, when the excitation current reached 32,000 A, the tube is just penetrated by the externally applied magnetic field. The behavior we find interesting is that when the excitation current NI begins to decrease, the magnetic field inside the tube continues to increase. This

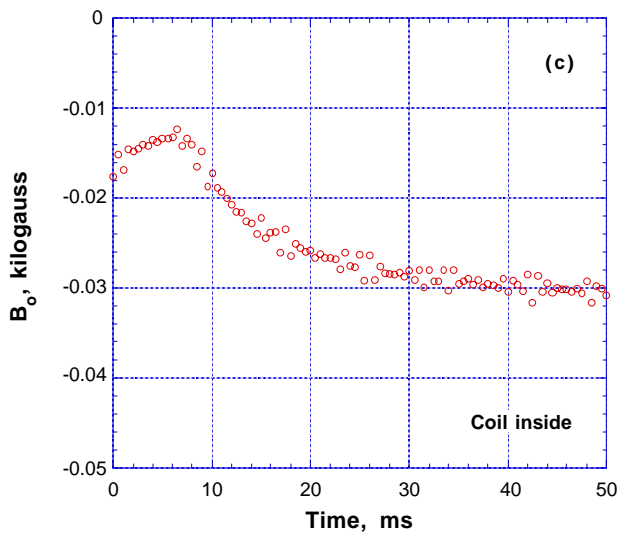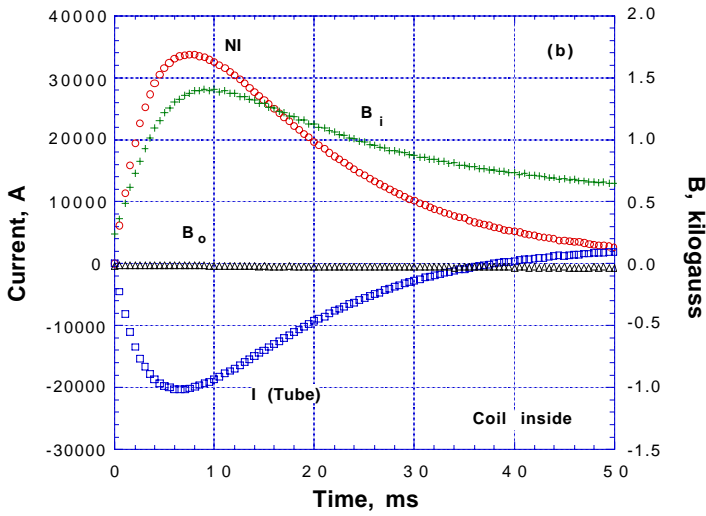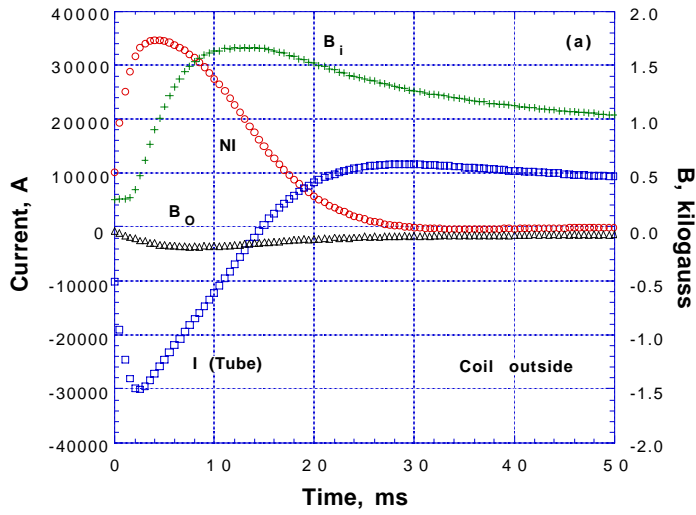*Fig. 58.*
Measured current and field at intermediate excitation current for (a) coil outside superconductor tube, (b) coil inside superconductor tube, and (c) coil inside superconductor tube, results plotted on more sensitive scale.

behavior can be explained by the concept of nonlinear magnetic diffusion. The results shown in Fig. 58b do not seem to indicate that the internally generated magnetic field has penetrated the tube because the field outside the tube (B_O) remains close to zero throughout the test. However, when the field outside the superconductor tube is plotted on a more sensitive scale, as shown in Fig. 58c, the data indicate that the internally generated magnetic field has penetrated the tube at t = 8 ms. This finding corresponds to a peak NI of ≈33,000 A, which equals the NI at penetration for the case of the coil outside the tube.

Figures 59a and 59b show the measured current and field at a relatively high excitation current. With the coil outside the tube, the data for B_i clearly indicate that the externally applied field penetrated the tube in 1.5 ms, and this occurred at NI $\cong$ 40,000 A. Figure 59a shows that, again, there is a delay between the peak NI and the peak B_i. When the coil is inside the tube, the data for B_O in Fig. 59b indicate that the internally generated magnetic field has penetrated the tube and affected the field outside the tube. The data indicate that field penetration occurred at t = 3.5 ms, which corresponds to NI = 52,000 A.

Several features are common to both test configurations. First, both tests show that there is a delay between the peak NI and peak penetration field (peak B_i for the coil outside and peak B_o for the coil inside). This delay decreases with increasing peak NI. For example, the delay between peak NI and peak B_i is 8 ms for peak NI = 34,000 A (Fig. 58a). This delay decreased to 3 ms when peak NI = 65,000 A (Fig. 59a). Similar behaviors were observed for the case with the coil inside the superconductor tube. Second, both test configurations show that the value of NI and I (tube) at field penetration depends on the ramp rate of the excitation current (dI/dt). Third, both test configurations show that the time at field penetration determined by the Hall probe coincides approximately with the time when the induced current I (tube) reaches its maximum value. Finally, all of the tests show that the induced current was initially negative and in the direction opposite of the excitation current, but eventually the induced current crossed over the horizontal axis and became positive, to support the trapped field inside the superconductor tube.

High-T_c superconductors usually follow the so-called power law in the flux creep regime, and the resistivity is a function of current. It can be shown that the magnetic diffusion equation becomes nonlinear when the resistivity depends on the current. For cylindrical geometry, the one-dimensional, nonlinear magnetic diffusion equation takes the form
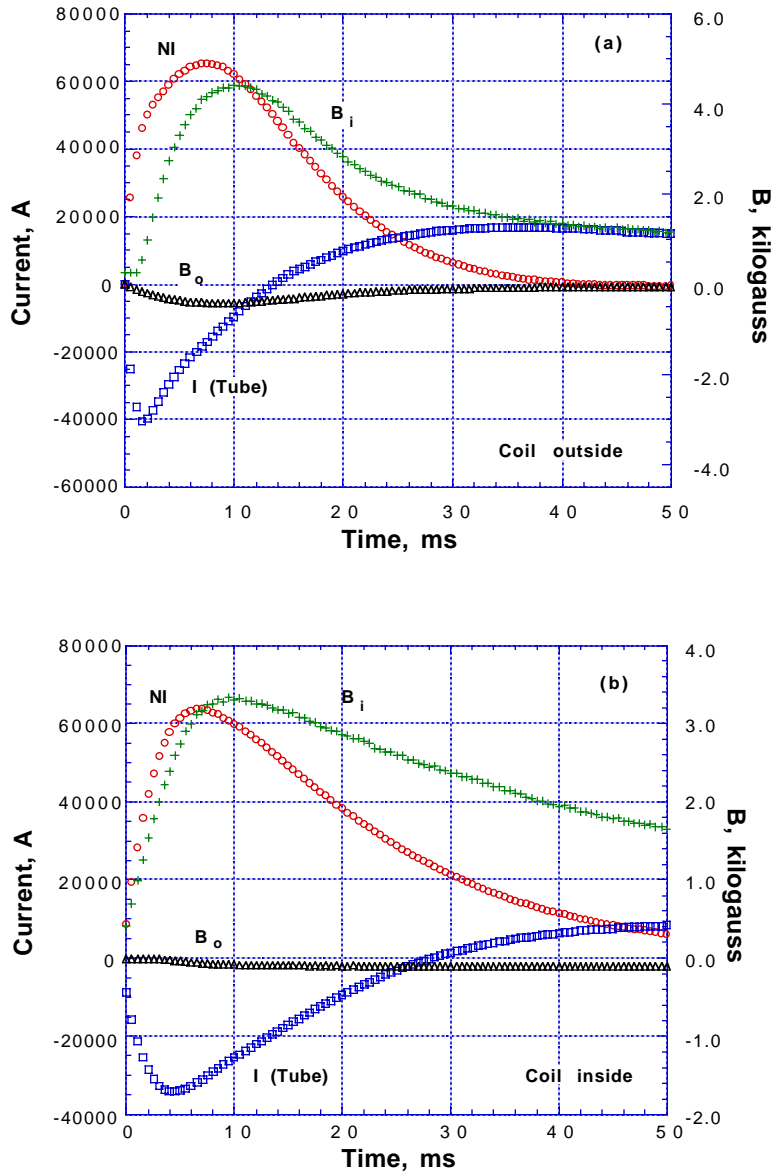
Fig. 59. *Measured current and field at relatively high excitation current for (a) coil outside superconductor tube, and (b) coil inside superconductor tube.*

$$[\partial(D_m r \partial B_Z/\partial r)/\partial r]/r = \partial B_Z/\partial t \,, \qquad\qquad (2)$$

where B_Z is the magnetic flux density in the axial direction, r is the radial coordinate, t is time, and the magnetic diffusion coefficient D_m is given by

$$D_m = \rho(J) / \mu_O \,, \qquad\qquad (3)$$

with the current-dependent resistivity $\rho(J)$ given by the power law. For melt-cast-processed Bi-2212 with a wall thickness of several millimeters, the characteristic diffusion time at 77 K and an electric field strength of 1 μV/cm is several hundred milliseconds. This is much larger than the rise time (several milliseconds) of the pulsed current in the present experiment. Therefore, magnetic diffusion is important and cannot be neglected. However, a characteristic diffusion time of several hundred milliseconds is too long for the Bi-2212 tube to be penetrated in the present experiment, which shows that penetration occurred in a few milliseconds.

Two factors increased the rate of magnetic diffusion and facilitated the field penetration of the tube. First, the speed of magnetic flux propagation (diffusion) strongly depends on the local resistivity ρ in the superconductor. During a transient, the local gradient of magnetic flux density can be greater than that of Bean's model, and the local current density can be greater than the critical current density at a field strength of 1 μV/cm. Local resistivity increases with current density, which speeds up the magnetic diffusion process because the magnetic diffusion coefficient D_m is linearly proportional to ρ. Second, when local ρ increases, so does dissipation (ρJ^2). If heat is not removed quickly enough from the superconductor, the local temperature will rise. When temperature rises, the resistivity increases, further increasing the magnetic diffusion coefficient, and speeding up the magnetic diffusion process. The observation that the penetrated field is still rising while the excitation current (NI) is decreasing is the result of magnetic diffusion. A finite time is necessary for magnetic flux density to diffuse from the interior to the boundary of the tube. When the excitation current begins to decrease, the flux density is greater inside the wall of the tube than outside the wall, magnetic diffusion is still in force and causes the penetrated field to increase. This series of events cannot be explained by Bean's critical-state model, which is applicable to steady-state conditions only.

With regard to applications, such as fault current limiters (FCLs), the present experiments show that the leakage flux is greater when the coil is inside the tube than outside the tube. They also demonstrate that the superconductor tube is equally capable of shielding internally or externally generated magnetic fields. To further support this conclusion, we have measured the inductance ratio of these two configurations. The inductance of the outside coil alone was

0.22 mH; that of the outside coil with the superconductor inside (at 77 K) was 0.049 mH. The reduction in inductance was a factor of 4.48. Inductance of the inside coil alone was 0.096 mH; that of the inside coil with the superconductor outside (at 77 K) was 0.020 mH. Reduction in inductance was a factor of 4.80. Therefore, both configurations will work for an FCL and the reduction in inductance does not differ much. However, under fault conditions, an FCL with a coil inside will have an inductance less than that of an FCL with a coil outside because, inherently, the latter has a larger volume than the former. Finally, it should be noted that the present experiments were conducted with an air core only and are different from the superconductor-shielded-core-reactor (SSCR), which usually contains an iron core. A closed iron-core SSCR is mostly a resistive device and is quite different from an air-core SSCR, which behaves more like an inductive device.

2.3.3 Current Sensor Development

In recent years, magneto-optical sensors have exhibited promise for use in high-power electronics applications. These sensors were first developed to examine current paths in HTS conductors. They offer unique advantages over traditional sensors, such as shunt resistors, current transducers, Hall effect sensors, and magneto-resistive devices. These advantages include galvanic isolation, immunity to stray electromagnetic forces, absence of insertion losses, operation at elevated temperatures, and a frequency-independent response from DC to hundreds of MHz. The operating basis of magneto-optical sensors is the Faraday rotation of linearly polarized light occurring in the sensor material due to the magnetic field generated by the current to be measured. By incorporating the sensor material into a polarization-analyzing optical system (Fig. 60), a change in polarization is transformed into a change of the transmitted light intensity, which, in turn, is the measure of the current. Most current designs of optical high-current sensors, however, require that bulk magneto-optical components or long lengths of optical fiber encircle the current-carrying conductor.

We are developing a miniature high-current sensor that incorporates a new, epitaxial, rare-earth-substituted, iron-garnet, thin-film sensor material into a fiber-optical system. This design is made possible by the exceptionally large Faraday rotation and the unique magnetic properties of the sensor material. In typical epitaxial garnet films, magnetic moments are oriented perpendicular to the film plane, an arrangement that leads to the formation of stripe domains. The magneto-optical signal is a measure of the relative size of up- and down-magnetized domains, which change under the
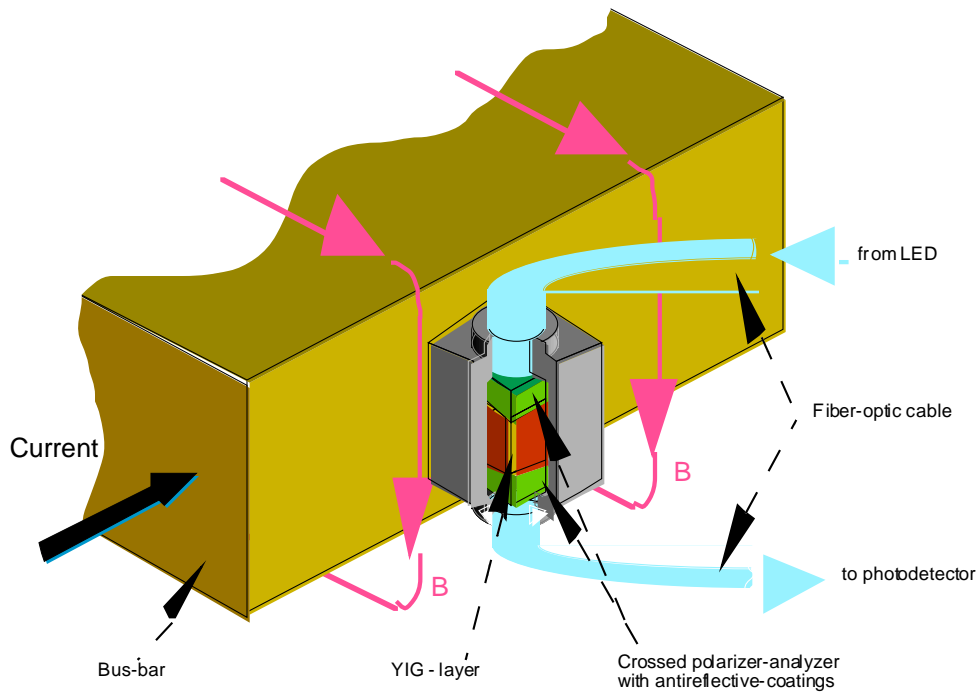
76

Fig. 60. Schematic diagram of current sensor mounted on bus bar. In transmission geometry, separate fibers are used for incoming and detected light.

influence of an external field. In contrast, the new material employed here displays in-plane magnetic anisotropy, and the magneto-optical signal is the result of rotation of the magnetic moments under the influence of the external field. This rotation allows for a linear response over a fairly large range of field and current without the occurrence of hysteresis. In addition, because there is no need to average over a sufficient number of domains, the miniaturization of the sensor to micrometer scale is feasible, offering the possibility of direct integration of the sensor into high-power-electronics chips.

Future work would entail the construction of a prototype fiber-optical current sensor based on a new garnet magneto-optical material with improved characteristics. This work will include design and characterization of the sensor head and its integration into a fiber-optical readout system. We also propose to tailor the specifications of the sensor material (such as sensitivity, field of saturation, spectrum) to the desired application by

changing the doping levels and growth conditions of the garnet films. Two proposals based on this work have been submitted to the U.S. Department of Energy.

Patents: 1999/2000

Method and apparatus for measuring gravitational acceleration utilizing a high temperature superconducting bearing
John R. Hull
U.S. Patent 6,079,267 (June 27, 2000).

Engineered flux pinning centers in BSCCO, TBCCO and YBCO superconductors
Kenneth C. Goretta, Michael T. Lanagan, Jieguang Hu, Dean J. Miller, Suvankar Sengupta, John C. Parker, Uthamalingam Balachandran, Donglu Shi, and Richard W. Siegel
U. S. Patent 5,929,001 (July 27, 1999).

Method and etchant to join Ag-clad BSCCO superconducting tape
Uthamalingam Balachandran, A. N. Iyer, and J. Y. Huang
U.S. Patent 5,882,536 (March 16, 1999).

Elongated Bi-based superconductors made by freeze dried conducting powders
Uthamalingam Balachandran, Milan Lelovic, and Nicholas G. Eror
U.S. Patent 5,874,384 (Feb. 23, 1999).

Thin film seeds for melt processing textured superconductors for practical applications
Boyd W. Veal, Arvydas Paulikas, Uthamalingam Balachandran, and Wei Zhong
U.S. Patent 5,869,431 (Feb. 9, 1999).

Superconductor composite
Stephen E. Dorris, Dominick A. Burlone, and Carol W. Morgan
U.S. Patent 5,866,515 (Feb. 2, 1999).

Surface texturing of superconductors by controlled oxygen pressure
Nan Chen, Kenneth C. Goretta, and Stephen E. Dorris
U.S. Patent 5,856,277 (Jan. 5, 1999).

Publications: FY2000

U. Balachandran, T. R. Askew, Y. S. Cha, S. E. Dorris, J. T. Dusek, J. E. Emerson, B. L. Fisher, K. C. Goretta, K. E. Gray, J. R. Hull, M. T. Lanagan, M. Lelovic, V. A. Maroni, R. L. McDaniel, N. Merchant, D. J. Miller, J.-H. Park, J. J. Picciolo, and J. P. Singh, Practical Superconductor Development for Electrical Power Applications - Annual Report for FY 1999, ANL-99/20 (1999).

Y. S. Cha, Magnetic Diffusion in High-T_c Superconductors, Physica C 330 (2000) 1-8.

B. L. Fisher, K. C. Goretta, N. C. Harris, U. Balachandran; and N. Murayama (Natl. Indus. Res. Inst. of Nagoya), Critical Current Densities in Bi-2223 Sinter Forgings, Advances in Cryogenic Engineering, Vol. 46B, pp. 686-690 (2000), eds. U. Balachandran, D. U. Gubser, K. T. Hartwig, and V. A. Bardos.

K. C. Goretta, Mechanical Properties of Bulk High-Temperature Superconductors, Chapter in "Superconducting Materials: Advances in Technology and Applications," pp. 234-239, eds. A. Tampieri and G. Celotti (World Scientific, Singapore, 2000).

K. C. Goretta and N. Chen, Diffusion and Heat Treatment of High-Temperature Superconductors, Chapter in "Superconducting Materials: Advances in Technology and Applications," pp. 218-228, eds. A. Tampieri and G. Celotti (World Scientific, Singapore, 2000).

J. R. Hull, Superconducting Bearings, Supercond. Sci. Technol. 13 (2000) R1-R15.

J. R. Hull, Effect of Permanent-Magnet Irregularities in Levitation Force Measurements, Supercond. Sci. Technol. 13 (2000), 854-856.

J. Martinez-Fernandez, A. Dominguez-Rodriguez (U. de Sevilla); J. L. Routbort and K. C. Goretta, Creep of Polycrystalline $(Bi,Pb)_2Sr_2Ca_2Cu_3O_x$, Scripta Mater. 42 (2000) 743-747.

J. L. Routbort, K. C. Goretta, R. E. Cook; and J. Wolfenstine (Army Res. Lab., Adelphi, MD), Deformation of Perovskite Electronic Ceramics: A Review, Solid State Ion. 129 (2000) 53-62.

S. Salem-Sugui Jr. (Instituto de Fisica, Rio de Janiero, Brazil) and K. C. Goretta, Study of Flux-Creep in Bulk Melt-Textured $YBa_2Cu_3O_x$ in the Regime of Individual Pinning, J. Supercond. 12, pp. 661–665 (1999).

S. Salem-Sugui Jr. (Instituto de Fisica, Rio de Janiero, Brazil) and K. C. Goretta, Effect of Short-Time Magnetic Relaxation on Hysteresis Curves in Single-Crystal $Bi_2Sr_2CaCu_2O_x$, J. Supercond. 13 (2000) 367-370.

V. Selvamanickam, G. Galinski, G. Carota, J. DeFrank, C. Trautwein, P. Haldar (IGC); U. Balachandran, M. Chudzik; J. Y. Coulter, P. N. Arendt, S. R. Foltyn, B. Newnam, and D. E. Peterson (LANL), High-Current Y-Ba-Cu-O Conductor by Metal Organic Chemical Vapor Deposition on Metal Substrates, Physica C 333 (2000) 155-162 .

B. I. Smirnov, T. S. Orlova (Ioffe Inst., Russia); S. Sengupta (Supercond. Comp., Columbus, OH); and K. C. Goretta, I-V Characteristics and the Electric-Field Effect in Melt-Grown $YBa_2Cu_3O_x/Y_2BaCuO_5$ HTSC Crystals, Phys. Solid State 42 (2000) 1207-1210.

M. Tetenbaum, Thermodynamic and Nonstoichiometric Behavior of Promising High-T_c Cuprate Systems via Electromotive Force Measurements: A Short Review, Metall. Mater. Trans. 30B (2000) 661-666.

B. Venkateshwaran, R. Guo, A. Bhalla (Penn State U.); and U. Balachandran, Quantum Paraelectric-like Behavior of the Paratitanate Family of Materials, Int. J. Inorganic Mater. 1 (1999) 395-402.

B. Venkateshwaran, M. Yao, R. Guo, A. Bhalla (Penn State U.), and
U. Balachandran, Low Temperature Dielectric Properties of Magnetoplumbite Family of Materials, Int. J. Inorganic Mater. 1 (1999) 213-217.